Development of Photocatalytic and Photoelectrochemical Systems using Metal Oxides with Tungsten Bronze Structure and Metal Sulfide for CO_2 Reduction and Water Splitting

（CO_2還元および水分解のためのタングステンブロンズ構造を持つ金属酸化物および金属硫化物を用いた光触媒および光電気化学系の開発）

Tomoaki Takayama
髙山　大鑑

Acknowledgements

The author would like to express his sincere gratitude to his supervisor, Prof. Akihiko Kudo of Faculty of Science, Tokyo University of Science, for Giving very attractive and challenging research of "Development of Photocatalytic and Photoelectrochemical Systems Using Metal Oxides with Tungsten Bronze Structure and Metal Sulfide for CO_2 Reduction and Water Splitting", generous and valuable guidance, fruitful discussion, and kind encouragement throughout this study. The author also would like to express deep gratitude to Dr. Kenji Saito of Nanomaterial Science Laboratory, Niigata University, Graduate School of Science and Technology for many valuable suggestions, helpful discussion, and warm encouragement throughout this study. The author was deeply grateful to Dr. Akihide Iwase for spending a great deal of time with me to discuss and advice. Special thanks are due to all the members of Kudo Laboratory for their much kindness support for the present study. Finally, the author would like to express his heartfelt gratitude to his parents and friends for much kindness, many supports and understanding.

Tomoaki Takayama

Contents

Chapter 1

General introduction

1-1. Background

Energy and chemicals to maintain the modern society depend on fossil fuels. However, the amounts of fossil fuels are limited. Additionally, CO_2 emission in the consuming process brings a green house effect resulting in global warming. The amount of the fossil fuel consumed in the world is steadily increasing. Therefore, development of the next-generation clean energy system and the technology to remove and fix CO_2 has been urged.

"*Hydrogen"* is an ultimate clean energy. Hydrogen changes to not any pollutants but only water (H_2O) by burning. Moreover, the most of chemicals utilized by the modern society has been produced by using *hydrogen* as shown in Figure 1-1. Thus, *hydrogen* is a very important matter for not only pollutant-free society but also chemical industries. However, the main production process of hydrogen is the steam reforming with consuming fossil fuels and emitting a large amount of CO_2 at the present time. In such a background, the solar hydrogen production from water using *photocatalyst* has been paid attention.

Reduction and oxidation proceed using photogenerated electrons and holes in a photocatalyst. For example, water split into H_2 and O_2 on the photocatalyst being similar to electrolysis (Figure 1-2). Because photocatalytic water splitting is the uphill reaction, it can be regarded as the artificial photosynthesis (Figure 1-3). In this reaction, solar energy is converted the storable chemical energy as hydrogen.

The reducing and oxidizing powers of electrons and holes photogenerated in a photocatalyst depend on elements and crystal structure constructing photocatalyst. As the reducing power is large, the electrons in the photocatalyst become to be able to reduce not only water but also other substrates. One of the applications is CO_2 reduction over a photocatalyst using water as an electron donor. The photocatalytic CO_2 reduction is an uphill reaction being similar to photocatalytic water splitting. It is noteworthy in the photocatalytic CO_2 reduction that various reduction products can be obtained by using suitable cocatalysts. Additionally, stored energy is larger than that of water splitting. Therefore, not only water splitting but also CO_2 reduction have extensively been studied in the world.

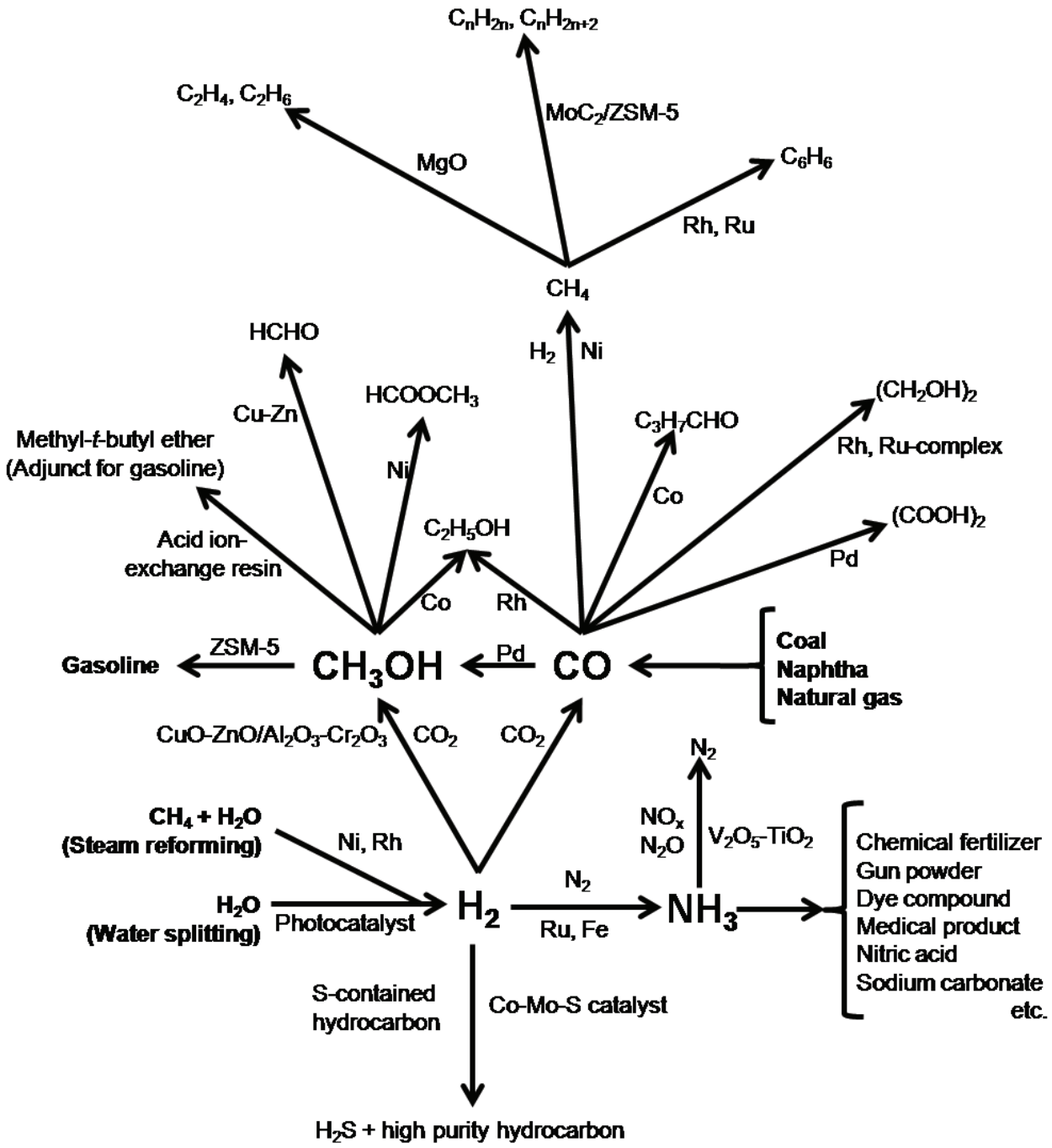

Figure 1-1. The utilization chart of hydrogen in industrial processes.

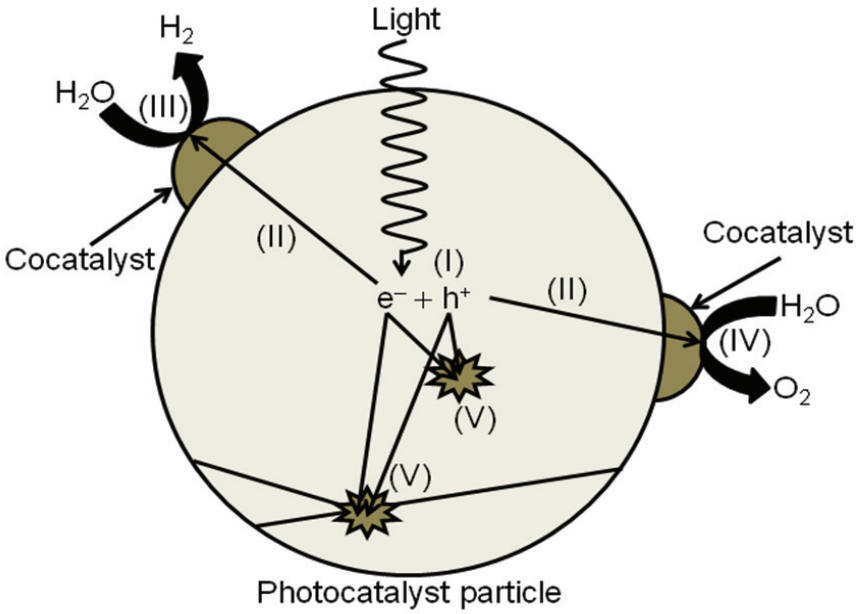

Figure 1-2. Mechanism of water splitting over semiconductor photocatalyst. (I) photon absorption, (II) charge separation and migration of carrier, (III) H_2 evolution, (IV) O_2 evolution, (V) recombination.

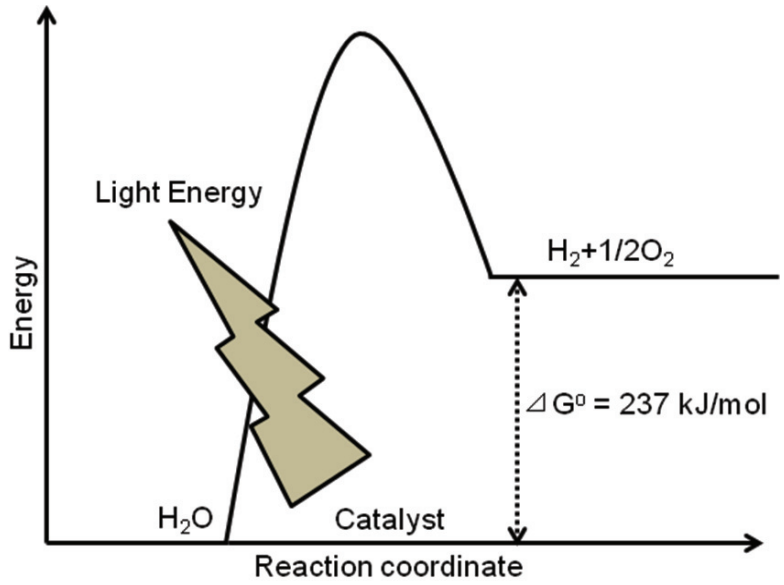

Figure 1-3. The energy diagram of water splitting.

1-2. Photocatalysts

1-2-1. Photocatalytic water splitting

1-2-1-1. Water splitting over metal oxide photocatalysts with wide band gaps

Table 1-1 shows water splitting over metal oxide photocatalysts which have been developed so far. Most of photocatalysts showing activity for water splitting have wide band gaps because large driving forces for reduction and oxidation are necessary to split water. Especially, the photocatalysts containing Ta as a constructing element split water into H_2 and O_2 with high efficiencies. It is due to the conduction band levels formed by Ta5d orbitals. $NaTaO_3$ photocatalyst shows high activity for water splitting by loading NiO-cocatalyst. It split water even without cocatalysts. Moreover, the efficiency for water splitting is drastically enhanced by doping La and alkaline earth metals. The apparent quantum yield for water splitting over La-doped $NaTaO_3$ photocatalyst is about 56% under monochromatic light irradiation at 270 nm. Similarly, ZrO_2 and Ga_2O_3 photocatalysts also split water without cocatalyst. Moreover, the efficiency for water splitting over Ga_2O_3 is dramatically improved by doping Zn and loading $Rh_{2-y}Cr_yO_3$ cocatalyst. Thus, the high efficient water splitting has been achieved by many metal oxide photocatalysts. However, these photocatalysts cannot use for solar hydrogen production because they are wide band gap materials.

1-2-1-2. Development of visible light driven photocatalysts

Development of visible-light-driven photocatalyst is necessary to achieve the solar hydrogen production. Therefore, the band engineering is important to obtain narrow band gap photocatalysts responding to the visible light occupying many parts of a solar spectrum. As the strategy to develop the visible-light-driven photocatalysts, the controlling of a valence band level by substituting metal cations and the forming of an impurity level by doping transition metal cations have been studied.

When Ag^+, Pb^{2+}, Sn^{2+} and Bi^{3+} are doped to wide band gap materials, the band gaps become narrow compared with the original materials. Ag4d, Pb6s, Sn5s and Bi6s orbitals also hybridize

Table 1-1 Water splitting over metal oxide photocatalysts with wide band gap.

Photocatalyst	Activity/μmol h^{-1}		Reaction condition	Ref. No.
	H_2	O_2		
Rh/TiO_2	449	–	Water vapor	1
NiO_x/TiO_2	6	2	3M NaOH aqueous solution	2
Pt/TiO_2	568	287	Na_2CO_3 aqueous solution	3
$NiO_x/SrTiO_3$	24	11	Pure water	4
$NiO_x/K_2La_2Ti_3O_{10}$	444	221	KOH (0.1 M) aqueous solution	5
$NiO_x/La_2Ti_2O_7$:Ba	5000	–	NaOH (24 M) aqueous solution	6
$NiO_x/BaLa_4Ti_4O_{15}$	2300	1154	Pure water	7
$RuO_2/SrLi_2Ti_6O_{14}$	13	7	LiOH (0.01 M) aqueous solution	8
$RuO_2/Na_2Li_2Ti_6O_{14}$	27	14	LiOH (0.01 M) aqueous solution	8
$NiO_x/K_4Nb_6O_{17}$	100	50	Pure water	9
$NiO_x/Sr_2Nb_2O_7$	110	36	Pure water	10
$NiO_x/Ba_5Nb_4O_{15}$	4021	1972	Pure water	7
$RuO_2/NaNbO_3$-nanowire	47	23	Pure water	11
$NiO_x/K_2SmNb_5O_{15}$	64	29	Pure water	12
NiO_x/La_3NbO_7	35	17	Pure water	13
NiO_x/Ta_2O_5	199	90	Pure water	14
NiO_x/La_3TaO_7	164	80	Pure water	13
$NiO/Sr_2Ta_2O_7$	1000	480	Pure water	10
$NiO/NaTaO_3$	2180	1100	Pure water	15
$NiO/NaTaO_3$:La	19800	9660	Pure water	16
$NiO/NaTaO_3$:Sr	9500	4700	Pure water	17
$NiO/K_2PrTa_5O_{15}$	517	238	Pure water	18
$K_3Ta_3B_2O_{12}$	2390	1210	Pure water	19
ZrO_2	72	36	Pure water	14
$Rh_{2-y}Cr_yO_3/Ga_2O_3$	11100	5700	Pure water	20

with O2p orbitals resulting in that the top of new balance band level is more positive than that of only O2p orbitals. Tables 1-2 and 1-3 show the photocatalytic activities for water splitting, hydrogen and oxygen evolution over valence-band-controlled materials. The band gap of $AgTaO_3$ is narrower than that of $NaTaO_3$, even if both crystal structures of the materials are perovskite structure. Because the valence band is formed by the hybrid orbitals consisting of Ag4d and O2p orbitals, $AgTaO_3$ photocatalyst splits water into H_2 and O_2 under UV light irradiation ($\lambda > 300$ nm). Moreover, $AgNbO_3$, $PbTiO_3$ and $BiVO_4$ photocatalysts have narrower band gaps than that of most metal oxide materials such as $NaTaO_3$, $SrTiO_3$ and so, because these photocatalysts have not only new valence band levels formed by hybridizing Ag4d, Pb6s, and Bi6s with O2p orbitals but also more positive levels of conduction bands formed by Nb4d, Ti3d and V3d orbitals than the conduction band levels (Ta5d) of tantalates. These photocatalysts show activities for H_2 and O_2 evolution under visible light irradiation. However, these photocatalysts cannot be used as a single-photocatalyst for water splitting under visible light irradiation.

Metal (oxy)nitrides also show photocatalytic activities for H_2 and O_2 evolution under visible light irradiation because N2p orbitals form the valence band with more negative level than O2p orbitals. Especially, GaN-ZnO solid solution with yellow color can split water into H_2 and O_2 in a stoichiometric amount under visible light irradiation by loading suitable cocatalysts.

To dope transition metal cations into materials with wide band gaps is one of the strategy to develop visible-light-driven photocatalysts. However, although this method gives easily the ability to absorb the visible light to wide band gap photocatalysts, the products don't show photocatalytic activity because the transition metal cations doped in the host materials probably behave as a recombination center to quench photogenerated electrons and holes. Therefore, development of visible-light-driven photocatalysts by doping the transition metal cations has been very difficult. Recently, however, it has been reported that some materials show photocatalytic activity under visible light irradiation by doping the transition metal cations. Among them, Rh-doped $SrTiO_3$, and Cr and Ta-codoped TiO_2 show activities for H_2 and O_2 evolution from an aqueous medium containing the sacrificial reagents under visible light irradiation.

Table 1-2 Valence band-controlled metal oxide and metal (oxy)nitride photocatalysts.

Photocatalysts	Activity / μmol h^{-1}		Reaction conditions	Ref. No.
	H_2	O_2		
$NiO/AgTaO_3$	21	10	Pure water, $\lambda > 300$ nm	21
$AgNbO_3$	–	37	$AgNO_{3\ aq.}$, $\lambda > 420$ nm	21
$PbTiO_3$	–	183	$AgNO_{3\ aq.}$, $\lambda > 420$ nm	22
$RuO_2/PbWO_4$	24	12	Pure water, UV light	23
$RuO_2/Na_4Ta_8P_4O_{32}$	45	22	Pure water, UV light	24
$BiVO_4$	–	31	$AgNO_{3\ aq.}$, $\lambda > 420$ nm	25
$Pt/SnNb_2O_6$	14	–	MeOH aq., $\lambda > 420$ nm	26
$IrO_2/SnNb_2O_6$	–	63	$AgNO_{3\ aq.}$, $\lambda > 420$ nm	26
Pt/TaON	120	–	MeOH aq., $\lambda > 420$ nm	27
Pt/Ta_3N_5	20	–	MeOH aq., $\lambda > 420$ nm	28
RuO_2/ZnO-GaN	60	30	$H_2SO_{4\ aq.}$ (pH = 3), $\lambda > 400$ nm	29

Table 1-3 Transition metal-doped metal oxide photocatalysts.

Photocatalysts	Activity / μmol h^{-1}		Reaction conditions	Ref. No.
	H_2	O_2		
$Pt/SrTiO_3$:Cr,Ta	70	–	MeOH aq., $\lambda > 440$ nm	30
$Pt/SrTiO_3$: Cr,Sb	78	–	MeOH aq., $\lambda > 420$ nm	31
$SrTiO_3$:Rh	90	–	MeOH aq., $\lambda > 440$ nm	32
TiO_2:Cr, Sb	–	32	$AgNO_3$ aq., $\lambda > 420$ nm	31
TiO_2:Rh, Sb	–	17	$AgNO_3$ aq., $\lambda > 440$ nm	33

Table 1-4 Metal sulfide photocatalysts.

Photocatalysts	Rate of H_2 evolution / μmol h^{-1}	Reaction conditions	Ref. No.
$Pt/(AgIn)_{0.22}Zn_{1.56}S_2$	944	$Na_2S + K_2SO_3$ aq., $\lambda > 420$ nm	34
$Ru/CuGa_2In_3S_8$	3200	$Na_2S + K_2SO_3$ aq., $\lambda > 420$ nm	35

Thus, the band engineering of wide band gap photocatalyst is useful to develop new visible-light-driven photocatalyst for H_2 and O_2 evolution and water splitting.

1-2-1-3. Hydrogen evolution over metal sulfide photocatalysts under visible light irradiation

Most of metal sulfide photocatalysts have narrow band gap compared with metal oxide photocatalysts with wide band gap because the position of valence band formed by S3p orbitals is more negative than that of O2p orbitals. Moreover, metal sulfide photocatalyst easily makes the solid solution resulting in the elaborate band engineering by using metal sulfide materials with wide and narrow band gaps. Table 1-4 shows H_2 evolution over metal sulfide photocatalysts from an aqueous medium containing the sacrificial reagents. $(AgIn)_{0.22}Zn_{1.56}S_2$ solid solution (2.33 eV) formed by ZnS (3.55 eV) showing high activity for hydrogen evolution and $AgInS_2$ (1.80 eV) shows activity for highly efficient hydrogen evolution under visible light irradiation. This photocatalyst is active up to 550 nm. Moreover, $CuGa_2In_3S_8$ photocatalyst (1.91 eV) shows activity for hydrogen evolution and responds to 680 nm longer than the absorption edge of the $(AgIn)_{0.22}Zn_{1.56}S_2$ solid solution. Thus, the band gaps of metal sulfide photocatalysts can be controlled relative easily, and the metal sulfide photocatalysts can use visible light occupying many parts of a solar spectrum for H_2 evolution.

1-2-1-4. Water splitting using Z-scheme system under visible light irradiation

In the most of photocatalytic reaction over visible-light driven photocatalysts, the sacrificial reagents are indispensable. In contrast, some visible-light-driven photocatalysts can be used to construct of the Z-scheme type photocatalytic system for water splitting as shown in Figure 1-5. For example, the Z-scheme type system consisting of $Pt/SrTiO_3$:Cr and Pt/WO_3 photocatalysts, and IO_3^-/I^- as a redox mediator shows activity for water splitting under visible light irradiation.[36] Similarly, combined systems with $Pt/SrTiO_3$:Rh photocatalyst for H_2 evolution, and $BiVO_4$,

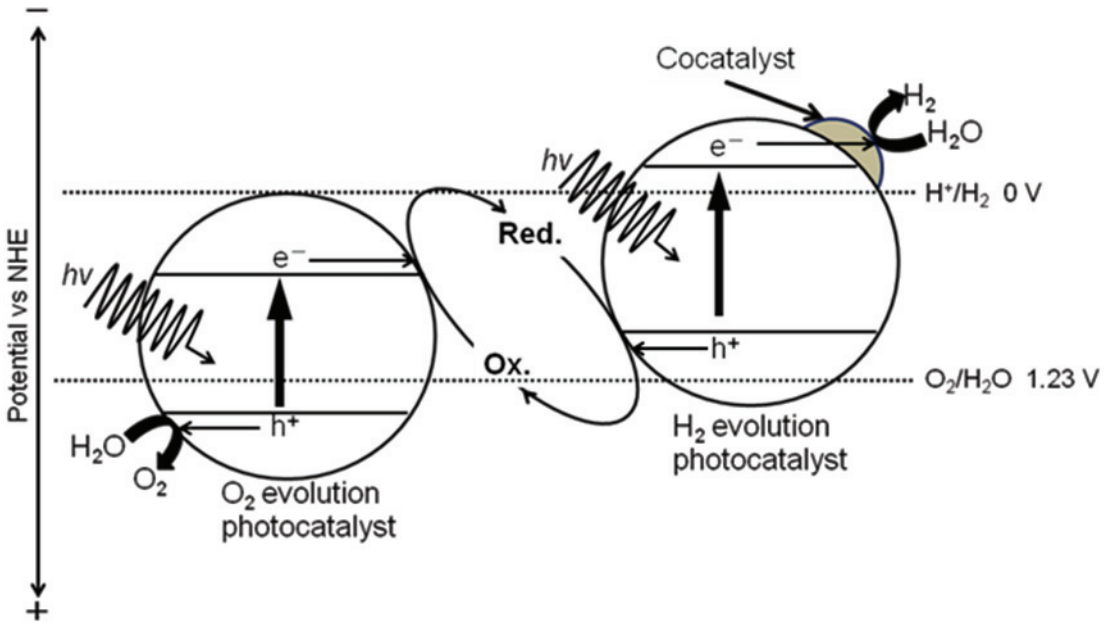

Figure 1-5. The mechanism of water splitting using Z-scheme type photocatalyst system.

Bi_2MoO_6 and WO_3 photocatalysts for O_2 evolution is also active for water splitting in the presence of an $Fe^{3+/2+}$ redox mediator.[37] The Z-scheme type photocatalytic system is important to achieve solar water splitting using various visible-light-driven photocatalysts, while the number of photocatalysts is limited.

1-2-1-5. Water splitting using photoelectrodes

In Honda-Fujishima effect,[38] it had arisen that TiO_2 photoelectrode can split water with external bias smaller than theoretical potential to split water (1.23 V). In other word, the system has achieved to convert light energy to chemical energy by production of the hydrogen from water, while TiO_2 responds not visible light but UV light. Therefore, the water splitting under visible light irradiation is interesting to achieve by using visible-light-driven photocatalyst electrode instead of TiO_2 electrode.

Rh-doped $SrTiO_3$ photoelectrode has arisen as a p-type semiconductor and split water H_2 and O_2 in a stoichiometric amount under visible light irradiation at −0.8 V vs. Pt of a counter electrode as an external bias smaller than 1.23 V.[39]

WO_3 and $BiVO_4$ electrodes with n-type semiconductor character show high activity for photoelectrochemical water splitting under visible light irradiation with suitable external bias and give 75% of the IPCE at 400 nm (1 V vs. RHE, in 1 M $HClO_4$),[40] and 33% at 400 nm (1.3 V vs. Ag/AgCl, in 0.5 M Na_2SO_4),[41] respectively. Moreover, the photoelectrochemical system can use the metal sulfide photocatalyst as a photoelectrode to split water, only if the metal sulfide photocatalyst possesses p-type semiconductor character. For example, Cu_2ZnSnS_4 photoelectrode has p-type semiconductor character and split water under visible light irradiation with an external bias.[42]

1-2-2. Photocatalytic CO_2 reduction

The technology to remove and convert CO_2 has been extensively studied to solve the energy

and environmental issues being similar to the solar hydrogen production using photocatalyst. The photocatalytic CO_2 reduction is one of the strategies. The reaction has been called the artificial photosynthesis mimicking the natural photosynthesis of the green plants because some carbon-containing materials such as CO, HCOOH, HCHO, CH_3OH, CH_4 and so are produced by using water, CO_2 and light energy.

Figure 1-4 shows the redox potential and the stored energy to convert CO_2 to some products by using water as an electron donor. This figure indicates that the CO_2 reduction is an attractive and challenging reaction. This is because the most of reducing potential are more negative level than that of hydrogen production. Moreover, methanol and methane evolutions are multi-electron reaction by consuming 6 and 8-electrons, respectively, even if the reduction potentials are more positive levels than that for hydrogen evolution. Therefore, the stored energy is larger than that of water splitting. Additionally, CO can be used the raw materials to synthesis the gasoline, and CH_3OH and CH_4. They can be direct used as energy source for fuel cells. Therefore, CO_2 reduction is interesting term as not only academic knowledge but also the strategy to convert to storable energy and chemicals.

1-2-2-1. CO_2 reduction using metal complex photocatalysts

The green plant uses the metal complex in the photosynthesis. Therefore, the metal complex photocatalyst to reduce CO_2 using light energy has been synthesized and studied.[52] Among them, the complex photocatalyst consisting of Re as a center metal cation shows activity for CO_2 reduction to form CO using light energy in DMF (N, N-dimethylformamide), while not electrochemical bias but sacrificial reagents are indispensable as shown in Table 1-5. Moreover, Re-Ru super molecule complex with separated absorbing and reacting parts shows high activity for CO_2 reduction with high selectivity for CO evolution. Thus, Re and Ru-metal complexes are the photocatalysts to reduce CO_2 to CO by light energy, while it cannot consumed water as an electron donor.

	(V vs. NHE, pH = 0)	
$CO_2 + 2H^+ + 2e^- \rightarrow HCOOH$	−0.20	(1)
$CO_2 + 2H^+ + 2e^- \rightarrow CO + H_2O$	−0.12	(2)
$CO_2 + 4H^+ + 4e^- \rightarrow HCHO + H_2O$	−0.07	(3)
$2H^+ + 2e^- \rightarrow H_2$	0	(4)
$CO_2 + 6H^+ + 6e^- \rightarrow CH_3OH + H_2O$	+0.03	(5)
$CO_2 + 8H^+ + 8e^- \rightarrow CH_4 + 2H_2O$	+0.17	(6)
$H_2O + 4h^+ \rightarrow 2H^+ + 1/2O_2$	+1.23	(7)
$CO_2 + H_2O \rightarrow HCOOH + 1/2O_2$	$\Delta G^0 = 276$	(8)
$CO_2 + H_2O \rightarrow CO + 1/2O_2 + H_2O$	$\Delta G^0 = 261$	(9)
$CO_2 + H_2O \rightarrow HCHO + O_2$	$\Delta G^0 = 502$	(10)
$CO_2 + 2H_2O \rightarrow CH_3OH + O_2$	$\Delta G^0 = 693$	(11)
$CO_2 + 2H_2O \rightarrow CH_4 + 2O_2$	$\Delta G^0 = 818$	(12)
$H_2O \rightarrow H_2 + 1/2O_2$	$\Delta G^0 = 237$	(13)
	(ΔG^0 / kJ mol^{-1} = $-nFE$)	

Figure 1-4. Chemical equation, redox potential[52] and Gibbs free energy of water splitting and CO_2 reduction.

Table 1-5 CO_2 reduction using metal complex photocatalysts

Photocatalyst	Product	Incident light	Sacrificial reagent	Ref. No.
$[Re(bpy)(CO)_3X]$ (X = Cl, Br and HCOO)	CO	$\lambda > 400$ nm	DMF (Dimethylformamide)	43 44
$[ReBr(CO)_3(bpy)]$	CO	λ =436 nm	TEOA (Triethanolamine)	45 46
[*fac*-$Re(bpy)(CO)_3$-$\{P(Oet)_3\}]^+$	CO	λ = 365 nm	DMF+TEOA	47
$[Ru\text{-}ReP(OEt)_3]^{3+}$	CO	λ =546 nm	DMF+TEOA+BNAH (BNAH: 1-benzyl-1,4-dihydronicotinamide)	48
fac-$[Re(bpy)(CO)_3(NCS)]$ *fac*-$[Re(bpy)(CO)_3(CN)]$	CO	λ = 365 nm	DMF+TEOA	49
$[(dmb)_2Ru(tb\text{-}carbinol)\text{-}(Re(CO)_3Cl_2)(PF_6)_2$ $[(dmb_2Ru)_2(tb\text{-}carbinol)\text{-}Re(CO)_3Cl](PF_6)_4$	CO	$\lambda > 500$ nm	DMF+TEOA+BNAH	50
$[(dmb)_2Ru(bpyC_2bpy)\text{-}Re(CO)_2\{P(p\text{-}FPh)_3\}_2]\text{-}(PF_6)_3$	CO	$\lambda > 500$ nm	DMF+TEOA+BNAH	51

1-2-2-2. CO_2 reduction over semiconductor photocatalysts

Metal oxide photocatalysts showing activity for water splitting can consume water as an electron donor. Therefore, those photocatalysts will be able to be used for the CO_2 reduction using water as an electron donor. Moreover, the selectivity for CO_2 reduction can be controlled by loading suitable cocatalysts. Table 1-6 shows CO_2 reduction over metal oxide photocatalysts loaded with various cocatalysts. Although various reduction products form in the reaction, oxygen evolution in a stoichiometric amount is not observed in many cases. In contrast, ZrO_2 photocatalyst shows activity for CO_2 reduction and produces H_2, CO and O_2 in stoichiometric amounts. Moreover, the selectivity for CO evolution is enhanced by loading Cu cocatalyst. Similarly, $BaLa_4Ti_4O_{15}$ and Zn-doped Ga_2O_3 photocatalysts show high activity for CO_2 reduction with high selectivity for CO evolution, when Ag cocatalyst was loaded. Additionally, O_2 as an oxidizing product of water in a stoichiometric amount is produced in these reaction. However, these wide band gap photocatalysts cannot use CO_2 reduction under the sunlight.

Many metal sulfide photocatalysts are also active for CO_2 reduction as shown in Table 1-7. Although ZnS photocatalyst responds not visible light but UV light, the photocatalysts produce various products by using suitable treatment. In contrast, CdS nanoparticle produces CO by reducing CO_2 under visible light irradiation. In this case, the carbon source of CO is confirmed to be not contamination but CO_2 molecule by an isotope experiment using $^{13}CO_2$.

Thus, metal oxide and metal sulfide photocatalysts can use CO_2 reduction. However, CO_2 reduction over powdered photocatalyst using sunlight and water as an electron donor has not been achieved.

1-2-2-3. CO_2 reduction using photoelectrodes

CO_2 reduction has been studied based on not only photocatalysis but also electrocatalysis. In the results, the properties of the metal electrodes for CO_2 reduction have been clarified as follows.[77-79]

Table 1-6 CO_2 reduction over metal oxide photocatalysts

Photocatalyst	Product	Incident light	Electron source	Ref. No.
TiO_2	CO, CH_4	UV	Water	53
	HCOOH			54
	CH_3OH etc.			55
$BaTiO_3$	HCOOH	UV	Water	56
Zn_2GeO_4	CH_4	UV	Water (Vapor)	57
ZrO_2, Cu/ZrO_2	CO	UV	Water	58
$Ag/BaLa_4Ti_4O_{15}$	CO	UV	Water	59
$Ag/La_2Ti_2O_7$	CO	UV	Water	60
Ag/Ga_2O_3:Zn	CO	UV	Water	61

Table 1-7 CO_2 reduction over metal oxide photocatalysts

Photocatalyst	Product	Incident light	Electron source	Ref. No.
ZnS	HCOOH	$\lambda > 290$ nm	2, 5-dihydrofuran	62
ZnS	HCOOH	$\lambda > 290$ nm	$NaPH_2O_2$, Na_2S	63
ZnS	HCOOH	$\lambda > 320$ nm	Na_2S (+Me_4NCl)	64
CdS	CO	$\lambda > 400$ nm	TEA (+DMF)	65
CdS	HCOOH, CO	$\lambda > 310$ nm	2-propanol	66
CdS	CO, CH_4	UV	Water	67
$Zn_{0.5}Cd_{0.5}S$	CO, HCOOH	$\lambda > 390$ nm	2-propanol	68
$Cu_xAg_yIn_zZn_kS_m$	CH_3OH	$\lambda > 400$ nm	Na_2S	69

Cu: Hydrocarbon

Au, Ag, Zn, Pd, Ga: Carbon monoxide

Pb, Hg, In, Sn, Cd, Tl: Formic acid

Ni, Fe, Pt, Ti: Hydrogen

Table 1-8 shows CO_2 reduction using the electrochemical system. The photoelectrochemical cell consisting of Cu-electrode and GaN-electrode produces CH_4 by using photon energy. Moreover, the electrochemical cell consisting of InP-electrode modified with the polymer of Ru-complex and TiO_2 electrode gives photocurrent and produces HCOOH under pseudo sunlight without any external bias. In this reaction, $H^{13}COOH$, $DCOO^-$ and $^{18}O_2$ are confirmed by suitable isotope experiments indicating that the CO_2 reduction proceeds using water as an electron donor. The hybrid system gives important information to achieve "*CO_2 reduction based on artificial photosynthesis*". Moreover, N-doped Ta_2O_5 photocatalyst modified with Ru-complex shows activity for CO_2 reduction to form HCOOH under visible light irradiation, although a sacrificial reagents is necessary for this system.

Thus, CO_2 reduction has been extensively studied in multi-fields. In the results, the reaction using pseudo sunlight has been achieved. However, the efficiency is not satisfying. Therefore, the continuous and extensive study for CO_2 reduction is necessary to develop the system which convert highly efficient CO_2 to raw materials.

1-3. Objects in this thesis

The problems for CO_2 reduction are listed below.

1) The number of photocatalysts for efficient CO_2 reduction is limited.

2) The mechanism of the reaction on the surface and relationship between the activity and the bulk property is unclearly.

3) The highly efficient photocatalyst for CO_2 reduction under visible light irradiation has not been developed yet.

Table 1-8 CO_2 reduction using semiconductor and metal electrode catalyst

Electrode catalysts		Product	Incident light	Ref.
Anode	Cathode			No.
TiO_2	p-GaP	CH_3OH	UV	70
GaN	Cu	CO, CH_4 HCOOH	UV	71
AlGaN/GaN	Cu	CO, CH_4 HCOOH	UV	72
WO_3	CO	CO, CH_4 HCOOH	$\lambda > 420$ nm	73
Glassy carbon	RCP/p-InP-Zn	HCOOH	$\lambda > 400$ nm	74
Glassy carbon	RCP/Cu_2ZnSnS_4	HCOOH	$\lambda > 400$ nm	75
Pt/TiO_2	RCP/p-InP	HCOOH	Pseudo sunlight	76

RCP: Ru complex polymer

In the present thesis, the author has studied photocatalytic CO_2 reduction over metal oxide photocatalyst with tungsten bronze structure and metal sulfide photoelectrode in order to develop new photocatalyst and photoelectrode and evaluate the reaction mechanism.

In Chapter 2, $KCaSrTa_5O_{15}$ of a new photocatalyst for water splitting and CO_2 reduction was developed. The effects of loading cocatalysts on photocatalytic properties for water splitting and CO_2 reduction were investigated. Moreover, the bulk properties of $KCaSrTa_5O_{15}$ prepared by a solid-state reaction and a polymerized complex method were discussed by using photoluminescence.

In Chapter 3, the photocatalytic activities for water splitting over nanorod-shaped $K_3Ta_3Si_2O_{13}$ and block-shaped $Ba_3Ta_6Si_4O_{26}$ were evaluated. Moreover, the relationship among the distortion of the tungsten bronze-like structure, photocatalytic activity, the crystal growth process and carrier migration was discussed.

In Chapter 4, $Ag/ZnS/Cu_{0.8}Ag_{0.2}GaS_2$ of a new photocathode for CO_2 reduction was developed. The effects of comodification of ZnS and Ag on CO_2 reduction over $Cu_{0.8}Ag_{0.2}GaS_2$ photocathode were evaluated. Moreover, the photoelectrochemical cell using $Ag/ZnS/Cu_{0.8}Ag_{0.2}GaS_2$ as a photocathode and $CoO/BiVO_4$ as a photoanode was constructed to convert CO_2 to CO under pseudo sunlight without any external bias.

In Chapter 5, conclusions in Chapters 2-4 were summarized. Additionally, the vision for the future was discussed.

References

(1) Yamaguti, K.; Sato, S. *J . Chem. Soc., Faraday Trans. 1* **1985**, *81*, 1237.

(2) Kudo, A.; Domen, K.; Maruya, K.; Onishi, T. *Chem. Phys. Lett.* **1987**, *133*, 517.

(3) Sayama, K.; Arakawa, H. *J. Chem. Soc., Faraday Trans.* **1997**, *93*, 1647.

(4) Domen, K.; Kudo, A.; Onishi, T. *J. Catal.* **1986**, *102*, 92.

(5) Takata, T.; Furumi, Y.; Shinohara, K.; Tanaka, A.; Hara, M.; N. Kondo, J.; Domen, K. *Chem. Mater.* **1997**, *9*, 1063.

(6) Kim, J.; W. Hwang, D.; G. Kim, H.; W. Bae, S.; S. Lee, J.; Li, W.; H. Oh, S. *Top. Catal.* **2005**, *35*, 295.

(7) Miseki, Y.; Kato, H.; Kudo, A. *Energy Environ. Sci.* **2009**, *2*, 306.

(8) Iwase, A.; Y. Teoh, W.; Amal, R. *Chem. Lett.* **2011**, *40*, 108.

(9) A) Domen, K.; Kudo, A.; Shinozaki, A.; Tanaka, A.; Maruya, K.; Onishi, T. *J. Chem. Soc.*, *Chem. Commun.* **1986**, 356. B) Kudo, A.; Sayama, K.; Tanaka, A.; Asakura, K.; Domen, K. *J. Catal.* **1989**, *120*, 337. C) Domen, K.; Kudo, A.; Shibata, M.; Tanaka, A.; Maruya, K.; Onishi, T. *J. Chem. Soc.*, *Chem. Commun.* **1986**, 1706.

(10) Kudo, A.; Kato, H.; Nakagawa, S. *J. Phys. Chem. B* **2000**, *104,* 571.

(11) Saito, K.; Koga, K.; Kudo, A. *Dalton Trans.* **2011**, *40*, 3909.

(12) Miseki, Y.; Kudo, A. *ChemSusChem* **2011**, *4*, 245.

(13) Abe, R.; Higashi, M.; Sayama, K.; Abe, Y.; Sugihara, H. *J. Phys. Chem. B* **2006**, *110*, 2219.

(14) Sayama, K.; Arakawa, H. *J. Photochem. Photobiol. A: Chem.* **1994**, *77*, 243.

(15) Kato, H.; Kudo, A. *J. Phys. Chem. B* **2001**, *105*, 4285.

(16) Kato, H.; Asakura, K.; Kudo, A. *J. Am. Chem. Soc.* **2003**, *125*, 3082.

(17) Iwase, A.; Kato, H.; Okutomi, H.; Kudo, A. *Chem. Lett.* **2004**, *33*, 1260.

(18) Kudo, A.; Okutomi, H.; Kato, H. *Chem. Lett.* **2000**, 1212.

(19) Kurihara, T.; Okutomi, H.; Miseki, Y.; Kato, H.; Kudo, A. *Chem. Lett.* **2006**, *35*, 274.

(20) Hisatomi, T.; Miyazaki, K.; Takanabe, K.; Maeda, K.; Kubota, J.; Sakata, Y.; Domen, K. *Chem. Phys. Lett.* **2010**, *486*, 144.

(21) Kato, H.; Kobayashi, H.; Kudo, A. *J. Phys. Chem.* B **2002**, *106*, 12441.

(22) Arney, D.; Watkins, T.; Maggard, A. P. *J. Am. Ceram. Soc.* **2011**, *94*, 1483.

(23) Saito, N.; Hisayoshi, K.; Kobayashi, H.; Ikarashi, K.; Nishiyama, H.; Inoue, Y. *Chem. Lett.* **2004**, *33*, 1452.

(24) Nishiyama, H.; Kobayashi, H.; Inoue, Y. *ChemSusChem* **2011**, *4*, 208.

(25) Kudo, A.; Ueda, Kazuhiro, Kato, H.; Mikami, I. *Catal. Lett.* **1998**, *53*, 229.

(26) Hosogi, Y.; Shimoda, Y.; Kato, H.; Kobayashi, H.; Kudo, A. *Chem. Mater.* **2008**, *20*, 1299.

(27) Hara, M.; Nunoshige, J.; Takata, T.; Kondo, N. J.; Domen, K. *Chem. Comm.* **2003**, 3000.

(28) Lee, Y.; Nukumizu, K.; Watanabe, T.; Takata, T.; Hara, M.; Yoshimura, M.; Domen, K. *Chem. Lett.* **2006**, *35*, 352.

(29) Maeda, K.; Teramura, K.; Takata, T.; Hara, M.; Saito, N.; Toda, K.; Inoue, Y.; Kobayashi, H.; Domen, K. *J. Phys. Chem. B* **2005**, *109*, 20504.

(30) Ishii, T.; Kato, H.; Kudo, A. *J. Photochem. Photobiol. A: Chem.* **2004**, *163*, 181.

(31) Kato, H.; Kudo, A. *J. Phys. Chem. B* **2002**, *106*, 5029.

(32) Konta, R.; Ishii, T.; Kato, H.; Kudo, A. *J. Phys. Chem. B* **2004**, *108*, 8992

(33) Niishiro, R.; Konta, R.; Kato, H.; Chun, W. J.; Asakura, K.; Kudo, A. *J. Phys. Chem. C* **2007**, *111*, 17420.

(34) Tsuji, I.; Kato, H.; Kobayashi, H.; Kudo, A. *J. Am. Chem. Soc.* **2004**, *126*, 13406.

(35) Kaga, H.; Saito, K.; Kudo, A. *Chem. Commun.* **2010**, *46*, 3779.

(36) Sayama, K.; Mukasa, K.; Abe, R.; Abe, Y.; Arakawa, H. *J. Photochem. Photobiol. A: Chem.* **2002**, *148*, 71.

(37) Kato, H.; Hori, M.; Konta, R.; Shimodaira, Y.; Kudo, A. *Chem. Lett.* **2004**, *33*, 1348.

(38) Fujishima, A.; Honda, K. *Nature* **1972**, *238*, 37.

(39) Iwashina, K.; Kudo, A. *J. Am. Chem. Soc.* **2011**, *133*, 132772.

(40) Santato, C.; Ulmann, M.; Augustynski, J. *J. Phys. Chem. B* **2001**, *105*, 936.

(41) Sayama, K.; Nomura, A.; Zou, Z.; Abe, R.; Abe, Y.; Arakawa, H. *Chem. Comm.* **2003**, 2908.

(42) Ma, G.; Minegishi, T.; Yokoyama, D.; Kubota, J.; Domen, K. *Chem. Phys. Lett.* **2011**,

501,619.

(43) Hawecker, J.; Lehn, J. M.; Ziessel, R. *J. Chem. Soc., Chem. Commun.* **1983**, 536.

(44) Hawecker, J.; Lehn, J. M.; Ziessel, R. *Helv. Chim. Acta* **1986**, *69*, 1990.

(45) Kutal, C.; Weber, A. M.; Ferraudi, G.; Geiger, D. *Organometallics* **1985**, *4*, 2161.

(46) Kutal, C.; Corbin, J. A.; Ferraudi, G. *Organometallics* **1987**, *6*, 553.

(47) Hori, H.; Johnson, A. P. F.; Koike, K.; Ishitani, O.; Ibusuki, T. *J. Photochem. Pahotobiol. A:Chem.* **1996**, *96*, 171.

(48) Sato, S.; Koike, K.; Inoue, H.; Ishitani, O. *Photochem. Photobiol. Sci.* **2007**, *6*, 454.

(49) Takeda, H.; Koike, K.; Inoue, H.; Ishitani, O. *J. Am. Chem. Soc.* **2008**, *130*. 2023.

(50) Bian, Y. Z.; Sumi, K.; Furue, M.; Sato, S.; Koike, K.; Ishitani, O. *Dalton Trance.* **2009**, 983.

(51)Tamaki, Y.; Watanabe, K.; Koike, K.; Inoue, H.; Morimoto, T.; Ishitani, O. *Faraday Discuss.* **2012**, *155*, 115.

(52) Takeda, H.; Ishitani, O. *Coordination Chemistry Reviews* **2010**, *254*, 346.

(53) Inoue, T.; Fujishima, A.; Konishi, S.; Honda, K. *Nature* **1979**, *277*, 637.

(54) Halmann, M.; Katzir, V. *Solar Energy Materials* **1984**, *10*, 85.

(55) Mao, J.; Li, K.; Peng, T. *Catal. Sci. Technol.* **2013**, *3*, 2481.

(56) Ulman, M.; Blajrni, B. A.; Halmann, M. *Israel J. Chem.* **1982**, *22*, 177.

(57) Liu, Q.; Zhou, Y.; Kou, J.; Chen, X.; Tian, Z.; Gao, J.; Yan, S.; Zou, Z. *J. Am. Chem. Soc.* 2**010**, *132*, 14385.

(58) Sayama, K.; Arakawa, H. *J. Phys. Chem. Lett.* **1993**, *97*, 531.

(59) Iizuka, K.; Wato, T.; Miseki, Y.; Saito, K.; Kudo, A. *J. Am. Chem. Soc.* **2011**, *133*, 20863.

(60) Wang, Z.; Teramura, K.; Hosokawa, S.; Tanaka, T. *Appl. Catal. B: Emviron.* **2015**, *163*, 241.

(61) K. Teramura, Z. Wang, S. Hosokawa, Y. Sakata, T. Tanaka, *Chem. Eur. J.* **2014**, 20, 9906.

(62) Kisch, H.; Twardzik, G. *Chem. Ber.* **1991**, *124*, 1161.

(63) Kanemoto, M; Shiragami, T.; Pac, C.; Yanagida, S. *Chem. Lett.* **1990**, 931.

(64) Eggins, R. B.; Robertson, J. K. P.; Stewart, H. J.; Woods, E. *J. Chem. Soc., Chem. Commun.* **1993**, 349.

(65) Kanemoto, M.; Ishihara, K.; Wada, Y.; Sakata, T.; Mori, H.; Yanagida, S. *Chem. Lett.* **1992**, 835.

(66) Inoue, H.; Nakamura, R.; Yoneyama, H. *Chem. Lett.* **1994**, 1227.

(67) Praus, P.; Kozak, O.; Koci, K.; Panacek, A.; Dvorsky, R. *J. Colloid Interf. Sci.* **2011**, *360*, 574.

(68) Inoue, H.; Moriwaki, H.; Maeda, K.; Yoneyama, H. *J. Photochem. Photobiol. A: Chem.* **1995**, *86*, 191.

(69) Liu, Y. J.; Garg, B.; Ling, C. Y. *Green Chem.* **2011**, *13*, 2029.

(70) Halmann, M. *Nature* **1978**, *275*, 115.

(71) Yotsuhashi, S.; Deguchi, M.; Zenitani, Y.; Hinogami, R. Hashiba, H.; Yamada, Y.; Ohkawa, K. *Appl. Phys. Express* **2011**, *4*, 117101.

(72) Yotsuhashi, S.; Deguchi, M.; Hashiba, H.; Zenitani,Y.; Hinogami, R.; Yamada, Y.; Ohkawa, K. *Appl. Phys. Lett.* **2012**, *100*, 243904.

(73) Magesh, G.; Kim, E. S.; Kang, H. J.; Banu, M.; Kim, J. Y.; Kim, J. H.; Lee, J. S. *J. Mater. Chem. A,* **2014**, *2*, 2044.

(74) Arai, T.; Sato, S.; Uemura, K.; Morikawa, T.; Kajino, T.; Motohiro, T. *Chem. Commun.* **2010**, *46*, 6944.

(75) Arai, T.; Tajima, S.; Sato, S.; Uemura, K.; Morikawa, T.; Kajino, T. *Chem. Commun.* **2011**, *47*, 12664.

(76) Sato, S.; Arai, T.; Morikawa, T.; Uemura, K.; Szuki, M. T.; Tanaka, H.; Kajino, T. *J. Am. Chem. Soc.* **2011**, *133, 15240.*

(77) Hori, Y.; Kikuchi, K.; Suzuki, S. *Chem. Lett.* **1985**, 1695.

(78) Hori, Y.; Wakebe, H.; Tsukamoto, T.; Koga, O. *Electrochim. Acta* **1994**, *39*, 1833.

(79) Hatsukade, T.; P. Kuhl, K.; R. Cave, E.; N Abram, D.; F. Jaramillo, T. *Phys. Chem. Chem. Phys.* **2014**, *16*, 13814.

Chapter 2

Development of $KCaSrTa_5O_{15}$ of a new photocatalyst with tungsten bronze structure prepared by a solid-state reaction and a polymerized complex method for water splitting and CO_2 reduction

2-1. Introduction

An artificial photosynthesis system has been extensively studied to develop systems for CO_2 conversion to fuels and chemicals. Photocatalytic CO_2 reduction is one of the potential candidates for the artificial photosynthesis. Homogeneous and heterogeneous photocatalyst systems for CO_2 reduction have been studied. The homogeneous photocatalysts including Re-complex and Re-Ru-complex require sacrificial reducing reagents such as TEOA (Triethanolamine) to reduce CO_2 to CO and HCOOH.[1-6] Although a heterogeneous CdS photocatalyst shows activity for CO_2 reduction to form CO under visible light irradiation, sacrificial reagents are also indispensable.[7-8] Heterogeneous metal oxide photocatalysts which possess the ability for O_2 evolution by oxidation of water have been reported for the CO_2 reduction to form HCOOH, CO, CH_3OH and CH_4 in aqueous media without sacrificial reagents.[9-16] However, oxygen evolution in a stoichiometric amount is not observed in many cases. Among them, a ZrO_2 photocatalyst produces CO and H_2 as reduction products and O_2 as an oxidation product in a stoichiometric amount under UV irradiation.[14] Moreover, the activity and selectivity for CO_2 reduction to form CO are enhanced by loading a Cu cocatalyst on the ZrO_2 photocatalyst. $BaLa_4Ti_4O_{15}$[15] and Zn-doped Ga_2O_3[16] are highly active for CO_2 reduction using water as an electron donor when Ag cocatalyst is employed. Thus, metal oxide photocatalysts for water splitting can be applied to CO_2 reduction using water as an electron donor if suitable cocatalysts are chosen.

We have developed tantalum-based photocatalysts, such as $NaTaO_3$ and $NaTaO_3$:A (A = La and Sr) with perovskite structure, and $K_2LnTa_5O_{15}$ (Ln = La, Pr, Nd, Sm, Gd, Tb, Dy and Tm) with tungsten bronze structure, for highly efficient water splitting under UV irradiation.[17-19] The high activities for the tantalum-based photocatalysts are mainly due to their high conduction bands formed by Ta5d orbitals. We have also reported that a $BaLa_4Ti_4O_{15}$ photocatalyst[20] with two dimensional anisotropy of crystal structure for water splitting also shows activity for CO_2 reduction using water as an electron donor by loading highly dispersed Ag cocatalyst.[15] The selectivity for the CO_2 reduction is superior to that for water reduction to form H_2 even in an aqueous medium. On the other hand, there is a tantalate group that possesses tungsten bronze structure with anisotropy to a

c-axis of the crystal structure and the framework consisting of TaO_6 octahedra with corner sharing being similar to the perovskite structure as seen in $NaTaO_3$ of a highly efficient photocatalyst for water splitting. Therefore, the tantalates with tungsten bronze structure are expected to be active for water splitting and CO_2 reduction.

The preparation method of the photocatalysts affects the photocatalytic properties. A polymerized complex method provides highly crystalline particles due to well-mixed metal cations at the atomic level during the synthetic process.[34] For example, a single phase of $BaLa_4Ti_4O_{15}$ photocatalyst can be obtained at lower temperature by a polymerized complex method than a solid-state reaction. The particles prepared by a polymerized complex method possess a plate shape with reduction sites separated from oxidation sites.[20] Well-crystallized particles of $K_2LaNb_5O_{15}$ with tungsten bronze structure can also be obtained by a polymerized complex method, resulting in higher photocatalytic activity for water splitting than that prepared by a solid-state reaction.[35] Thus, the polymerized complex method is a useful for the synthesis of highly active photocatalyst particles with high crystallinity and a characteristic shape.

In the present study, $KCaSrTa_5O_{15}$ with tungsten bronze structure[21] was prepared by a solid-state reaction, and their photocatalytic activities for water splitting and CO_2 reduction were investigated. The photocatalyst particles and cocatalysts were characterized using SEM, XPS and DRS. Moreover, well-crystalline $KCaSrTa_5O_{15}$ was prepared by a polymerized complex method and its photocatalytic activity for water splitting and CO_2 reduction were evaluated. The relationship between photocatalytic activity and migration of photogenerated electrons and holes was also discussed by monitoring the emission of Tb^{3+} doped in the well-crystalline $KCaSrTa_5O_{15}$ host as a guest.

2-2. Experimental

Preparation of $KCaSrTa_5O_{15}$

$KCaSrTa_5O_{15}$ powder was prepared by a solid-state reaction and a polymerized complex method (denoted as SSR-$KCaSrTa_5O_{15}$ and PC-$KCaSrTa_5O_{15}$, respectively). Starting materials of

K_2CO_3 (Kanto Chemical; 99.0%), $CaCO_3$ (Kanto Chemical; 99.5%), $SrCO_3$ (Kanto Chemical; 99.9%), and Ta_2O_5 (Rare Metallic; 99.99%) for SSR-$KCaSrTa_5O_{15}$ were mixed in an atomic ratio of K:Ca:Sr:Ta=1.05:1:1:5. The excess amount of potassium (5 mol%) was to compensate the volatilization.[22] The mixed powder was calcined in air at 1173 K for 1 h and subsequent 1423 K for 10 h in a platinum crucible. The excess potassium was washed out with water from the obtained powder. For the synthesis of PC-$KCaSrTa_5O_{15}$, $TaCl_5$ (Aldrich Japan; 99.99%), K_2CO_3 (Kanto Chemical; 99.0%), $CaCO_3$ (Kanto Chemical; 99.5%), and $SrCO_3$ (Kanto Chemical; 99.9%) were used as starting materials. Those metal compounds and a citric acid were dissolved in a mixed solvent of ethanol and ethylene glycol.[35, 36] The mixture was heating at 393 K in air to obtain a precursor. The precursor was calcined at 1173 K for 10 h in air to obtain PC-$KCaSrTa_5O_{15}$. Tb^{3+} was doped into the SSR-$KCaSrTa_5O_{15}$ and PC-$KCaSrTa_5O_{15}$ for a photoluminescence measurement using Tb_4O_7 (Soekawa Chemical; 99.9%) and $Tb(CH_3COO)_3 \bullet 4H_2O$ (Wako Pure Chemical; 99.9%) as starting materials, respectively. Various cocatalysts were loaded by impregnation and photodeposition methods on the surface of $KCaSrTa_5O_{15}$ photocatalyst. NiO and Ag cocatalysts were loaded by an impregnation method. Photocatalyst powder was dispersed in aqueous solutions dissolving $Ni(NO_3)_2$ (Wako Pure Chemical: 98.5%) and $AgNO_3$ (Tanaka Rare Metal) in a porcelain crucible. The slurry solution was stirred with a glass rod during evaporation using a hot plate. Obtained powder was calcined in air at 575 K and 723 K for 1 h for loading the NiO and Ag cocatalysts, respectively. The NiO and Ag cocatalysts were reduced with H_2 at 773 K, if necessary. Ag, Ni, Ru, Rh, Pt, Cu and Au cocatalysts were photodeposited from aqueous solutions dissolving suitable amounts of $AgNO_3$, $Ni(NO_3)_2$, $RuCl_3$, $RhCl_3$, H_2PtCl_6, $Cu(NO_3)_2$ and $HAuCl_4$ *in situ*.

Characterization of $KCaSrTa_5O_{15}$

$KCaSrTa_5O_{15}$ powders prepared by a solid-state reaction at several temperatures were examined by X-ray diffraction using Cu Kα radiation (Rigaku: Miniflex). Diffuse reflectance spectra of these powders were obtained using a UV-vis-NIR spectrometer (Jasco: UbestV-570) and were converted from reflection to absorption by the Kubelka-Munk method. Photocatalyst powders

were observed by a scanning electron microscope (JEOL: JSM-6700F). Surface species of cocatalysts on photocatalysts were analyzed by X-ray photoelectron spectroscopy (Shimazdu: ESCA-3400; Mg anode). Metallic Ni (Nilaco: 99+%), NiO (Soekawa Chemical: 99.9%) and $Ni(OH)_2$ (Wako Pure Chemical: 95.0%) were employed as references for the XPS measurements. Binding energies were corrected using C 1s (285.0 eV) on a metallic Au foil (84.0 eV).[23] The surface area was examined by BET measurement (BECKMAN COULTER: SA3100). The emission spectrum of the obtained powder was monitored using a spectrofluorometer (HORIBA JOBIN YVON; SPEX Fluorolog-3).

Photocatalytic water splitting and CO_2 reduction

0.5 g of photocatalyst powder was dispersed in 350 mL of water in an inner irradiation cell made of quartz with a 400 W high-pressure mercury lamp. $NaHCO_3$ was added into the water for CO_2 reduction, if necessary. Ar or CO_2 gas was continually bubbled into the suspension at 30 mL min^{-1} of a flow rate during the photocatalytic reactions. The gaseous products of H_2, O_2, and CO were determined using a gas chromatograph (Shimadzu; GC-8A, MS-5A, TCD, Ar carrier for H_2 an O_2; GC-8A, SHINCARBON ST, TCD, He carrier for CO). The isotope measurement was conducted using a $^{13}CO_2$ (99.5 atom%) gas. The product of ^{13}CO was analyzed using a GC-MS (Shimadzu; GC-MS Plus 2010, RESTEK; RT-Msieve 5A). The apparent quantum yield for water splitting was examined using a gas-closed circulation system equipped with a top-irradiation cell made of quartz. 0.5 g of photocatalyst powder was dispersed into 350 mL of water. A 300 W Xe-arc lamp equipped with a band-pass filter was employed as the monochromatic light source at 254 nm.

2-3. Results and discussion

2-3-1. Development of $KCaSrTa_5O_{15}$ of a new photocatalyst prepared by a solid-state reaction

2-3-1-1. Characterization of $KCaSrTa_5O_{15}$ prepared by a solid-state reaction

The X-ray diffraction patterns of the materials prepared at different calcination temperatures were assigned to $KCaSrTa_5O_{15}$ (PDF: 40-351) as shown in Figure 2-1. Calcination below 1573 K

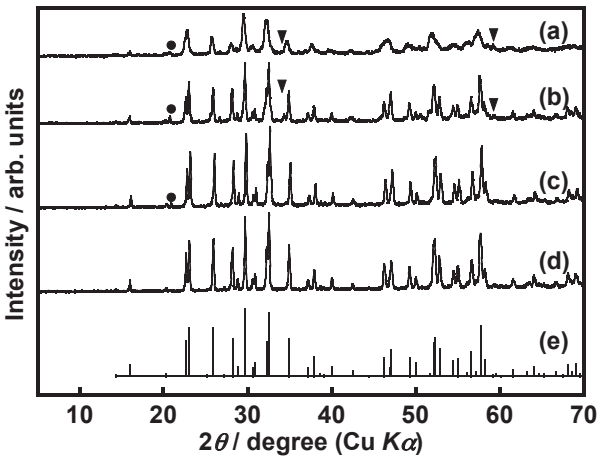

Figure 2-1 X-ray diffraction patterns of $KCaSrTa_5O_{15}$ prepared at (a) 1173 K, (b) 1423 K, (c) 1573 K and (d)1773 K for 10 h. (e) $KCaSrTa_5O_{15}$ (PDF:40-351). Closed triangle and closed circle represent $Ca_2Ta_2O_7$ (PDF: 53-743) and an unknown compound, respectively.

gave small amounts of $Ca_2Ta_2O_7$ (PDF: 53-743) and an unknown compound as impurities (Figure 2-1 (a), (b) and (c)), while the single phase of highly crystalline $KCaSrTa_5O_{15}$ was obtained by calcining at 1773 K for 10 h (Figure 2-1 (d)). The band gap of $KCaSrTa_5O_{15}$ was estimated to be 4.1 eV from the absorption edges except for the material prepared at 1173 K as shown in Figure 2-2. Primary particles of $KCaSrTa_5O_{15}$ with 200-300 nm of an average diameter aggregated, when they were prepared below 1573 K as shown in Figure 2-3 (a), (b) and (c). In contrast, the morphology of $KCaSrTa_5O_{15}$ prepared at 1773 K was rod as shown in Figure 2-3 (d), reflecting tungsten bronze structure in which TaO_6 octahedral units were connected with each other along the c-axis.

2-3-1-2. Photocatalytic water splitting and CO_2 reduction over $KCaSrTa_5O_{15}$ prepared by a solid-state reaction

Table 2-1 shows activity for water splitting over $KCaSrTa_5O_{15}$ under Ar gas flow. All samples prepared at different temperatures showed the activity for water splitting without cocatalyst. Moreover, the activities were drastically enhanced when NiO cocatalyst was loaded on $KCaSrTa_5O_{15}$. In contrast, the activities of $KCaSrTa_5O_{15}$ were not enhanced when Ni cocatalysts were loaded by a photodeposition, and an impregnation and H_2 reduction. NiO-loaded $KCaSrTa_5O_{15}$ prepared at 1423 K showed the highest activity. Although the initial activity of this photocatalyst was high, the rates of H_2 and O_2 evolution decreased at the initial stage as shown in Figure 2-4. H_2 and O_2 steadily evolved in a stoichiometric amount after the deactivation. The apparent quantum yield was 2.3% at 254 nm for water splitting. Thus, $KCaSrTa_5O_{15}$ with tungsten bronze structure has arisen as a new photocatalyst for water splitting.

The $KCaSrTa_5O_{15}$ photocatalyst was applied to CO_2 reduction as shown in Table 2-2. The pristine $KCaSrTa_5O_{15}$ produced only H_2 and O_2 without any reduction products of CO_2. This indicates that there were no active sites for CO_2 reduction on the surface of the $KCaSrTa_5O_{15}$ photocatalyst. Therefore, various cocatalysts were loaded to introduce active sites. Water splitting activity of $KCaSrTa_5O_{15}$ was enhanced when NiO and Au of effective cocatalysts[17, 24-25] for water

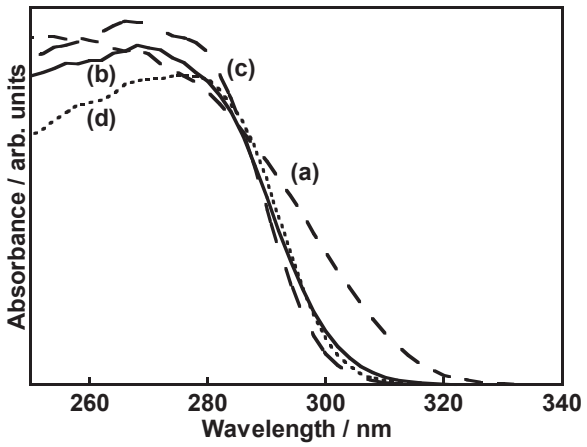

Figure 2-2 Diffuse reflectance spectra of $KCaSrTa_5O_{15}$ prepared at (a) 1173 K, (b) 1423 K, (c) 1573 K and (d) 1773 K for 10 h.

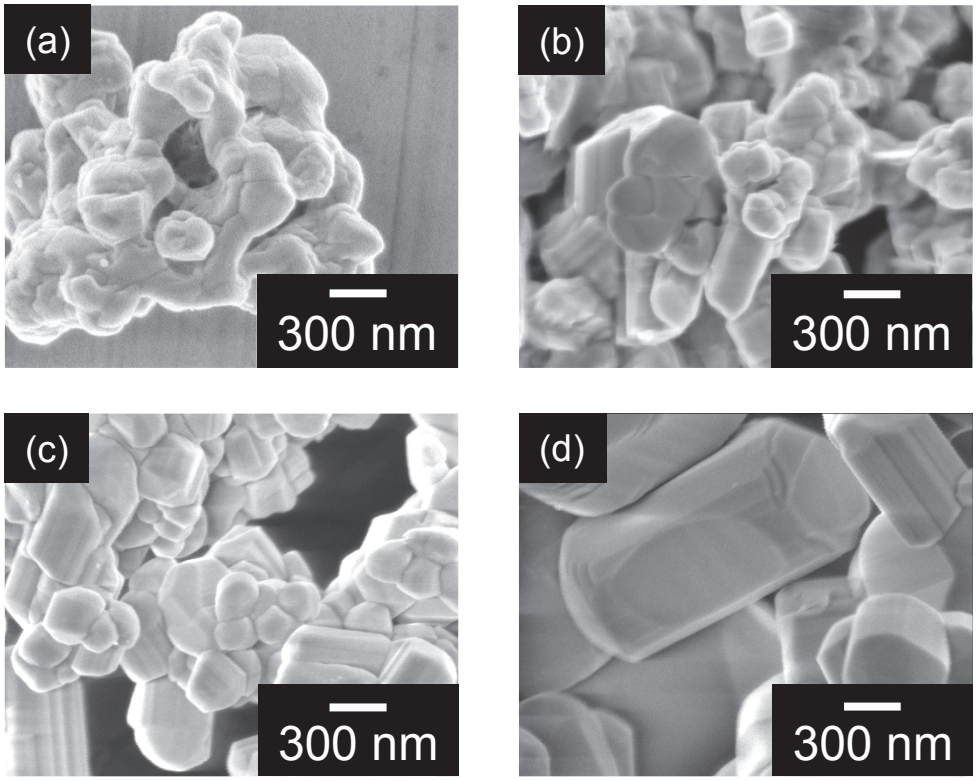

Figure 2-3 SEM images of $KCaSrTa_5O_{15}$ prepared at (a) 1173 K, (b) 1423 K, (c) 1573 K and (d) 1773 K for 10 h.

Table 2-1 Photocatalytic water splitting over $KCaSrTa_5O_{15}$ prepared at different temperatures.

Preparation Temperature / K	Cocatalyst	Loading method	Activity / μmol h^{-1}	
			H_2	O_2
1173	None	-	271	180
1173	NiO	Impregnation	639	263
1423	None	-	102	42
1423	NiO	Impregnation	1339	700
1423	Ni	Photodeposition	25	12
1423	Ni	Impregnation + H_2 red.	115	62
1573	None	-	106	47
1573	NiO	Impregnation	1270	644
1773	None	-	66	31
1773	NiO	Impregnation	212	95

Photocatalyst: 0.5 g, cocatalyst: 0.5 wt%, loading conditions: impregnation (573 K for 1 h in air), impregnation and subsequent H_2 reduction (773 K for 2 h in H_2 flow), photodeposition (*in situ*), reactant solution: water (350 mL), light source: a 400 W high-pressure mercury lamp, reactor: an inner irradiation cell made of quartz. $KCaSrTa_5O_{15}$ was prepared by a solid-state reaction at 1423 K for 10 h.

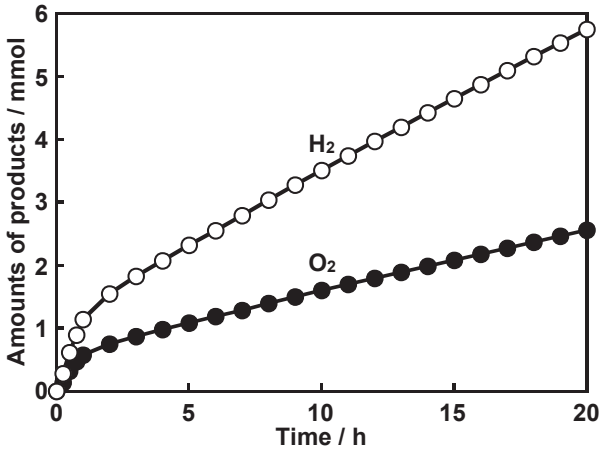

Figure 2-4 Water splitting over NiO(0.5 wt%)-loaded $KCaSrTa_5O_{15}$ photocatalyst. Photocatalyst: 0.5 g, reactant solution: water (350 mL) with Ar gas flow (30 mL min^{-1}), light source: a 400 W high-pressure mercury lamp, reactor: an inner irradiation cell made of quartz. $KCaSrTa_5O_{15}$ was prepared by a solid-state reaction at 1423 K for 10 h. NiO cocatalyst was loaded by an impregnation method.

Table 2-2 Photocatalytic CO_2 reduction over various cocatalysts-loaded $KCaSrTa_5O_{15}$.

Cocatalyst	Loading Condition	Activity / μmol h^{-1}		
		H_2	O_2	CO
None	-	116	48	0
NiO	Impregnation[a]	764	398	0
Ni	Photodeposition	111	58	0
Cu	Photodeposition	216	100	trace
Ru	Photodeposition	28	13	0
Rh	Photodeposition	43	19	0
Ag	Photodeposition	53	37	8.1
Ag	Impregnation[b]	55	28	5.5
Ag	Impregnation[b]+H_2 red.	96	48	1.0
Pt	Photodeposition	62	23	0
Au	Photodeposition	584	269	0

Photocatalyst: 0.5 g, cocatalysts: 0.5 wt%, loading conditions: photodeposition (*in situ*), impregnation ([a]573 K for 1 h in air, [b]723 K for 1 h in air), impregnation and subsequent H_2 reduction (773 K for 2 h in H_2 flow), reactant solution: water (350 mL) dissolved with CO_2 under 1 atm, light source: a 400 W high-pressure mercury lamp, reactor: an inner irradiation cell made of quartz. $KCaSrTa_5O_{15}$ was prepared by a solid-state reaction at 1423 K for 10 h.

splitting were loaded as observed for $BaLa_4Ti_4O_{15}$ photocatalyst.[15] No CO_2 reduction proceeded, when Ni, Ru, Rh, Pd, Pt and Au were loaded. When Cu cocatalyst was loaded, a small amount of CO evolved. In contrast, Ag-loaded $KCaSrTa_5O_{15}$ photocatalyst produced CO from CO_2 as a reduction product regardless of loading methods of the Ag cocatalyst. In particular, the highest activity for CO_2 reduction was observed, when Ag cocatalyst was loaded by photodeposition and impregnation methods as shown in Table 2-2 and Figure 2-5. The fact that CO_2 was reduced on the Ag-loaded $KCaSrTa_5O_{15}$, but not on the pristine $KCaSrTa_5O_{15}$, indicates that Ag cocatalyst works as a reduction site of CO_2. Metallic Ag is a good electrocatalyst for reduction of CO_2 to CO.[26] The process of CO_2 reduction to CO on the Ag cocatalyst would be similar to that on the Ag electrocatalyst[27-28] as observed for $BaLa_4Ti_4O_{15}$[15] and Zn-doped Ga_2O_3[16] photocatalysts. A CO_2 molecule is reduced to a CO_2^- adsorbed on Ag cocatalyst by a photoexcited electron. As a subsequent further reduction process of the adsorbed CO_2^- to CO, following possible ways can be considered. Although the redox potential of CO_2^- formation is −1.9 V[27], the redox potential showed become more positive due to stabilization by adsorption. The adsorbed CO_2^- is reacted with a H^+ ion in water to form an adsorbed –COOH. The adsorbed –COOH is subsequently reduced to become CO and OH− by an another electron.[27-28] H_2, O_2 and CO evolved steadily with a reaction time on the optimized Ag-loaded $KCaSrTa_5O_{15}$ photocatalyst as shown in Figure 2-6. The turnover number of electrons reacted for CO evolution to the number of the Ag atom in the cocatalyst calculated using the equation (1) was 8.6 at 20 h, and the ratio of electron to hole calculated using the equation (2) was unity. These results indicate that the CO_2 reduction over Ag-loaded $KCaSrTa_5O_{15}$ proceeded photocatalytically and water was consumed as an electron donor.

TON_{CO} = (The number of electrons consumed for CO formation) / (The total number of a Ag atom in cocatalyst on $KCaSrTa_5O_{15}$) (1)

e^-/h^+ = (The number of electrons consumed for H_2 and CO formation) / (The numbers of holes consumed for O_2 formation) (2)

It has been reported that methane forms from not CO_2 but an organic contamination adsorbed

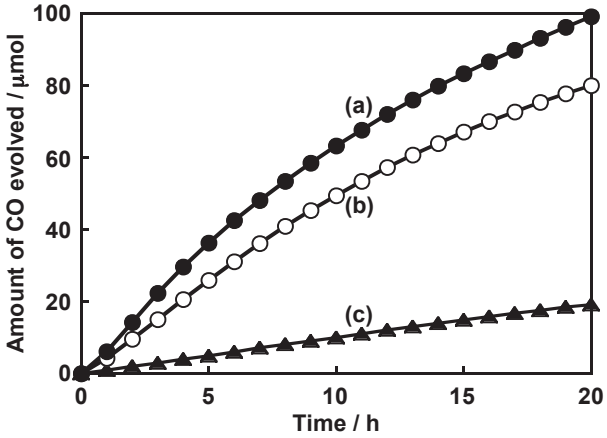

Figure 2-5 CO evolution from CO_2 over $KCaSrTa_5O_{15}$ photocatalysts with Ag cocatalysts loaded by (a) photodeposition, (b) impregnation and (c) impregnation and subsequent H_2 reduction. Photocatalyst: 0.5 g, reactant solution: water (350 mL), light source: a 400 W high-pressure mercury lamp, reactor: an inner irradiation cell made of quartz. $KCaSrTa_5O_{15}$ was prepared by a solid-state reaction at 1423 K for 10 h.

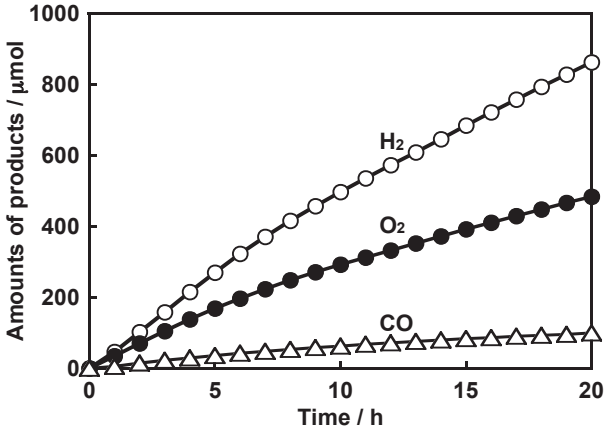

Figure 2-6 CO_2 reduction over Ag(0.5 wt%)-loaded $KCaSrTa_5O_{15}$ photocatalyst in an aqueous medium. Photocatalyst: 0.5 g, reactant solution: water (350 mL) with CO_2 gas flow (30 mL min^{-1}), light source: a 400 W high-pressure mercury lamp, reactor: an inner irradiation cell made of quartz. $KCaSrTa_5O_{15}$ was prepared by a solid-state reaction at 1423 K for 10 h. The Ag cocatalyst was loaded by a photodeposition.

on the photocatalyst surface.[29] Therefore, an isotope experiment using $^{13}CO_2$ was carried out to clarify the carbon source of CO formed. When the $^{13}CO_2$ gas was analyzed by a GC-MS using a MS-5A column, no peaks with mass numbers due to ^{12}CO and ^{13}CO were detected, indicating that the $^{13}CO_2$ gas contained negligible amounts of ^{12}CO and ^{13}CO. In contrast, photocatalytic reduction of $^{13}CO_2$ over Ag-loaded $KCaSrTa_5O_{15}$ photocatalyst gave ^{13}CO and no ^{12}CO as shown in Figure 2-7. Additionally, the ratio of electron to hole calculated from the products was about unity also in this isotopic experiment. Therefore, it was proven that CO was produced from CO_2 molecules over the Ag-loaded $KCaSrTa_5O_{15}$ photocatalyst.

2-3-1-3. Characterization of activated NiO and Ag cocatalysts on the surface of $KCaSrTa_5O_{15}$

NiO and Ag cocatalysts loaded on $KCaSrTa_5O_{15}$ before and after photocatalytic water splitting and CO_2 reduction were analyzed by scanning electron microscopy (SEM), X-ray photoelectron spectroscopy (XPS) and diffuse reflectance spectroscopy (DRS) in order to clarify the active states of these cocatalysts.

The particle size and morphology of NiO and Ni cocatalysts loaded on $KCaSrTa_5O_{15}$ photocatalysts were observed using SEM before and after photocatalytic water splitting as shown in Figure 2-8. A particle size of NiO loaded by an impregnation method was about 10 nm (Figure 2-8 (a)). Small particle sizes of metallic Ni remained after H_2 reduction, though a part of metallic Ni sintered (Figure 2-8 (c)). The metallic Ni aggregated after the photocatalytic water splitting, and nano-particles of Ni were hardly observed (Figure 2-8 (d)). The shape of Ni loaded by a photodeposition method was not spherical particle being clearly different from that loaded by an impregnation method (Figure 2-8 (e)). Thus, the particle size and the shape of NiO and/or Ni cocatalysts after photocatalytic water splitting depended on the loading methods.

Figure 2-9 shows DRS of NiO and Ni-loaded $KCaSrTa_5O_{15}$ before and after photocatalytic water splitting. Non-loaded $KCaSrTa_5O_{15}$ was white and possessed 302 nm of an absorption edge (Figure 2-9 (a)). A color of $KCaSrTa_5O_{15}$ loaded with NiO by an impregnation method was gray and the background of the DRS arose at visible and near IR regions (Figure 2-9 (b)). A color of

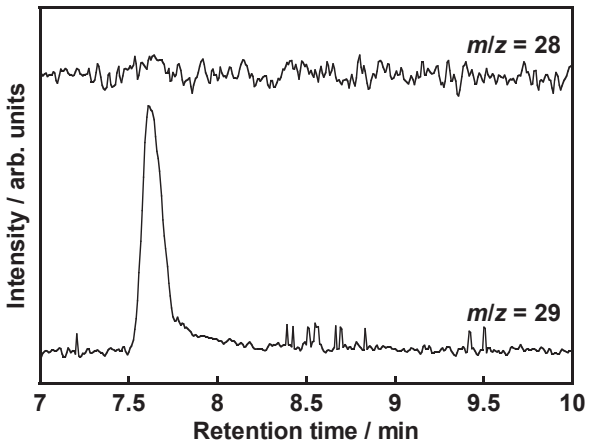

Figure 2-7 GC-MS analysis (MS-5A column) of CO produced by photocatalytic reduction of $^{13}CO_2$ over Ag(0.5 wt%)/$KCaSrTa_5O_{15}$. Photocatalyst: 0.5 g, reactant solution: water (350 mL), Ag cocatalyst was impregnated from $AgNO_3$ and calcination at 723 K for 1 h in air, light source: a 400 W high-pressure mercury lamp, reactor: an inner irradiation cell made of quartz. $KCaSrTa_5O_{15}$ was prepared by a solid-state reaction at 1423 K for 10 h.

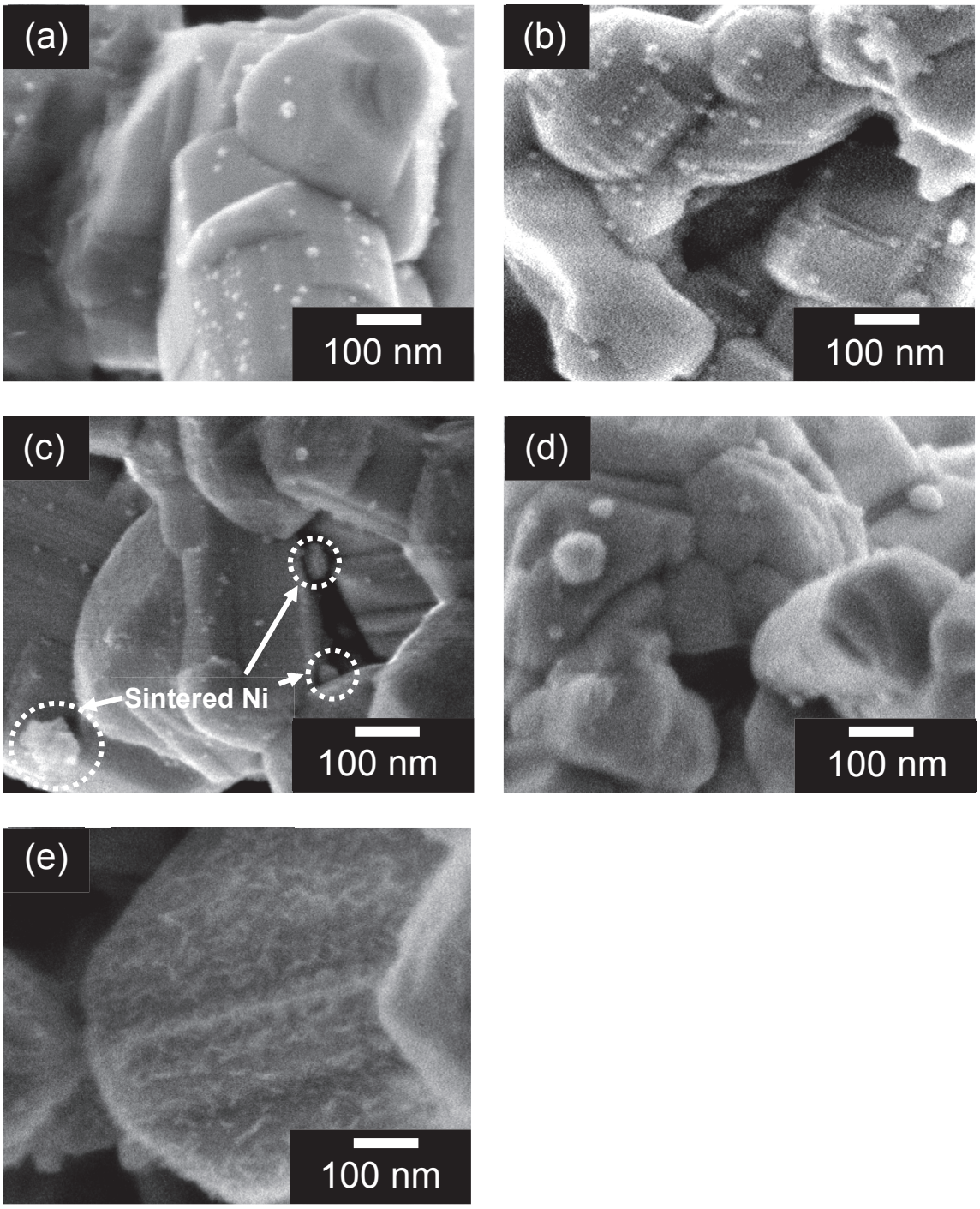

Figure 2-8 SEM images of NiO(0.5 wt%) and Ni(0.5 wt%)-loaded $KCaSrTa_5O_{15}$ by various loading methods before and after water splitting. (a) Before and (b) after water splitting for the sample prepared by an impregnation method, (c) before and (d) after water splitting for the sample prepared by an impregnation and subsequent H_2 reduction, (e) after water splitting for the sample prepared by a photodeposition. $KCaSrTa_5O_{15}$ was prepared by a solid-state reaction at 1423 K for 10 h.

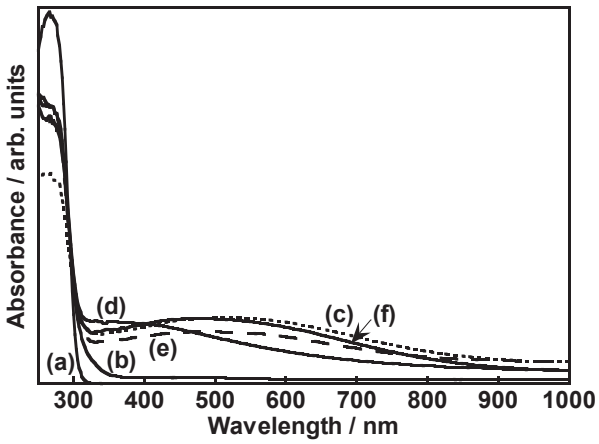

Figure 2-9 Diffuse reflectance spectra of (a) pristine $KCaSrTa_5O_{15}$ and (b)-(f) NiO(0.5 wt%) and Ni(0.5 wt%)-loaded $KCaSrTa_5O_{15}$ by various methods before and after water splitting. (b) Before and (c) after water splitting for the sample prepared by an impregnation method, (d) before and (e) after water splitting for the sample prepared by impregnation and subsequent H_2 reduction, (f) after water splitting for the sample prepared by a photodeposition. $KCaSrTa_5O_{15}$ was prepared by a solid-state reaction at 1423 K for 10 h.

$Ni/KCaSrTa_5O_{15}$ obtained by an impregnation and subsequent H_2 reduction was pale brown and gave a broad absorption band with a peak around 400 nm (Figure 2-9 (d)). All Ni or NiO-loaded photocatalysts were dark purple after photocatalytic water splitting giving broad absorption bands in visible light region (Figure 2-9 (c), (e) and (f)). This result suggests that the condition of nickel cocatalysts was similar to each other during photocatalytic water splitting regardless of the loading methods. The dark purple color did not quickly change after exposing to air.

Figure 2-10 shows XPS of Ni 2p of NiO and Ni cocatalysts loaded on $KCaSrTa_5O_{15}$ before and after photocatalytic water splitting. Binding energies of standard samples of metallic Ni, NiO and $Ni(OH)_2$ agreed with those of previous reports.[30] The surface of the standard NiO powder was covered with surface hydroxyl groups. NiO loaded on $KCaSrTa_5O_{15}$ by an impregnation method also gave peaks due to NiO and $Ni(OH)_2$ (Figure 2-10 (a)). $Ni/KCaSrTa_5O_{15}$ obtained by an impregnation and subsequent H_2 reduction gave XPS signals due to metallic Ni with NiO (Figure 2-10 (c)). All samples showed XPS signals mainly due to $Ni(OH)_2$ after photocatalytic water splitting (Figure 2-10 (b), (d) and (e)). $Ni(OH)_2$ is generally green, not dark purple as mentioned above. DRS of the samples after photocatalytic water splitting were different from that of $Ni(OH)_2$ as shown in Figure 2-11. Therefore, the XPS signals due to $Ni(OH)_2$ observed for the samples after photocatalytic water splitting indicates the existence of not bulky $Ni(OH)_2$ but the surface nickel hydroxide as observed for a $NiO_x/SrTiO_3$ photocatalyst.[30] It has been reported that a color of a $NiO/InBO_4$ photocatalyst also changed to dark purple after photocatalytic water splitting.[31] Ultra fine NiO cocatalyst loaded on a $NaTaO_3$:La photocatalyst gives visible light absorption bands which are different from that of $Ni(OH)_2$.[32] Thus, active NiO cocatalyst loaded on the photocatalysts with wide band gaps has a unique character.

The impregnation method for loading the nickel cocatalyst was more effective than impregnation and subsequent H_2 reduction, and photodeposition methods for water splitting over the $KCaSrTa_5O_{15}$ photocatalyst as shown in Table 2-1. SEM and XPS measurements suggested that the most active $KCaSrTa_5O_{15}$ photocatalyst possessed the cocatalyst of fine NiO particles covered with surface nickel hydroxide.

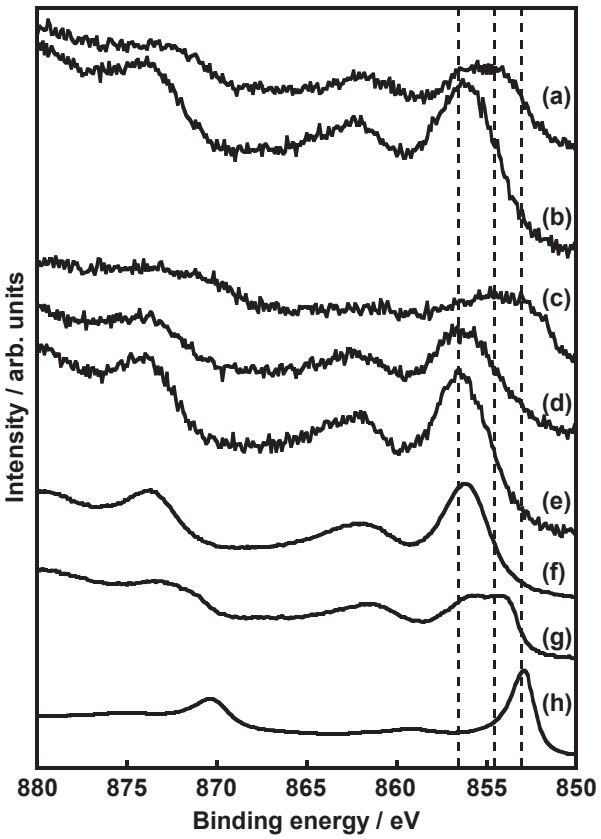

Figure 2-10 X-ray photoelectron spectroscopy of Ni 2p of NiO(0.5 wt%) and Ni(0.5 wt%)-loaded $KCaSrTa_5O_{15}$. Nickel cocatalyst on $KCaSrTa_5O_{15}$ (a) before and (b) after water splitting for the sample prepared by an impregnation method, (c) before and (d) after water splitting for the sample prepared by an impregnation and subsequent H_2 reduction, (e) after water splitting for the sample prepared by a photodeposition. Standard sample of (f) $Ni(OH)_2$, (g) NiO, (h) metallic Ni foil. Reference data[30] are indicated as dashed lines respectively: Ni metal (853.1 eV), NiO (854.5 eV), $Ni(OH)_2$ (856.6 eV).

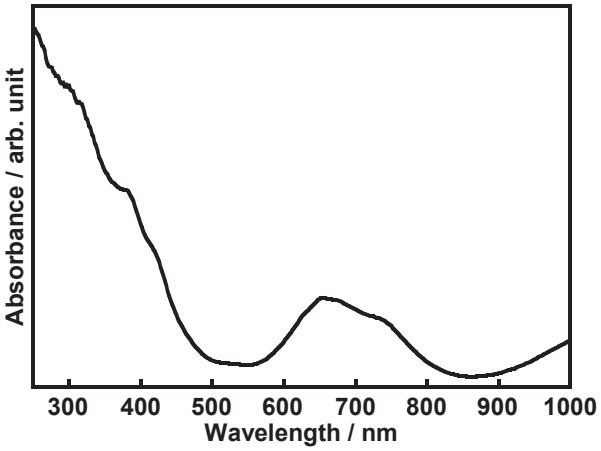

Figure 2-11 Diffuse reflectance spectrum of $Ni(OH)_2$ powder.

SEM images of Ag loaded on $KCaSrTa_5O_{15}$ photocatalysts were also observed before and after photocatalytic CO_2 reduction as shown in Figure 2-12. An impregnation method gave Ag cocatalyst with about 10 nm of the particle size before and after H_2 reduction (Figure 2-12 (a) and (c)). The Ag cocatalyst aggregated after photocatalytic CO_2 reduction (Figure 2-12 (b) and (d)). The growth of some Ag particles reached up to 50─100 nm. The particle size of Ag after photocatalytic CO_2 reduction was similar to that obtained by a photodeposition method (Figure 2-12 (e) and (f)).

Nano-sized metallic Ag particle generally gives a surface plasmonic absorption band in visible light region.[33] Therefore, DRS of samples before and after photocatalytic CO_2 reduction were measured as shown in Figure 2-13. Ag cocatalyst obtained by H_2 reduction was orange and gave a characteristic surface plasmonic absorption spectrum (Figure 2-13 (c)), while such a spectrum was not observed for Ag cocatalyst obtained by an impregnation method (Figure 2-13 (a)). All samples after photocatalytic CO_2 reduction gave similar absorption spectra to the sample obtained by H_2 reduction (Figure 2-13 (b), (d), (e) and (f)), although the intensities of the absorption spectra decreased after the photocatalytic reduction of CO_2. This result suggests dissolution and re-deposition of Ag during the photocatalytic reaction giving aggregated Ag particles as observed by SEM. Ag cocatalyst prepared by an impregnation method after the photocatalytic reduction of CO_2 also gave the similar absorption spectrum indicating that the Ag cocatalyst was reduced to fine metallic particles by photogenerated electrons. These results indicate that the metallic Ag giving the surface plasmonic absorption spectrum is an active site for the photocatalytic CO_2 reduction.

2-3-2. Development of the single crystalline nanorod $KCaSrTa_5O_{15}$ photocatalyst prepared by a polymerized complex method

2-3-2-1. Characterization of the material properties of single crystalline nanorod $KCaSrTa_5O_{15}$ prepared by a polymerized complex method

Figure 2-14 shows XRD patterns of PC-$KCaSrTa_5O_{15}$ prepared at different temperatures. A single phase of $KCaSrTa_5O_{15}$ was not obtained by a solid-state reaction even at 1423 K. In contrast, the polymerized complex method gave the single phase even at 1173 K for 10 h (Figure 2-14(c)).

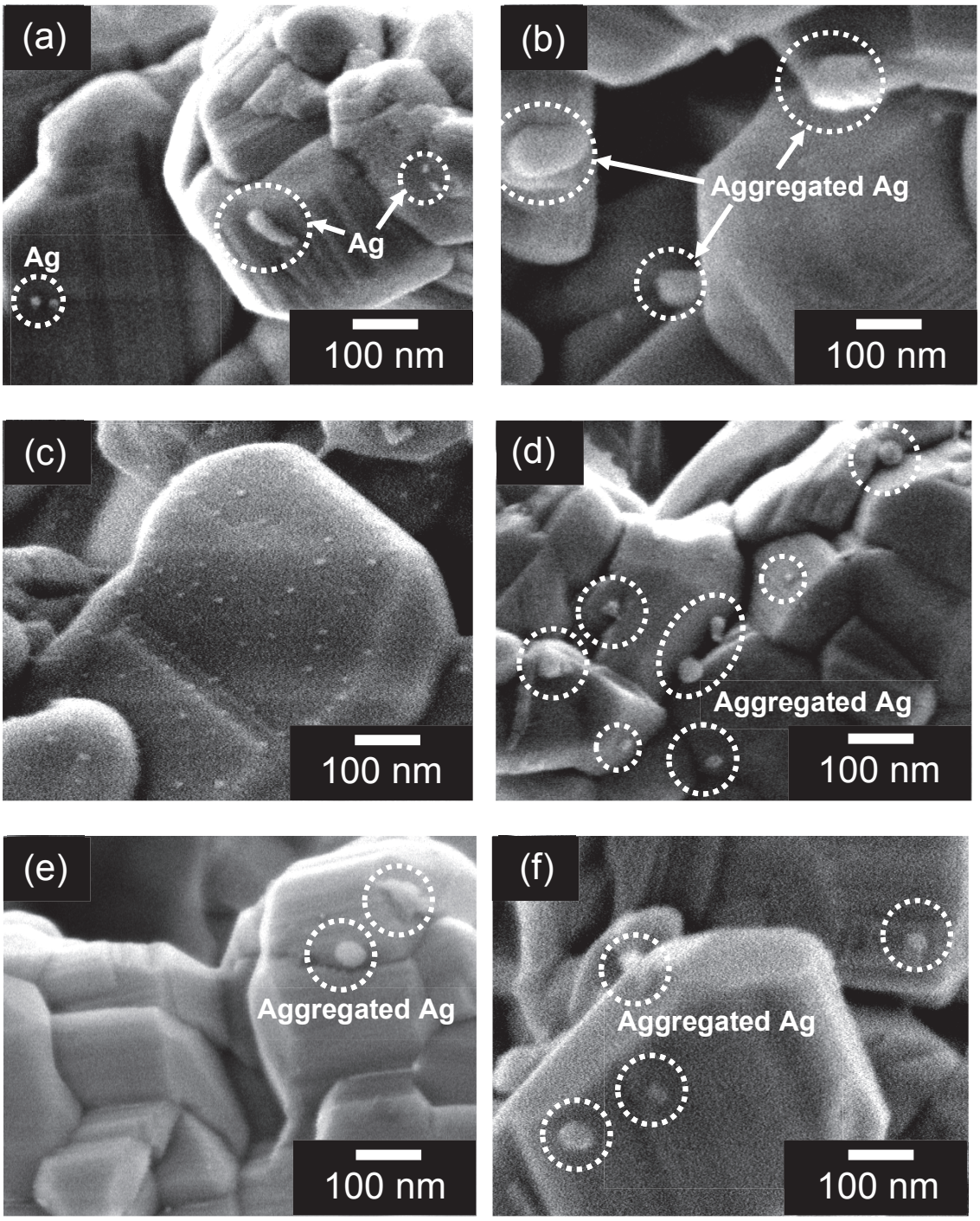

Figure 2-12 SEM images of Ag(0.5 wt%)-loaded $KCaSrTa_5O_{15}$ by various loading methods before and after CO_2 reduction. (a) Before and (b) after CO_2 reduction for the sample prepared by an impregnation method, (c) before and (d) after CO_2 reduction for the sample prepared by an impregnation and subsequent H_2 reduction, after CO_2 reduction for the sample prepared by a photodeposition (*in situ*) at (e) 2h and (f) 20h. $KCaSrTa_5O_{15}$ was prepared by a solid-state reaction at 1423 K for 10 h.

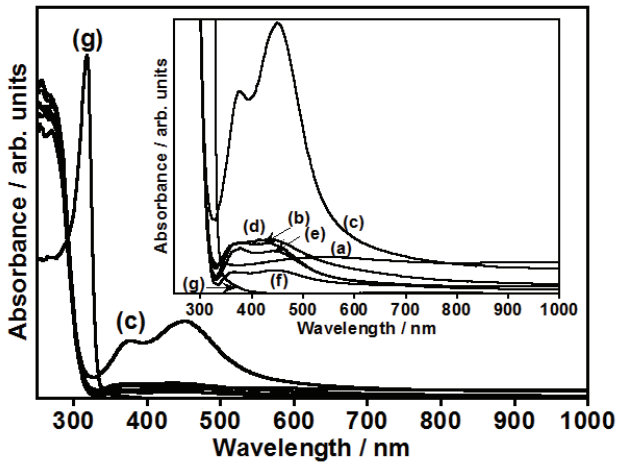

Figure 2-13 Diffuse reflectance spectra of Ag(0.5 wt%)-loaded $KCaSrTa_5O_{15}$ by various methods before and after CO_2 reduction. (a) Before and (b) after CO_2 reduction for the sample prepared by an impregnation method, (c) before and (d) after CO_2 reduction for the sample prepared by an impregnation and subsequent H_2 reduction, after CO_2 reduction for the sample prepared by a photodeposition at (e) 2h and (f) 20h, and (g) metallic and bulky Ag. $KCaSrTa_5O_{15}$ was prepared by a solid-state reaction at 1423 K for 10 h.

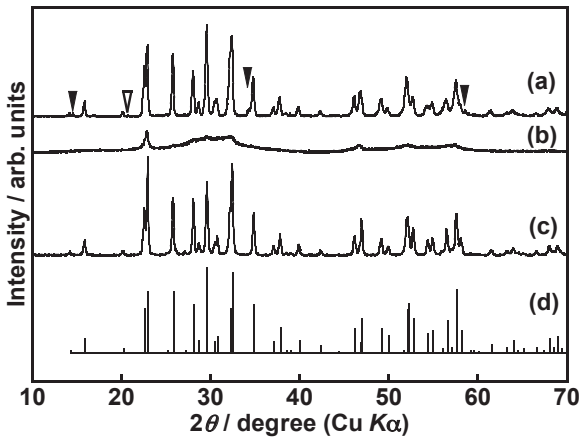

Figure 2-14. X-ray diffraction patterns of $KCaSrTa_5O_{15}$ prepared by (a) a solid-state reaction at 1423 K for 10 h, and a polymerized complex method at (b) 773 K for 1 h, and (c) 1173 K for 10 h. (d) $KCaSrTa_5O_{15}$ (PDF: 40-351). Closed and open triangles indicate $Ca_2Ta_2O_7$ (PDF: 53-743) and unknown phase as impurities, respectively

The crystallinity of PC-$KCaSrTa_5O_{15}$ was higher than that of SSR-$KCaSrTa_5O_{15}$ judging from the full width at half maximum of XRD patterns, even if the preparation temperature was lower. The specific surface areas of PC-$KCaSrTa_5O_{15}$ and SSR-$KCaSrTa_5O_{15}$ were 17.4 and 2.4 $m^2\ g^{-1}$, respectively. It suggests that the PC-$KCaSrTa_5O_{15}$ particles are small. It was confirmed that the polymerized complex method was also useful for the preparation of the $KCaSrTa_5O_{15}$ photocatalyst with high quality as observed for $K_2LaNb_5O_{15}$ with the same crystal structure.

Figure 2-15 shows SEM and TEM of SSR-$KCaSrTa_5O_{15}$ and PC-$KCaSrTa_5O_{15}$. The SSR-$KCaSrTa_5O_{15}$ particles aggregated consisting of primary particles with 100–300 nm of the particle size and no special shape (Figure 2-15(a)). In contrast, the PC-$KCaSrTa_5O_{15}$ particles were nanorods with 40–100 nm of the diameter and 100–300 nm of the length (Figure 2-15(b) and (c)). This nanorod shape reflected the tungsten bronze structure. TEM showed 0.384 nm of a fringe pattern due to a (001) face of tungsten bronze structure as shown in Figure 2-15(d). Selected-area electron diffraction patterns with regular spots shown in Figure 2-15(e) indicated that the nanorod particle was a single crystal growing to the direction of a c-axis of the tungsten bronze structure as shown in Figure 2-16.

Figure 2-17 shows diffuse reflectance spectra of SSR-$KCaSrTa_5O_{15}$ and PC-$KCaSrTa_5O_{15}$. The band gaps were 4.09 and 4.13 eV, respectively.

A migration process of photogenerated carriers affects the activity in semiconductor photocatalysts.[17] Luminescent Ln^{3+} such as Tb^{3+} and Pr^{3+} can be used as a probe to examine the carrier migration process.[20, 37-39] For example, the usage of Pr^{3+} revealed that the diffusion length of photogenerated carriers in a $BaLa_4Ti_4O_{15}$ photocatalyst was longer than that of $CaLa_4Ti_4O_{15}$ agreeing with the order in the photocatalytic activity for water splitting.[20] Therefore, we employed Tb^{3+} as a probe to see the carrier behavior in SSR-$KCaSrTa_5O_{15}$ and PC-$KCaSrTa_5O_{15}$. XRD and SEM revealed that the Tb-doping did not affect the crystal phase, the particle size, and the morphology of the SSR-$KCaSrTa_5O_{15}$ and PC-$KCaSrTa_5O_{15}$ particles as shown in Figures 2-18 and 2-19. It is reported that La^{3+} and Ce^{3+} ions exist at the A1 sites in tungsten bronze structure in $K_2LaNb_5O_{15}$ and $K_2CeTa_5O_{15}$ (Figure 2-16).[40, 41] Therefore, the Tb^{3+} ions should also be doped at

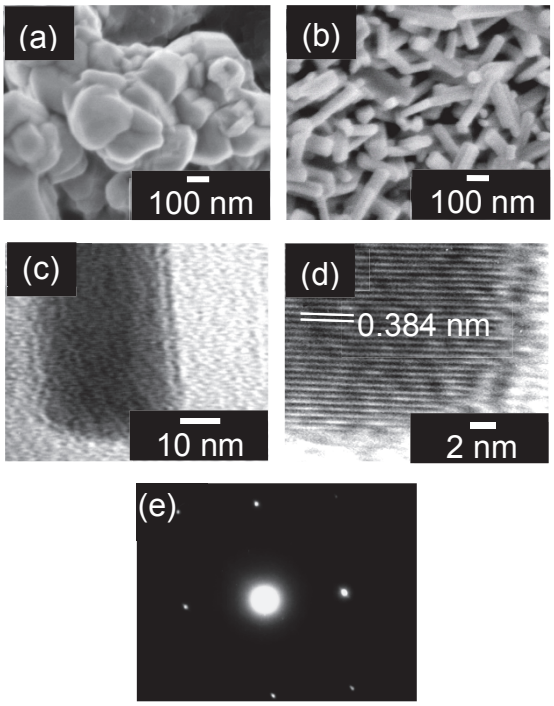

Figure 2-15. SEM images of $KCaSrTa_5O_{15}$ prepared by (a) a solid-state reaction and (b) a polymerized complex method, and (c, d) TEM images of $KCaSrTa_5O_{15}$ prepared by a polymerized complex method. (e) Selected-area electron diffraction pattern of $KCaSrTa_5O_{15}$ prepared by a polymerized complex method. Preparation conditions: SSR; 1423 K for 10 h, PC; 1173 K for 10 h.

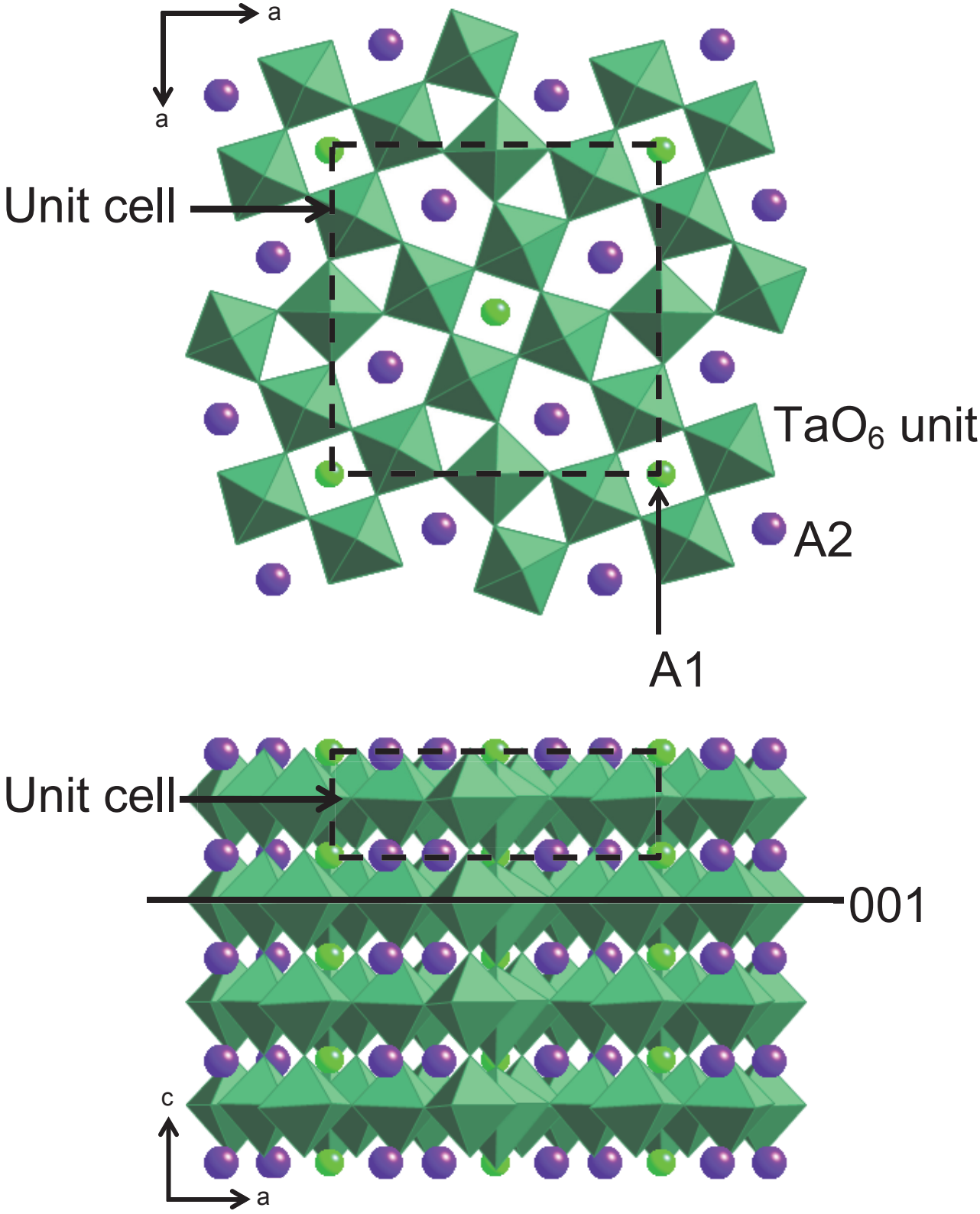

Figure 2-16. Crystal structure of tungsten bronze indicated as $A1A2_2Ta_5O_{15}$.[41]

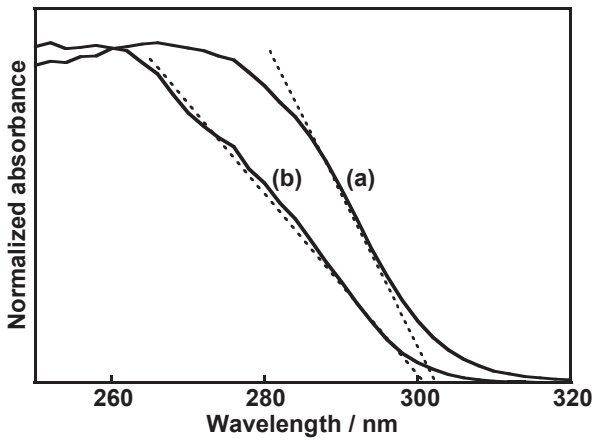

Figure 2-17. Diffuse reflectance spectra of $KCaSrTa_5O_{15}$ prepared by (a) a solid-state reaction, and (b) a polymerized complex method. Preparation conditions: SSR; 1423 K for 10 h, PC; 1173 K for 10 h.

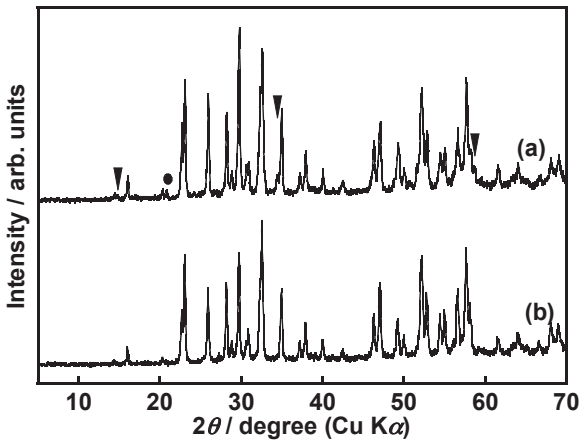

Figure 2-18. X-ray diffraction patterns of Tb(0.03 atom%)-doped $KCaSrTa_5O_{15}$ prepared by (a) a solid-state reaction and (b) a polymerized complex method. Closed triangle and circles represent $Ca_2Ta_2O_7$ (PDF: 53-743) of an impurity and an unknown phase, respectively. Preparation conditions: SSR; 1423 K for 10 h, PC; 1173 K for 10 h.

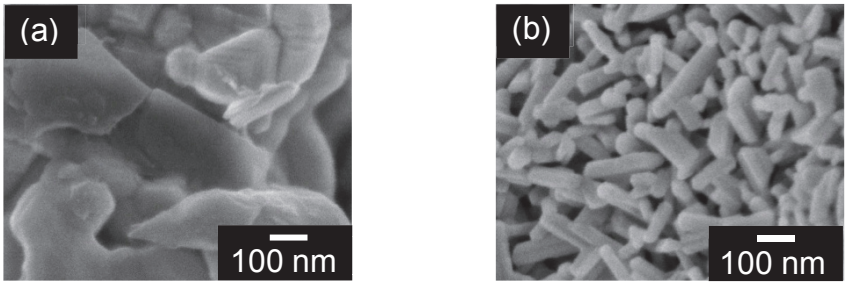

Figure 2-19. SEM images of Tb(0.03 atom%)-doped $KCaSrTa_5O_{15}$ prepared by (a) a solid-state reaction and (b) a polymerized complex method. Preparation conditions: SSR; 1423 K for 10 h, PC; 1173 K for 10 h.

the A1 site in $KCaSrTa_5O_{15}$. Tb-doped SSR-$KCaSrTa_5O_{15}$ and PC-$KCaSrTa_5O_{15}$ were denoted as SSR-$KCaSrTa_5O_{15}$:Tb and PC-$KCaSrTa_5O_{15}$:Tb, respectively.

First, we examined excitation and emission spectra of nondoped SSR-$KCaSrTa_5O_{15}$ and PC-$KCaSrTa_5O_{15}$ at 77 K in vacuum as shown in Figure 2-20(A). Those samples gave broad yellow emissions. The luminescence was not observed at room temperature. Onsets of the excitation spectra agreed with those of diffuse reflectance spectra indicating that the yellow emissions were due to radiative transition by the band gap excitation. This is a typical host emission by the host excitation. Figure 2-20(B) shows excitation and emission spectra of SSR-$KCaSrTa_5O_{15}$:Tb and PC-$KCaSrTa_5O_{15}$:Tb at room temperature. Green emissions due to $^5D_4 \rightarrow {}^7F_6$ (480–500 nm) and $^5D_4 \rightarrow {}^7F_5$ (530–560 nm) were observed by host excitation at 290 nm. This result indicates that electrons and holes photogenerated in the bulk migrate to the Tb^{3+} ions resulting in the radiative transition. In more detail, after photogenerated holes are trapped at Tb^{3+} to form Tb^{4+}, they recombine with migrating electrons at the Tb^{4+} to form Tb^{3+} in an excited state to give luminescence. The intensity of the Tb^{3+} emission of PC-$KCaSrTa_5O_{15}$:Tb was much higher than that of SSR-$KCaSrTa_5O_{15}$:Tb. The green emission of the PC-$KCaSrTa_5O_{15}$:Tb was strong enough for being visual at room temperature as shown in Figure 2-21. These results indicate that the number of the recombination center for nonratiative transition for PC-$KCaSrTa_5O_{15}$:Tb was smaller than that of SSR-$KCaSrTa_5O_{15}$:Tb. Figure 2-22 shows the proposed mechanism derived from the photoluminescence behavior for the carrier migration in the PC-$KCaSrTa_5O_{15}$:Tb and SSR-$KCaSrTa_5O_{15}$:Tb particles. A grain boundary would work as a recombination center accompanied with nonradiative transition.[17] XRD, SEM, and TEM observations support that the grain boundary hardly exists in the single crystalline nanorod of PC-$KCaSrTa_5O_{15}$:Tb resulting in the suppression of nonratiative transition and the high intensity of photoluminescence as shown in Figure 2-22(a). In contrast, SSR-$KCaSrTa_5O_{15}$:Tb possessed a lot of grain boundaries because it was a polycrystalline particle and primary particles aggregated. Photogenerated carriers recombine at the defect of the grain boundary resulting in the decrease in those carriers that can reach the Tb^{3+} ions of the luminescence center as shown in Figure 2-22(b). Therefore, the intensity of

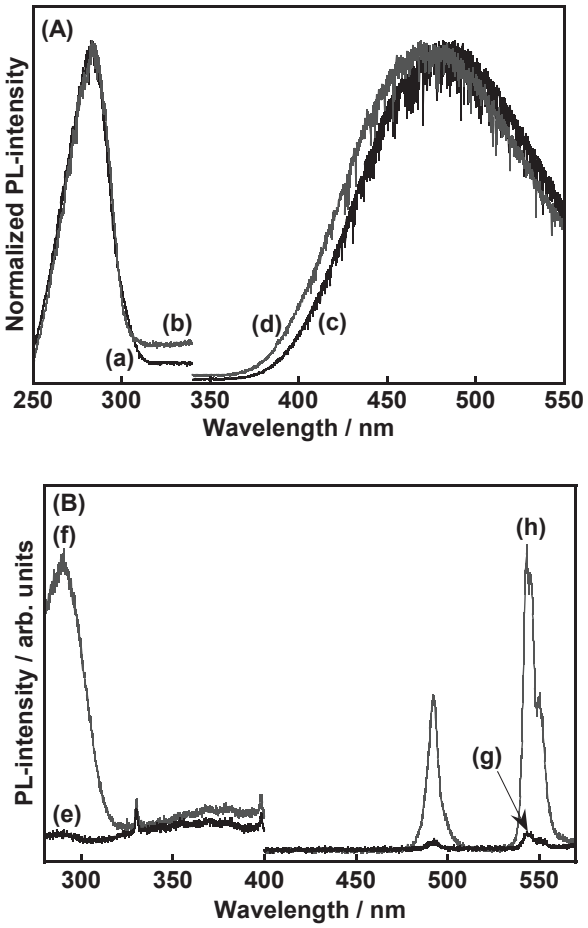

Figure 2-20. Emission and excitation spectra of (A) $KCaSrTa_5O_{15}$ at 77 K in vacuum and (B) Tb(0.03%)-doped $KCaSrTa_5O_{15}$ at room temperature. The excitation spectra of (a) SSR-$KCaSrTa_5O_{15}$ and (b) PC-$KCaSrTa_5O_{15}$ were obtained by monitoring at 475 nm. The emission spectra of (c) SSR-$KCaSrTa_5O_{15}$ and (d) PC-$KCaSrTa_5O_{15}$ were obtained by excitation at 285 nm. The excitation spectra of (e) SSR-$KCaSrTa_5O_{15}$:Tb and (f) PC-$KCaSrTa_5O_{15}$:Tb were obtained by monitoring at 543 nm. The emission spectra of (g) SSR-$KCaSrTa_5O_{15}$:Tb and (h) PC-$KCaSrTa_5O_{15}$:Tb were obtained by excitation at 290 nm. Preparation conditions: SSR; 1423 K for 10 h, PC; 1173 K for 10 h.

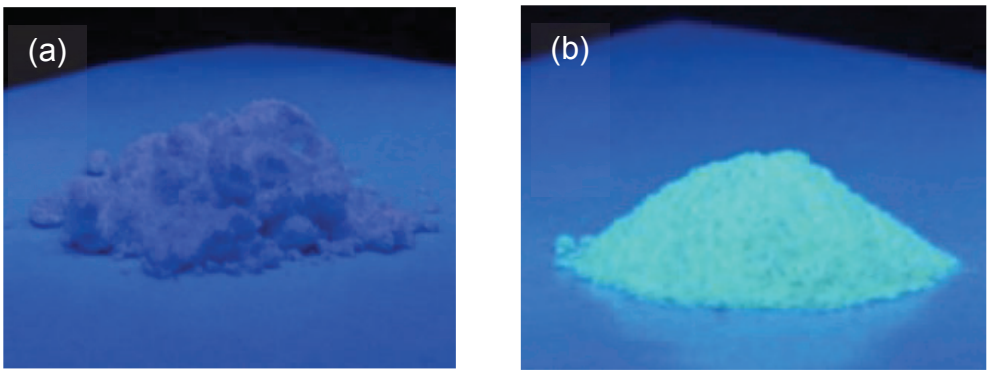

Figure 2-21. Photoluminescence at room temperature of Tb(0.03 atom%)-doped $KCaSrTa_5O_{15}$ prepared by (a) a solid-state reaction and (b) a polymerized complex method. Excitation wavelength was 254 nm. Preparation conditions: SSR; 1423 K for 10 h, PC; 1173 K for 10 h.

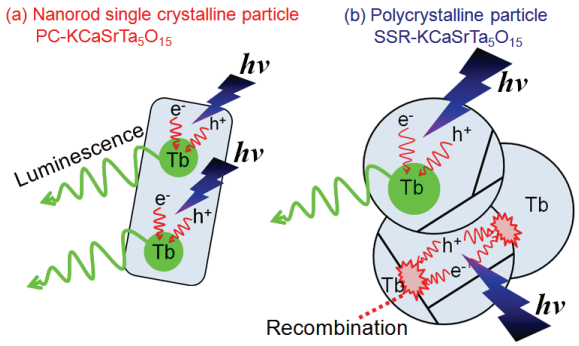

Figure 2-22. Proposed mechanism of carrier migration in single crystalline nanorod and polycrystalline particle of $KCaSrTa_5O_{15}$.

photoluminescence of SSR-$KCaSrTa_5O_{15}$:Tb was low.

2-3-2-2. Photocatalytic water splitting and CO_2 reduction over single crystalline nanorod $KCaSrTa_5O_{15}$ prepared by a polymerized complex method

Table 2-3 shows photocatalytic activity for water splitting over PC-$KCaSrTa_5O_{15}$ and SSR-$KCaSrTa_5O_{15}$. PC-$KCaSrTa_5O_{15}$ showed the activity even without cocatalyst as well as SSR-$KCaSrTa_5O_{15}$. The activity of PC-$KCaSrTa_5O_{15}$ was higher than that of SSR-$KCaSrTa_5O_{15}$. The activity of PC-$KCaSrTa_5O_{15}$ drastically increased when a NiO cocatalyst was loaded. The optimum amount of NiO loading was 0.2 wt% as shown in Figure 2-23. NiO-cocatalyst-loaded PC-$KCaSrTa_5O_{15}$ (NiO/PC-$KCaSrTa_5O_{15}$) showed higher activity than NiO-loaded SSR-$KCaSrTa_5O_{15}$ at any loading amounts. This is due to the less recombination probability at the grain boundary in PC-$KCaSrTa_5O_{15}$ than SSR-$KCaSrTa_5O_{15}$ as shown in Figure 2-22. Figure 2-24 shows water splitting over the optimized NiO/PC-$KCaSrTa_5O_{15}$ photocatalyst. Although the photocatalytic activity decreased with the reaction time, the initial activities for H_2 and O_2 evolution using 400-W high-pressure mercury lamp were 4.30 mmol h^{-1} and 2.26 mmol h^{-1}, respectively. The apparent quantum yield at 254 nm was 6.6%. It was 2.9 times higher than that of SSR-$KCaSrTa_5O_{15}$.

CO_2 reduction using water as an electron donor was conducted by the PC-$KCaSrTa_5O_{15}$ photocatalyst optimized for water splitting as shown in Table 2-4. Nonloaded and NiO/PC-$KCaSrTa_5O_{15}$ did not show the activity for the CO_2 reduction. When a Ag cocatalyst was loaded, CO_2 reduction proceeded to form CO. A Ag electrode is an excellent electrocatalyst for CO_2 reduction to form CO.[26-28] The Ag cocatalyst was also effective for $BaLa_4Ti_4O_{15}$,[15] Zn-doped Ga_2O_3[16] and SSR-$KCaSrTa_5O_{15}$ photocatalysts. When $NaHCO_3$ was added in the aqueous solution, the activity for CO formation was improved to give 87% of the selectivity defined by the equation (3).

Table 2-3. Photocatalytic water splitting over SSR- and PC-$KCaSrTa_5O_{15}$ loaded with NiO cocatalyst

Preparation Method	Cocatalyst (wt%)	Activity / mmol h^{-1}	
		H_2	O_2
SSR	None	0.10	0.04
SSR	NiO (0.5)	1.34	0.70
PC	None	0.17	0.08
PC	NiO (0.2)	4.30	2.26

Catalyst: 0.5 g, loading condition: impregnation (573 K for 1 h in air), reactant solution: 350 mL of water, system: an Ar gas flow system using an inner irradiation cell made of quartz with a 400 W high-pressure mercury lamp. Preparation conditions: SSR; 1423 K for 10 h, PC; 1173 K for 10 h.

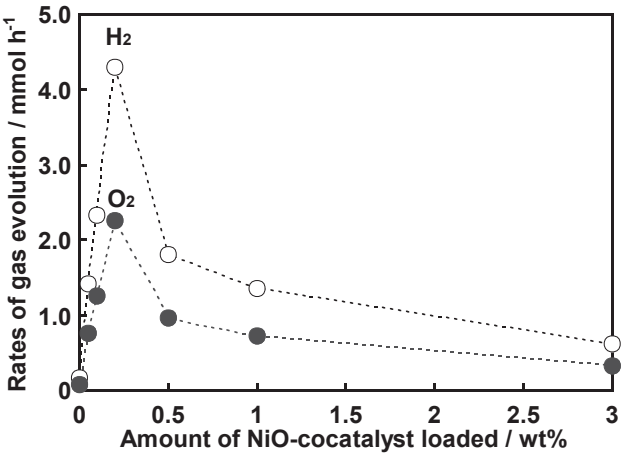

Figure 2-23. Effect of a loading amount of NiO-cocatalyst on water splitting over $KCaSrTa_5O_{15}$ photocatalyst prepared at 1173 K for 10 h by a polymerized complex method. Catalyst: 0.5 g, loading condition: impregnation at 573 K for 1 h in air, reactant solution: 350 mL of water, system: an Ar gas flow system using an inner irradiation cell made of quartz with a 400 W high-pressure mercury lamp.

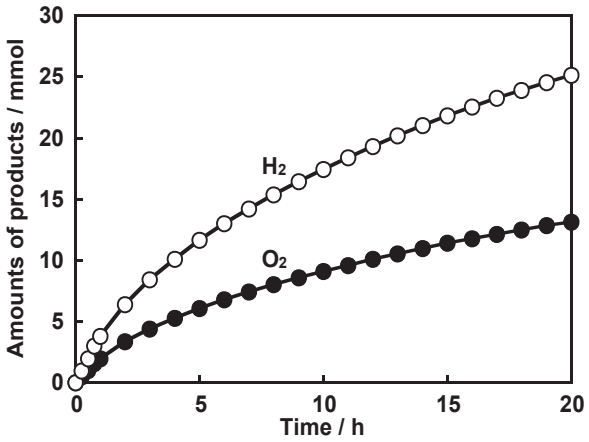

Figure 2-24. Water splitting over NiO(0.2 wt%)-loaded $KCaSrTa_5O_{15}$ nanorod photocatalyst prepared at 1173 K for 10 h by a polymerized complex method. Catalyst: 0.5 g, reactant solution: 350 mL of water, system: an Ar gas flow system using an inner irradiation cell made of quartz with a 400 W high-pressure mercury lamp. NiO-cocatalyst was loaded by an impregnation method.

Table 2-4. Photocatalytic CO_2 reduction over PC-$KCaSrTa_5O_{15}$ loaded with NiO and Ag cocatalysts

Cocatalyst (wt%)	Loading Temperature / K	Additive	Activity / μmol h^{-1}			CO selectivity %
			H_2	O_2	CO	
None	–	None	79	40	0	–
NiO (0.2)	573	None	2001	1077	0	–
NiO (0.2)	573	$NaHCO_3$	1198	657	Trace	–
Ag (0.5)	723	None	57	30	9	14
Ag (0.5)	723	$NaHCO_3$	15	46	97	87

Catalyst: 0.5 g, loading method: impregnation, reactant solution: 350 mL of water and 0.1 mol L^{-1} of $NaHCO_{3\ aq.}$ dissolved with 1 atm of CO_2, system: a CO_2 gas flow system using an inner irradiation cell made of quartz with a 400 W high-pressure mercury lamp. Preparation conditions: 1173 K for 10 h.

CO selectivity (%) = (Rate of CO formation/μmol h^{-1}) / (Sum of rates of H_2 and CO formation/μmol h^{-1})×100 (3)

In the case of Ag-loaded $NaTaO_3$:Sr, the supply of CO_2 molecules to the Ag-cocatalyst is enhanced in the presence of $NaHCO_3$ resulting in the significant increase in the selectivity to CO formation.[42] In contrast, CO formation was not observed for NiO/PC-$KCaSrTa_5O_{15}$ even in the presence of $NaHCO_3$. Figure 2-25 shows photocatalytic CO_2 reduction over Ag/PC-$KCaSrTa_5O_{15}$ in the presence of $NaHCO_3$. CO, H_2 and O_2 evolved, while activity for CO evolution decreased with the reaction time. TON_{CO} and e^-/h^+ calculated from equations (1) and (2) were 56 and 1.1 at 10 h, respectively. This result indicates that the CO_2 reduction proceeds using water as an electron donor.

Diffuse reflectance spectra of Ag-cocatalyst-loaded PC-$KCaSrTa_5O_{15}$ (Ag/PC-$KCaSrTa_5O_{15}$) before and after photocatalytic CO_2 reduction were measured to examine the state of the Ag-cocatalyst as shown in Figure 2-26. Ag/PC-$KCaSrTa_5O_{15}$ before CO_2 reduction did not show surface plasmonic absorption as shown in Figure 2-26(b). In contrast, Ag/PC-$KCaSrTa_5O_{15}$ after the reaction showed surface plasmonic absorption around 330–600 nm as shown in Figure 2-26(c). This result indicates that the metallic fine Ag-cocatalyst with a small particle size to show the surface plasmonic absorption is the active site for the CO_2 reduction for the PC-$KCaSrTa_5O_{15}$ photocatalyst in an aqueous $NaHCO_3$ solution as well as for $BaLa_4Ti_4O_{15}$[15] and SSR-$KCaSrTa_5O_{15}$. It is important in photocatalytic reduction of CO_2 to use $^{13}CO_2$ to see the carbon source of the reduction products.[29] Only ^{13}CO was obtained by reduction of $^{13}CO_2$ on the Ag/PC-$KCaSrTa_5O_{15}$ photocatalyst. Thus, it was confirmed that not contamination but CO_2 was the carbon source of formed CO.

2-4. Conclusions

$KCaSrTa_5O_{15}$ (BG = 4.1 eV) with tungsten bronze structure has arisen as a new photocatalyst for water splitting and CO_2 reduction under UV light irradiation. $KCaSrTa_5O_{15}$ showed activity for water splitting without cocatalyst. In addition, NiO was an effective cocatalyst. The NiO cocatalyst activated during water splitting was dark purple and possessed a Ni hydroxide-shell/NiO-core

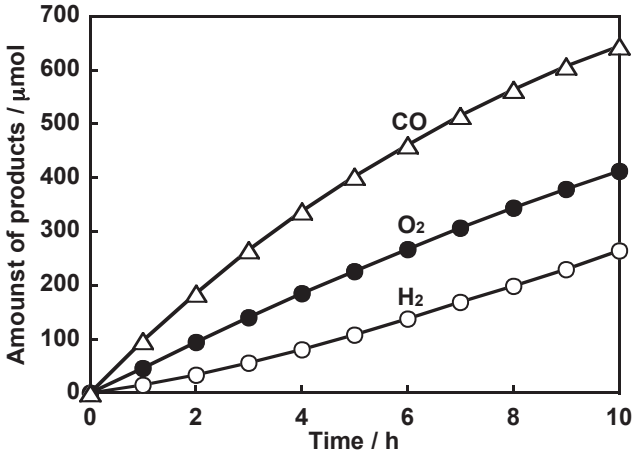

Figure 2-25. CO_2 reduction in an aqueous $NaHCO_3$ solution over Ag(0.5 wt%)-loaded $KCaSrTa_5O_{15}$ nanorod photocatalyst prepared at 1173 K for 10 h by a polymerized complex method. Catalyst: 0.5 g, reactant solution: 0.1 mol L^{-1} of $NaHCO_{3\ aq.}$ (350 mL) dissolved with 1 atm of CO_2, system: a CO_2 gas flow system using an inner irradiation cell made of quartz with a 400 W high-pressure mercury lamp. Ag-cocatalyst was loaded by an impregnation method.

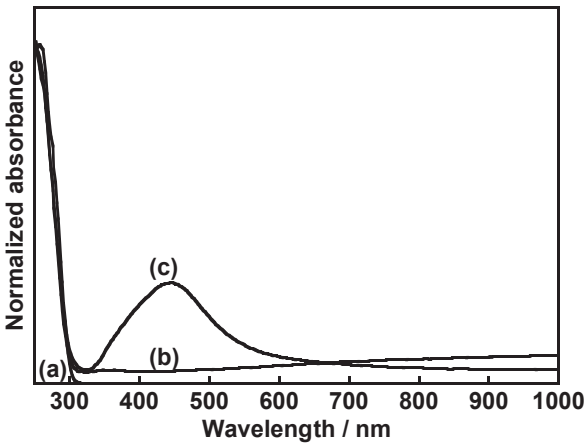

Figure 2-26. Diffuse reflectance spectra of (a) pristine $KCaSrTa_5O_{15}$ and Ag(0.5 wt%)-loaded $KCaSrTa_5O_{15}$ nanorods (b) before and (c) after 10 h of photocatalytic CO_2 reduction in an aqueous $NaHCO_3$ solution. Preparation condition of $KCaSrTa_5O_{15}$ nanorod: a polymerized complex method at 1173 K for 10 h.

structure as an active site for water reduction. The apparent quantum yield of optimized NiO-loaded $KCaSrTa_5O_{15}$ was 2.3% at 254 nm for the water splitting. On the other hand, Ag-loaded $KCaSrTa_5O_{15}$ photocatalyst was active for CO_2 reduction to CO in an aqueous medium. The Ag cocatalyst activated during CO_2 reduction gave surface plasmonic absorption band in visible light region suggesting that fine metallic Ag particle is the active site for the CO_2 reduction. Isotope experiment using $^{13}CO_2$ revealed that the carbon source of produced CO was CO_2 molecules. Moreover, a stoichiometric amount of O_2 evolution and TON_{CO} calculated from products was larger than 1 indicating that the CO_2 reduction to CO photocatalytically proceeded using water as an electron donor. Moreover, $KCaSrTa_5O_{15}$ single crystalline nanorod photocatalysts prepared by a polymerized complex method showed higher activities for water splitting than $KCaSrTa_5O_{15}$ prepared by a solid-state reaction with loading NiO-cocatalyst. The $KCaSrTa_5O_{15}$ nanorod showed photocatalytic activity for CO_2 reduction in an aqueous medium, when Ag-cocatalyst was loaded. The CO_2 reduction was enhanced by addition of $NaHCO_3$ in the reactant solution giving about 90% of the selectivity for CO formation. Photoluminescence measurement using Tb^{3+} as a probe for migration of electron-hole pairs indicated that the formation of defects such as a grain boundary was suppressed in the single crystalline nanorod photocatalyst than in the photocatalyst obtained by the solid-state reaction. The measurement revealed the suppression of recombination between photogenerated electrons and holes resulting in the high photocatalytic activities for water splitting and CO_2 reduction.

References

(1) Hawecker, J.; M. Lehn, J.; Ziessel, R. *J. Chem. Soc., Chem. Commun.* **1983**, 536.

(2) Hawecker, J.; M. Lehn, J.; Ziessel, R. *Helv. Chim. Acta.* **1986**, *69*, 1990.

(3) Takeda, H.; Koike, K.; Inoue, H.; Ishitani, O. *J. Am. Chem. Soc.* **2008**, *130*, 2023.

(4) Takeda, H.; Ishitani, O. *Coord. Chem. Rev.* **2010**, *254*, 346.

(5) Yui, T.; Tamaki, Y.; Sekizawa, K.; Ishitani, O. in *photocatalysis*, *Top. Curr. Chem.*, ed. C. A. Bignozzi, Springer, 2011, vol. 303, pp. 151-184.

(6) Tamaki, Y.; Watanabe, K.; Koike, K.; Inoue, H.; Morimoto, T.; Ishitani, O. *Faraday Discuss.*, **2012**, *155*, 115.

(7) M. Aliwi, S.; F. Al-Jubori, K. *Sol. Energy Mater.* **1989**, *18*, 223.

(8) Kanemoto, M.; Ishihara, K.; Wada, Y.; Sakata, T.; Mori, H.; Yanagida, S. *Chem. Lett.* **1992**, 835.

(9) Koči, K.; Obalova, L.; Lacny, Z. *Chem. Pap.* **2008**, *62*, 1.

(10) N. Habisreutinger, S.; Schmidt-Mende, L.; K. Stolarczyk, J. *Angew. Chem. Int. Ed*. **2013**, *52*, 7372.

(11) Tahir, M.; S. Amin, N. *Energy Convers. Manage.* **2013**, *76*, 194.

(12) Navalon, S.; Dhakshinamoorthy, A.; Alvaro, M.; Garcia, H. *ChemSusChem* **2013**, *6*, 562.

(13) Mao, J.; Li, K.; Peng, T. *Catal. Sci. Technol.* **2013**, *3*, 2481.

(14) Sayama, K.; Arakawa, H. *J. Phys. Chem.* **1993**, *97*, 531.

(15) Iizuka, K.; Wato, T.; Miseki, Y.; Saito, K.; Kudo, A. *J. Am. Chem. Soc.* **2011**, *133*, 20863.

(16) Teramura, K.; Wang, Z.; Hosokawa, S.; Sakata, Y.; Tanaka, T. *Chem. Eur. J.* **2014**, *20*, 9906.

(17) Kudo, A.; Miseki, Y. *Chem. Soc. Rev.* **2009**, *38*, 253.

(18) Kato, H.; Kudo, A. *Catal. Today* **2003**, *78*, 561.

(19) Kudo, A.; Okutomi, H.; Kato, H. *Chem. Lett.* **2000**, 1212.

(20) Miseki, Y.; Kato, H.; Kudo, A. *Energy Environ. Sci.* **2009**, *2*, 306.

(21) Nelson, D.; Scheetz, B.; Abate, C. *The International Centre for Diffraction Data*, # 40-351.

(22) Kato, H.; Kudo, A. *J. Phys. Chem. B* **2001**, *105*, 4285.

(23) P. Seah, M. *Surf. Interface Anal.* **1989**, *14*, 488.

(24) Iwase, A.; Kato, H.; Kudo, A. *Appl. Catal.B: Environ.* **2013**, *89*, 136.

(25) Negishi, Y.; Mizuno, M.; Hirayama, M.; Omatoi, M.; Takayama, T.; Iwase, A.; Kudo, A. *Nanoscale* **2013**, *5*, 7188.

(26) Hori, Y.; Kikuchi, K.; Suzuki, S. *Chem. Lett.* **1985**, 1695.

(27) Hori, Y.; Wakebe, H.; Tsukamoto, T.; Koga, O. *Electrochim. Acta* **1994**, *39*, 1833.

(28) Hatsukade, T.; P. Kuhl, K.; R. Cave, E.; N Abram, D.; F. Jaramillo, T. *Phys. Chem. Chem. Phys.* **2014**, *16*, 13814.

(29) Ishitani, O.; Inoue, C.; Suzuki, Y.; Ibusuki, T. *J. Photochem. Photobiol. A: Chem.* **1993**, *72*, 269.

(30) Domen, K.; Kudo, A.; Onishi, T.; Kosugi, N.; Kuroda, H. *J. Phys. Chem.* **1986**, *90*, 292.

(31) Jia, Q.; Miseki, Y.; Saito, K.; Kobayashi, H.; Kudo, A. *Bull. Chem. Soc. Jpn.* **2010**, *83*, 1275.

(32) Kato, H.; Asakura, K.; Kudo, A. *J. Am. Chem. Soc.* **2003**, *125*, 3082.

(33) Matsubara, K.; Tatsuma, T. *Adv. Mater.* **2007**, *19*, 2802.

(34) Kakihana, M.; Domen, K. *MRS Bull.* **2000**, *25*, 27.

(35) Miseki, Y.; Kudo, A. *ChemSusChem.* **2011**, *4*, 245.

(36) Yoshioka, K.; Petrykin, V.; Kakihana, M.; Kato, H.; Kudo, A. *J. Catal.* **2005**, *232*, 102.

(37) Kudo, A.; Sakata, T. *J. Phys. Chem.* **1995**, *99*, 15963.

(38) Kudo, A.; Kaneko, E. *Chem. Commun.* **1997**, 349.

(39) Kudo, A. *Chem. Mater.* **1997**, *9*, 664.

(40) Zhang, W.; Kumada, N.; Takei, T.; Yonesaki, Y.; Kinomura, N. *Mater. Res. Bull.* **2007**, *42*, 844.

(41) Brik, F.; Enjalbert, R.; Roucau, C.; Galy, J. *J. Solid State Chem.* **1996**, *122*, 7.

(42) Nakanishi, H.; Nakamura, A.; Wato, T.; Iwase, A.; Kudo, A. *Abstract of the CATSJ Meeting* **2012**, Vol. 110, p 547.

Chapter 3

Preparation of nanorod-shaped $K_3Ta_3Si_2O_{13}$ photocatalyst with tungsten bronze-like structure for water splitting

3-1. Introduction

Water splitting using semiconductor photocatalysts has extensively been studied as a candidate of clean hydrogen production. Water splitting under visible light irradiation has been achieved using single particulate photocatalysts of GaN-ZnO,[1] $ZnGeN_2$-ZnO,[2] TaON,[3] and Rh and Sb codoped-$SrTiO_3$.[4] However, the efficiencies are not satisfying. On the other hand, various metal oxide photocatalysts with wide band gaps have been reported.[5] $NaTaO_3$:La[6] and Zn-doped Ga_2O_3[7] give high quantum yields for water splitting. These wide band gap photocatalysts are suitable samples for examining the mechanism of photocatalytic reactions as well as TiO_2. For example, dynamics of photogenerated carriers[8] and relationship among crystal structure, physical property, and photocatalytic activity[9] have been studied using $NaTaO_3$ photocatalysts. Therefore, it is important to develop and improve various types of photocatalyst materials even with wide band gaps, because those photocatalysts can be employed for the basic research of the photocatalytic water splitting into H_2 and O_2.

To prepare single crystal-like photocatalyst particles is advantageous to obtaining high photocatalytic performances because recombination between photogenerated electrons and holes is suppressed in such particles. Therefore, the preparation of highly crystalline photocatalysts with shapes reflecting the crystal structures is a potential strategy to improve the activity. Polymerized complex[10-11] and flux[12] methods easily give such photocatalyst particles. Nanorod-shaped $K_2LaNb_5O_{15}$ photocatalyst powder with tungsten bronze structure is obtained by the polymerized complex method.[11] $SrTiO_3$ photocatalyst with a specific crystal face and high crystallinity is also prepared from a precursor obtained by a polymerized complex method and by subsequent flux treatment. This $SrTiO_3$ photocatalyst shows high activity for water splitting as well as $NaTaO_3$:La photocatalyst.[13] Therefore, it is interesting to prepare highly crystalline photocatalyst particles with shapes reflecting the crystal structures by polymerized complex and flux methods and examine the photocatalytic activity.

$K_3Ta_3Si_2O_{13}$ possesses tungsten bronze-like structure in which three chains of corner-shared TaO_6 octahedra form pillared structure along the c axis and the pillars are connected with SiO_4

tetrahedral units as shown in Figure 3-1.[14] The bond angles of O-Ta-O are 178° and 167°. Although $Ba_3Ta_6Si_4O_{26}$ has the similar crystal structure to $K_3Ta_3Si_2O_{13}$, the bond angles of TaO_6 chains are 163° and 141° that are quite distorted as shown in Figure 3-2.[14] Although the $K_3Ta_3Si_2O_{13}$ and $Ba_3Ta_6Si_4O_{26}$ prepared by a solid-state reaction and an amorphous metal complex method show photocatalytic activities for water splitting, the activities are not high.[15-16] These photocatalyst powders have featureless shapes. Therefore, it is expected that the photocatalytic activities are improved by using highly crystalline particles with the shape of the pillared crystal structure. Moreover, it is interesting to compare the photocatalytic activities from the viewpoints of the distortion of the one-dimensional pillared structure and the morphologies of the particles.

In the present study, highly crystalline $K_3Ta_3Si_2O_{13}$ and $Ba_3Ta_6Si_4O_{26}$ with specific morphologies were prepared by a flux method using KCl. The relationship among the crystal structure, morphology, and the photocatalytic activity was discussed.

3-2. Experimental

Preparation of photocatalysts

$K_3Ta_3Si_2O_{13}$ and $Ba_3Ta_6Si_4O_{26}$ powders were prepared by a solid-state reaction and a flux method. These samples are denoted as SSR-$K_3Ta_3Si_2O_{13}$, Flux-$K_3Ta_3Si_2O_{13}$, SSR-$Ba_3Ta_6Si_4O_{26}$, and Flux-$Ba_3Ta_6Si_4O_{26}$, respectively. SSR-$K_3Ta_3Si_2O_{13}$ was prepared by the same condition according to a previous report.[15] Starting materials for SSR-$Ba_3Ta_6Si_4O_{26}$ were $BaCO_3$ (Kanto Chemical; 99%), Ta_2O_5 (Rare Metallic; 99.99%), and SiO_2 (Kanto Chemical, 50 mol%excess). The mixture of starting materials was calcined at 1423 K for 10 h in air using a platinum crucible. Flux-$K_3Ta_3Si_2O_{13}$ and Flux-$Ba_3Ta_6Si_4O_{26}$ were prepared using KCl (Kanto Chemical; 99.5%, melting point; 1043 K) as the flux agent and an alumina crucible. Single phases of $K_3Ta_3Si_2O_{13}$ and $Ba_3Ta_6Si_4O_{26}$ were obtained at 1423 K of the preparation temperature by the flux method. The obtained powders were washed out with water to remove the KCl flux. NiO cocatalyst was loaded by an impregnation method (573 K for 1 h in air) from an aqueous $Ni(NO_3)_2$ solution.

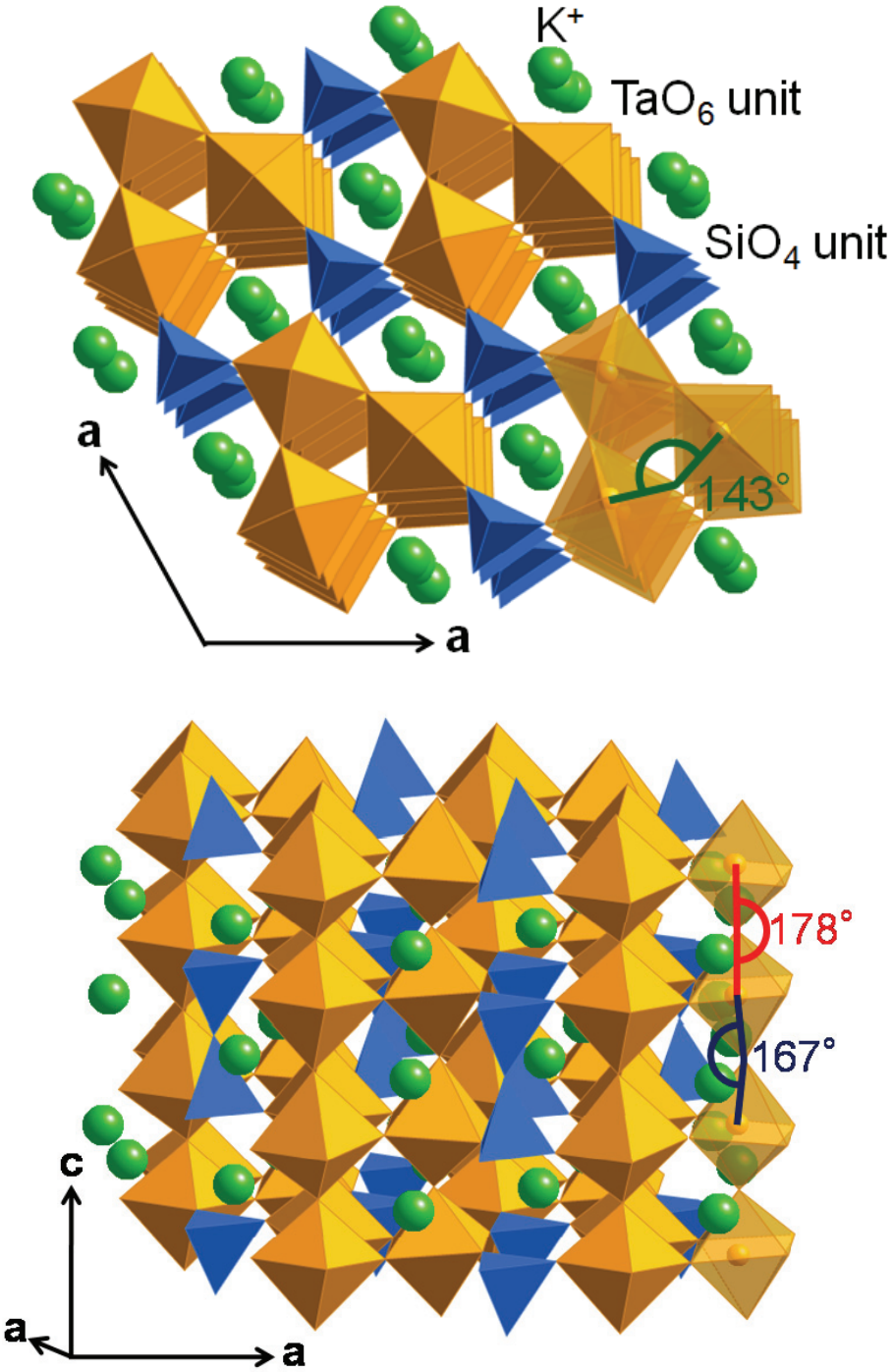

Figure 3-1. Crystal structure of $K_3Ta_3Si_2O_{13}$.[14]

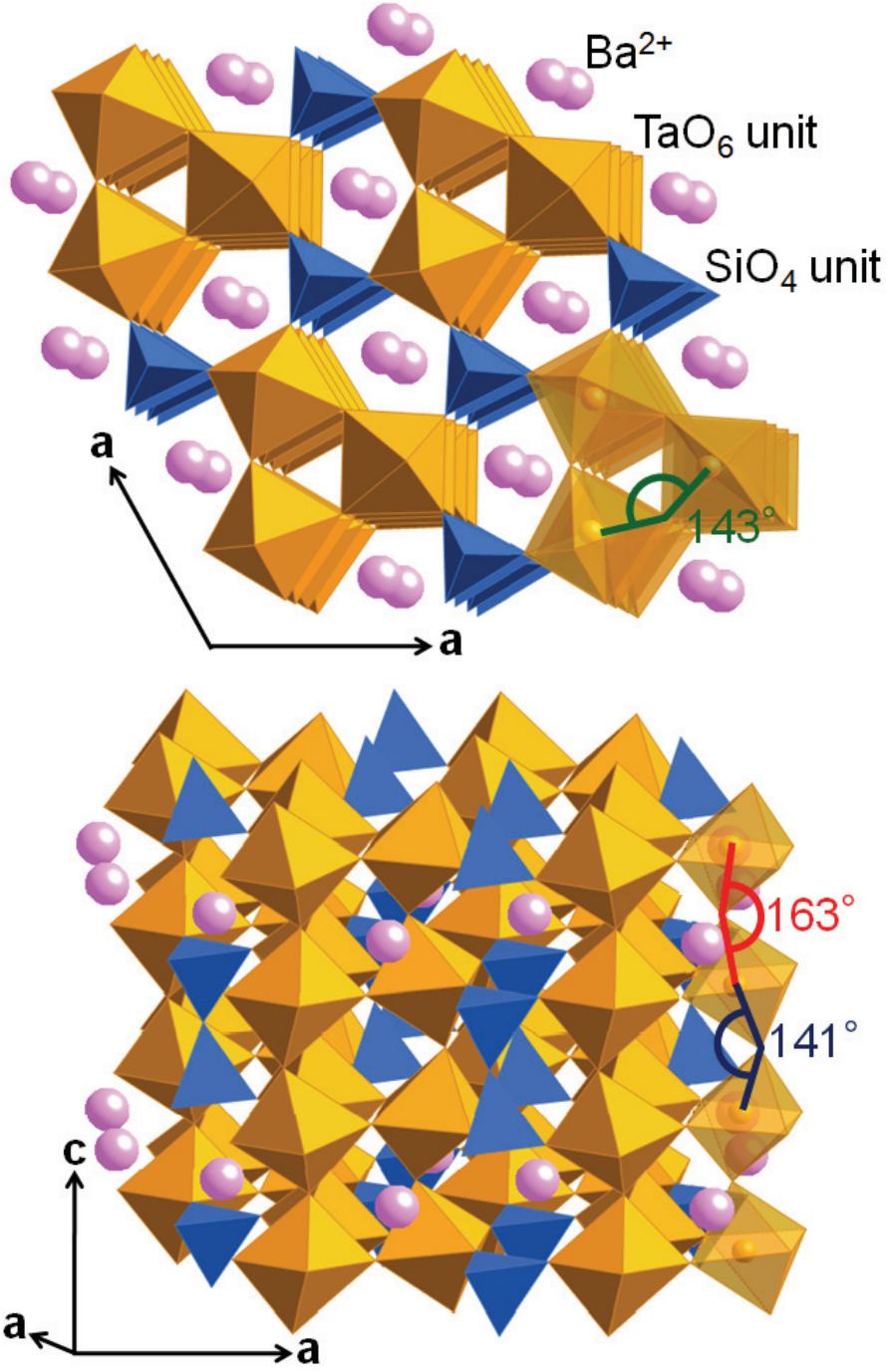

Figure 3-2. Crystal structure of $Ba_3Ta_6Si_4O_{26}$.[14]

Characterization of photocatalysts

Crystal phases of obtained powders were confirmed by X-ray diffraction using Cu Kα radiation (Rigaku; Miniflex). Diffuse reflection spectra of these powders were obtained by using a UV-vis-NIR spectrometer and converted to absorbance from the reflection by using Kubelka-Munk function. The morphology of obtained particles was observed by using a scanning electron microscope (JEOL; JSM-6700F).

Photocatalytic water splitting

Photocatalytic water splitting was conducted using an Ar flow system and an inner irradiation cell made of quartz with a 400 W high-pressure mercury lamp. 0.5 g of photocatalyst powder was dispersed in 350 mL of pure water by using a magnetic stirrer. Ar gas (99.99%) was continuously bubbled into the suspension at about 30 mL min^{-1} of a flow rate during the photocatalytic reaction. Gaseous products of H_2 and O_2 were determined by using a gas chromatograph (Shimadzu: GC-8A with Molecular Sieve 5A, TCD and Ar carrier). The apparent quantum yield for water splitting was measured using a gas-closed circulation system. 0.5 g of photocatalyst powder was dispersed in 350 mL of pure water in a top-irradiation cell made of quartz. A 300 W Xe-arc lamp with a band-pass filter was employed as a monochromatic light source at 254 nm.

3-3. Results and discussion

3-3-1. Characterization of nanorod-shaped $K_3Ta_3Si_2O_{13}$ and block-shaped $Ba_3Ta_6Si_4O_{26}$ prepared by a solid-state reaction and a flux method

Figure 3-3 shows XRD patterns of $K_3Ta_3Si_2O_{13}$ and $Ba_3Ta_6Si_4O_{26}$ prepared by a solid-state reaction and a flux method. SSR-$K_3Ta_3Si_2O_{13}$ was obtained as a single phase by preparation at 1573 K (Figure 3-3a), whereas preparation at 1423 K gave some impurities (Figure 3-3b) as reported.[15] In contrast, the single phase was obtained by the flux method using KCl even at 1423 K (Figure 3-3c).

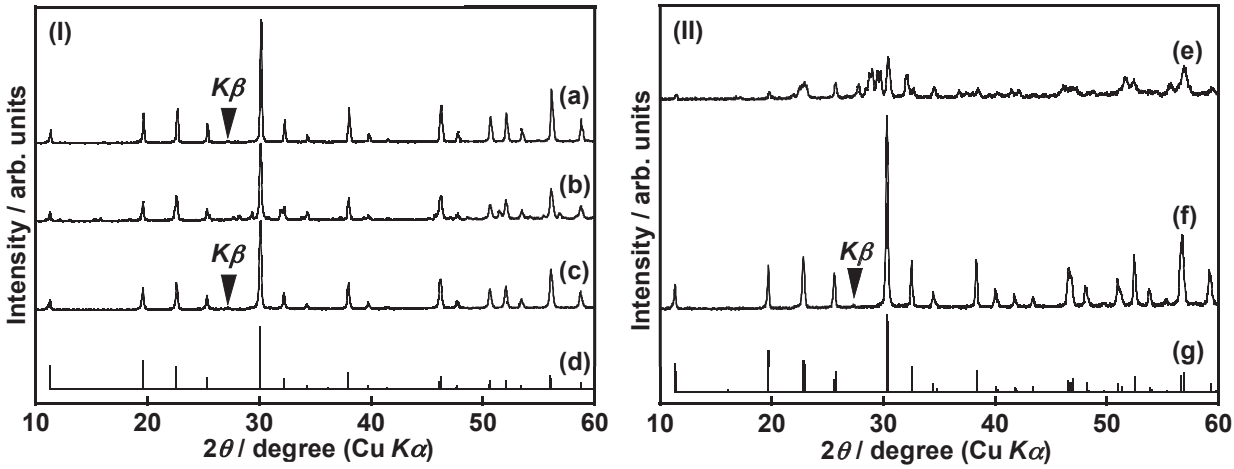

Figure 3-3. X-ray diffraction patterns of (I) $K_3Ta_3Si_2O_{13}$ and (II) $Ba_3Ta_6Si_4O_{26}$ prepared by a solid-state reaction and a flux method at several temperatures for 10 h. $K_3Ta_3Si_2O_{13}$ prepared by a solid-state reaction at (a) 1573 K, (b) 1423 K, (c) a flux method at 1423 K, and (d) PDF: 1-72-557. $Ba_3Ta_6Si_4O_{26}$ prepared by (e) a solid-state reaction at 1423 K, (f) a flux method at 1423 K, and (g) PDF: 1-72-555.

Although the solid-state reaction gave some impurities for the preparation of $Ba_3Ta_6Si_4O_{26}$ as reported,[16] the single phase was obtained by the flux method (Figure 3-3e, f). Diffuse reflection spectra indicated that band gaps of SSR-$K_3Ta_3Si_2O_{13}$, Flux-$K_3Ta_3Si_2O_{13}$, and Flux-$Ba_3Ta_6Si_4O_{26}$ were 4.1, 4.2, and 4.3 eV, respectively as shown in Figure 3-4.

Figure 3-5 shows SEM images of $K_3Ta_3Si_2O_{13}$ and $Ba_3Ta_6Si_4O_{26}$ prepared by a solid-state reaction and a flux method. SSR-$K_3Ta_3Si_2O_{13}$ was sintered particles with a featureless shape. In contrast, most of Flux-$K_3Ta_3Si_2O_{13}$ particles were nanorod with 100−150 nm of width and 300−2000 nm of length. The formation of nanorod by the flux method is also observed for $KSr_2Ta_5O_{15}$ photocatalyst that possesses the similar structure to $K_3Ta_3Si_2O_{13}$.[12] Although $Ba_3Ta_6Si_4O_{26}$ was prepared by an amorphous metal complex method using a peroxo complex, the obtained particles were sintered and had featureless shape,[16] Flux-$Ba_3Ta_6Si_4O_{26}$ possessed not a nanorod shape but a block shape with high crystallinity. The difference in morphology between Flux-$K_3Ta_3Si_2O_{13}$ and Flux-$Ba_3Ta_6Si_4O_{26}$ particles is due to the degree of the distortion of pillared structure. The bond angles of O-Ta-O chains in $K_3Ta_3Si_2O_{13}$ are more liner than those of $Ba_3Ta_6Si_4O_{26}$ as shown in Figures 3-1 and 3-2. Crystal growth along the c axis seems easy for $K_3Ta_3Si_2O_{13}$ resulting in the growth of nanorod. In contrast, crystal growth along the c axis seems to be suppressed for $Ba_3Ta_6Si_4O_{26}$ with zigzag chains of TaO_6 units giving the thick block shape.

3-3-2. Photocatalytic water splitting over nanorod-shaped $K_3Ta_3Si_2O_{13}$ and block-shaped $Ba_3Ta_6Si_4O_{26}$ prepared by a solid-state reaction and a flux method

Table 1 shows photocatalytic activities for water splitting over $K_3Ta_3Si_2O_{13}$ and $Ba_3Ta_6Si_4O_{26}$ prepared by a solid-state reaction and a flux method. SSR-$K_3Ta_3Si_2O_{13}$ showed the activity even without loading of any cocatalysts as reported.[15] SSR-$K_3Ta_3Si_2O_{13}$ showed slightly higher activity than Flux-$K_3Ta_3Si_2O_{13}$ without cocatalysts. In this case, a surface reaction for H_2 evolution would be a rate-determining step. Therefore, the bulk property did not significantly affect the photocatalytic activity. So, the large surface area of SSR-$K_3Ta_3Si_2O_{13}$ would be effective for the

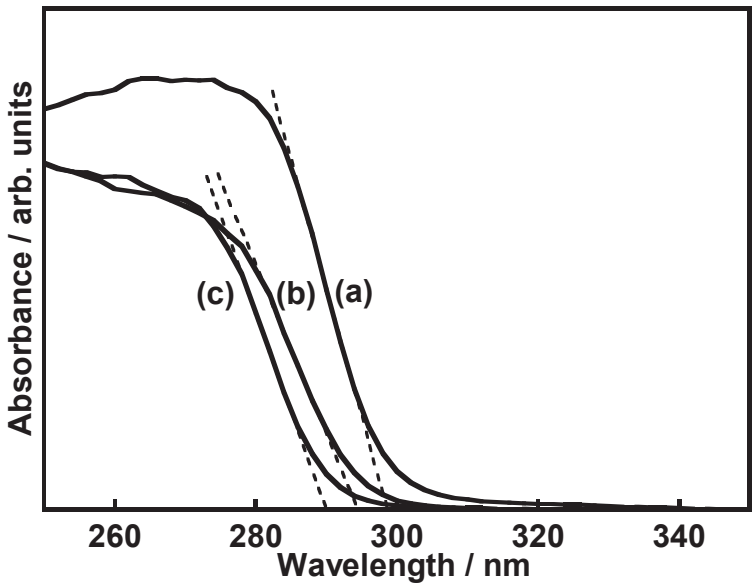

Figure 3-4. Diffuse reflectance spectra of $K_3Ta_3Si_2O_{13}$ prepared by (a) a solid-state reaction (1573 K for 10 h) and (b) a flux method (1423 K for 10 h), and (c) $Ba_3Ta_6Si_4O_{26}$ prepared by a flux method (1423 K for 10 h).

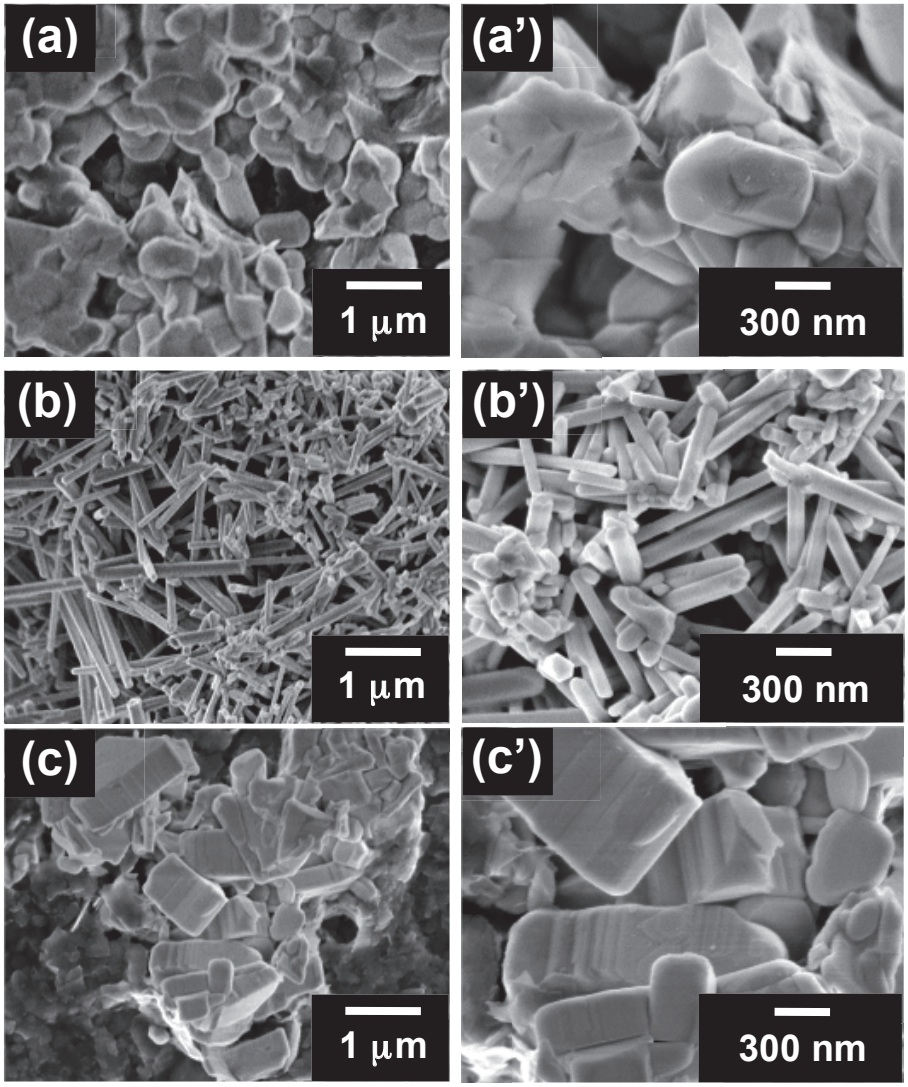

Figure 3-5. SEM images of $K_3Ta_3Si_2O_{13}$ prepared by (a and a') a solid-state reaction at 1573 K and (b and b') a flux method at 1423 K for 10 h, and (c and c') $Ba_3Ta_6Si_4O_{26}$ prepared by a flux method at 1423 K for 10 h

Table 1. Photocatalytic water splitting over metal oxide materials with tungsten bronze-like structure prepared by a solid-state reaction (SSR) and a flux method (Flux)

Photocatalyst	Preparation Method	Band Gap / eV	Surface Area / m^2 g^{-1}	Cocatalyst (wt%)	Activity / μmol h^{-1}		AQY(%) at 254 nm
					H_2	O_2	
$K_3Ta_3Si_2O_{13}$	SSR	4.1	6.1	None	100	47	–
$K_3Ta_3Si_2O_{13}$	SSR	4.1	–	NiO (0.2)	309	132	1.7
$K_3Ta_3Si_2O_{13}$	SSR	4.1	–	NiO (1.3)	214	94	–
$K_3Ta_3Si_2O_{13}$	Flux	4.2	4.4	None	78	36	–
$K_3Ta_3Si_2O_{13}$	Flux	4.2	–	NiO (0.2)	773	406	2.4
$K_3Ta_3Si_2O_{13}$	Flux	4.2	–	NiO (1.3)	458	235	–
$Ba_3Ta_6Si_4O_{26}$	Flux	4.3	1.1	None	17	5	–
$Ba_3Ta_6Si_4O_{26}$	Flux	4.3	–	NiO (0.2)	134	68	0.2
$Ba_3Ta_6Si_4O_{26}$	Flux	4.3	–	NiO (1.3)	95	3	–

Catalyst: 0.5 g,, reactant solution: pure water (350 mL), system: an Ar gas flow system using an inner irradiation cell made of quartz, light source: a 400 W high-pressure mercury lamp.

high activity. The activity was much improved by loading of a NiO cocatalyst to introduce the surface active site for H_2 evolution. In contrast to the pristine photocatalysts, the activity of NiO/Flux-$K_3Ta_3Si_2O_{13}$ was higher than that of NiO/SSR-$K_3Ta_3Si_2O_{13}$, because the bulk property mainly affected the photocatalytic activity rather than the surface area in the presence of an excellent cocatalyst enhancing surface reactions. Apparent quantum yields of NiO/SSR-$K_3Ta_3Si_2O_{13}$ and NiO/Flux-$K_3Ta_3Si_2O_{13}$ were 1.7% and 2.4% at 254 nm, respectively. H_2 and O_2 evolved in a stoichiometric amount even under the week UV irradiation using a Xe lamp and a band-pass filter. The major reason for the higher activity of NiO/Flux-$K_3Ta_3Si_2O_{13}$ than NiO/SSR-$K_3Ta_3Si_2O_{13}$ is that the amount of defect such as grain boundary in single crystal-like nanorods of Flux-$K_3Ta_3Si_2O_{13}$ is smaller than that in featureless particles of SSR-$K_3Ta_3Si_2O_{13}$ as observed by SEM, because the defects work as recombination centers for photogenerated electrons and holes. The anisotropic nanorod structure would also contribute to enhancement of charge separation. Flux-$Ba_3Ta_6Si_4O_{26}$ also showed the photocatalytic activity for water splitting without cocatalysts as reported.[16] Although the photocatalytic activity was improved with a NiO cocatalyst, it was lower than that of $K_3Ta_3Si_2O_{13}$. The reason why the activity of Flux-$Ba_3Ta_6Si_4O_{26}$ was lower than NiO/Flux-$K_3Ta_3Si_2O_{13}$ is due to the degree of distortion of TaO_6 chains. Excited energy or photogenerated electron-hole pairs will mainly migrate along the c-axis of the pillared structure, because the pillars consisting of TaO_6 chains are separated from each other by SiO_4 units in the direction of an a-axis. As the bond angle of O-Ta-O in corner-shared TaO_6 along the c-axis is close to 180^o, migration of the excited energy or photogenerated electron-hole pairs becomes easy as observed in perovskite structure.[9] Therefore, mobility of excited energy or photogenerated electron-hole pairs in $Ba_3Ta_6Si_4O_{26}$ is more localized than that of $K_3Ta_3Si_2O_{13}$. It results in the decrease in excited energy or photogenerated electron-hole pairs that can reach the surface and the decrease in photocatalytic activity.

Figure 3-6 shows photocatalytic water splitting over NiO(0.2 wt%)/Flux-$K_3Ta_3Si_2O_{13}$. H_2 and O_2 steadily evolved in a stoichiometric amount. The turnover number of electrons and holes consumed for H_2 and O_2 evolutions to molar quantity of Flux-$K_3Ta_3Si_2O_{13}$ was 5.7 indicating that

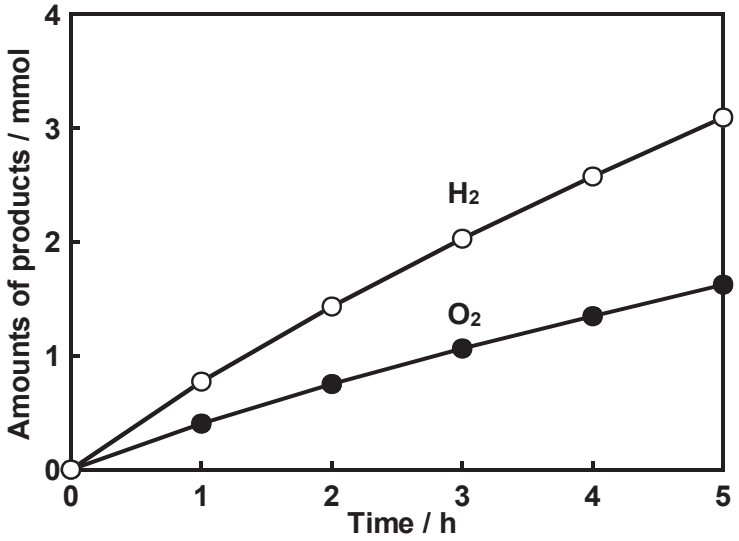

Figure 3-6. Photocatalytic water splitting over NiO(0.2 wt%)/$K_3Ta_3Si_2O_{13}$ prepared by a flux method.

the reaction proceeded photocatalytically. Color of the NiO cocatalyst turned pail purple from gray during photocatalytic water splitting, indicating the activated NiO cocatalyst as observed for many metal oxide photocatalysts with wide band gaps.[6, 9] Thus, the NiO cocatalyst was also activated on the Flux-$K_3Ta_3Si_2O_{13}$ photocatalyst to show high activity.

3-4. Conclusions

It was confirmed that the flux method was effective for preparation of high crystalline particles with the morphology reflecting the crystal structure for materials with tungsten bronze-like structure. The effects of distortion of the TaO_6 chains on the crystal growth and the photocatalytic activity for $K_3Ta_3Si_2O_{13}$ and $Ba_3Ta_6Si_4O_{26}$ with one-dimensional pillared structure were clarified by preparing the highly crystalline particles using the flux method.

References

(1) Maeda, K.; Teramura, K.; Lu, D.; Takata, T.; Saito, N.; Inoue, Y.; Domen, K. *Nature* **2006**, *440*, 295.

(2) Lee, Y.; Terashima, H.; Shimodaira, Y.; Teramura, K.; Hara, M.; Kobayashi, H.; Domen, K.; Yashima, M. *J. Phys. Chem. C* **2007**, *111*, 1042.

(3) Maeda, K.; Lu, D.; Domen, K. *Chem. Eur. J.* **2013**, *19*, 4986.

(4) Asai, R.; Nemoto, H.; Jia, Q.; Saito, K.; Iwase, A.; Kudo, A. *Chem. Commun.* **2014**, *50*, 2543.

(5) Kudo, A.; Miseki, Y. *Chem. Soc. Rev.* **2009**, *38*, 253, and references therein.

(6) Kato, H.; Asakura, K.; Kudo, A. *J. Am. Chem. Soc.* **2003**, *125*, 3082.

(7) Sakata, Y.; Matsuda, Y.; Nakagawa, T.; Yasunaga, R.; Imamura, H.; Teramura, K. *ChemSusChem* **2011**, *4*, 181.

(8) Yamakata, A.; Ishibashi, T.; Kato, H.; Kudo, A.; Onishi, H. *J. Phys. Chem. B* **2003**, *107*, 14383.

(9) Kato, H.; Kudo, A. *J. Phys. Chem. B* **2001**, *105*, 4285.

(10) Kakihana, M.; Domen, K. *MRS Bull.* **2000**, *25*, 27.

(11) Miseki, Y.; Kudo, A. *ChemSusChem* **2011**, *4*, 245.

(12) Wang, P.; Schwertmann, L.; Marschall, R.; Wark, M. *J. Mater. Chem. A* **2014**, *2*, 8815.

(13) Kato, H.; Kobayashi, M.; Harab, M.; Kakihana, M. *Catal. Sci. Technol.* **2013**, *3*, 1733.

(14) Choisnet, J.; Nguyen, N.; Groult, D.; Raveau, B. *Mat. Res. Bull.* **1976**, *11*, 887.

(15) Kudo, A.; Kato, H. *Chem. Lett.* **1997**, 867.

(16) Yanagisawa, R.; Petrykin, V.; Kakihana, M. *J. Jpn. Soc. Powder Powder Metallurgy* **2010**, *57*, 701.

Chapter 4

Development of Ag/ZnS/$Cu_{0.8}Ag_{0.2}GaS_2$ photocathode for CO_2 reduction using water as an electron donor under visible light irradiation

4-1. Introduction

$BaLa_4Ti_4O_{15}$ and Zn-doped Ga_2O_3 with wide band gaps reduce CO_2 to CO by loading Ag cocatalyst on the surface.[1, 2] In the chapter 2, $KCaSrTa_5O_{15}$ has arisen as a new photocatalyst for water splitting and CO_2 reduction. The important point of the CO_2 reduction using these photocatalysts is that H_2, CO and O_2 evolve in the stoichiometric amounts. However, The wide band gap photocatalysts cannot be used in the industry process because it doesn't respond to visible light occupying a lot of part of the sunlight.

Many metal sulfide photocatalysts which have the valence band formed by S3p orbitals with negative level compered with O2p orbitals respond to visible light. Although CdS photocatalyst showed activities for hydrogen evolution and CO_2 reduction under visible light irradiation, sacrificial reagent is indispensable. In contrast, Cu_2ZnSnS_4 and with p-type semiconductor character shows activity for photoelectrochemical hydrogen evolution with external bias under visible light irradiation.[4] The photoelectrochemical reaction can be called uphill reaction if the external bias is smaller than the theoretical bias to split water (1.23 V) between working and counter electrodes. Therefore, development of metal sulfide photocathodes showing activity for CO_2 reduction has attracted. $Cu_{0.8}Ag_{0.2}GaS_2$ photocatalyst with chalcopyrite structure has a p-type semiconductor character.[5, 6] In the present study, photoelectrochemical CO_2 reduction under visible light irradiation over $Cu_{0.8}Ag_{0.2}GaS_2$ photocathode was studied. Moreover, The improving of activity of $Cu_{0.8}Ag_{0.2}GaS_2$ photocathode was conducted by comodifying ZnS thin film and various metal cocatalysts.

4-2. Experimental

$Cu_{0.8}Ag_{0.2}GaS_2$ photocatalyst was prepared by a solid-state reaction. The starting materials were Cu_2S , Ag_2S and Ga_2S_3. The mixture was sealed in a quartz ampoule tube *in vacuo*, and heat-treated at 1073 K for 10 h. The excess amount of gallium (10%) was added to the mixture. The photocatalyst powder was dispersed in ethanol, and casted on FTO electrode. After drying, the

electrode was annealed at 773 K for 2 h in N_2 atmosphere to prepare photoelectrode. The photoelectrode was modified with ZnS thin film by a chemical bath deposition method according to previous report.[7] The starting materials were $ZnSO_4 \bullet 4H_2O$ (Wako Pure Chemical; 99.5%), thiourea (98.0 %), citric acid (98.0%) and 25% ammonia solution (Wako Pure Chemical). The mixed solution of 0.03 mol L^{-1} of $ZnSO_{4\ aq.}$, 0.06 mol L^{-1} of thiourea $_{aq.}$ and 0.08 mol L^{-1} of citric acid $_{aq.}$ was heated to 353 K. The photoelectrode was dipped for 10 minute to modify with ZnS thin film on the surface and dried at room temperature after adding 10 vol% of ammonia solution(25%) into the mixture solution. The ZnS thin film-modified photoelectrode was annealed at 773 K for 2 h in N_2 atmosphere. Nonannealed and annealed the photoelectrodes modified with ZnS thin film were denoted as TF-ZnS(NA)/$Cu_{0.8}Ag_{0.2}GaS_2$ and TF-ZnS(A)/$Cu_{0.8}Ag_{0.2}GaS_2$, respectively. As comparison of the TF-ZnS(A)/$Cu_{0.8}Ag_{0.2}GaS_2$ photoelectrode, the $Cu_{0.8}Ag_{0.2}GaS_2$ photoelectrode modified with ZnS particles was prepared by casting the ZnS suspension in ethanol onto the photoelectrode and drying at room temperature and subsequent annealing at 773 K for 2 h in N_2 atmosphere (denoted as P-ZnS(A)/$Cu_{0.8}Ag_{0.2}GaS_2$).

Cocatalysts were loaded according to follows. The aqueous solution dissolved a metallic salt was casted on photoelectrode. The photoelectrode annealed at 773 K for 2 h in N_2 atmosphere after drying up the solution. The method was conducted after that the photoelectrode was dipped in a mixture solution of water and acetone (the ratio of 1:1 as a volume), if necessary. $AgNO_3$, $HAuCl_4$, H_2PrCl_6, $RuCl_3$ and $RhCl_3$ were employed as starting materials for cocatalysts.

Photoelectrochemical properties were evaluated using a potentiostat (Hokuto Denko; HZ-3000) and an H-type cell divided into working and counter electrode cell by Nafion (Dupont). Pt plate (1 cm^2) and a saturated Ag/AgCl electrode (DKK-TOA) were used as the counter electrode and reference electrode, respectively. 0.1 mol L^{-1} of $K_2SO_{4\ aq.}$ with phosphate buffer (0.025 mol L^{-1} each of $KH_2PO_{4\ aq.}$ and $Na_2HPO_{4\ aq.}$) and 0.1 mol L^{-1} of $KHCO_{3\ aq.}$ were employed for electrolyte, respectively. The electrolyte in both cells was bubbled with N_2 or CO_2 before measurements. The light source was a 300 W Xe-arc lamp. The wavelength of the irradiation light was controlled by cutoff filters, an NIR-absorbing filter, and a plano-convex lens. The light source of pseudo-sun light

was a solar simulator. The gaseous products in H-type glass cell were determined by GC (Shimadzu; TCD, MS-5A, Ar carrier; FID with a methanizer, MS-13X, N_2 carrier). The isotope experiment was conducted by using $^{13}CO_2$ to confirm carbon source in CO_2 reduction. ^{13}CO as a reducing product was analyzed by GC-MS (Shimadzu; GCMS-QP2010 Plus, RESTEK; RT-Msieve 5A).

4-3. Results and discussion

4-3-1. Effect of ZnS modification on photocathodic property of $Cu_{0.8}Ag_{0.2}GaS_2$

Figure 4-1 shows photoresponse in current vs. potential curves for pristine $Cu_{0.8}Ag_{0.2}GaS_2$ and TF-ZnS(A)/$Cu_{0.8}Ag_{0.2}GaS_2$ electrodes under N_2 atmosphere. Cathodic photocurrent of the pristine $Cu_{0.8}Ag_{0.2}GaS_2$ electrode was drastically enhanced by modification of ZnS thin film. This would be due to that the charge separation of photogenerated electrons and holes in the $Cu_{0.8}Ag_{0.2}GaS_2$ photoelectrode was enhanced by the p-n junction formed by modification of ZnS thin film. The effect of ZnS modification on photocathodic property of $Cu_{0.8}Ag_{0.2}GaS_2$ electrode for CO_2 reduction was also evaluated by using TF-ZnS(NA)/$Cu_{0.8}Ag_{0.2}GaS_2$, TF-ZnS(A)/$Cu_{0.8}Ag_{0.2}GaS_2$, and P-ZnS(A)/$Cu_{0.8}Ag_{0.2}GaS_2$ electrodes as shown in Figure 4-2. The cathodic photocurrent of P-ZnS(A)/$Cu_{0.8}Ag_{0.2}GaS_2$ and TF-ZnS(NA)/$Cu_{0.8}Ag_{0.2}GaS_2$ electrodes were not enhanced compared with that of pristine $Cu_{0.8}Ag_{0.2}GaS_2$ electrode. In contrast, the cathodic photocurrent of TF-ZnS(A)/$Cu_{0.8}Ag_{0.2}GaS_2$ electrode was much larger than that of pristine $Cu_{0.8}Ag_{0.2}GaS_2$, P-ZnS(A)/$Cu_{0.8}Ag_{0.2}GaS_2$, and TF-(NA)/$Cu_{0.8}Ag_{0.2}GaS_2$ electrodes. The surface and bulk structure were analyzed by using a scanning electron microscope and X-ray photoelectron spectroscopy to clarify the effect of ZnS modification on photocathodic property of $Cu_{0.8}Ag_{0.2}GaS_2$ electrode.

Figure 4-3 shows SEM images of the top and the side of pristine $Cu_{0.8}Ag_{0.2}GaS_2$ and TF-ZnS(A)/$Cu_{0.8}Ag_{0.2}GaS_2$ photoelectrodes. Although ZnS thin film was not observed on the surface of TF-ZnS(A)/$Cu_{0.8}Ag_{0.2}GaS_2$, it was confirmed that both photoelectrodes were consisted of featureless particles.

Figure 4-4 shows the results of XPS measurement for Pristine and ZnS-modified

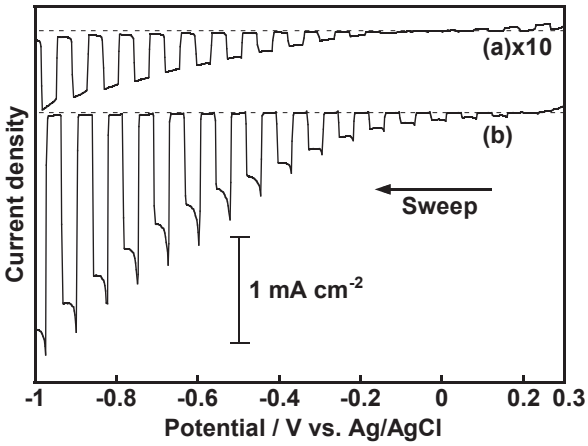

Figure 4-1. Current vs. potential curves for (a) pristine $Cu_{0.8}Ag_{0.2}GaS_2$ and (b) Thin-ZnS(A)/$Cu_{0.8}Ag_{0.2}GaS_2$ photoelectrodes under visible light irradiation and dark. Electrolyte: 0.1 mol L^{-1} of $K_2SO_{4\ aq.}$ with phosphate buffer (0.025 mol L^{-1} of $KH_2PO_{4\ aq.}$ and $Na_2HPO_{4\ aq.}$) with dissolved N_2 atmosphere, light source: a 300 W Xe-arc lamp with a cutoff filter (λ > 420 nm), sweep range: 0.3→−1 vs. Ag/AgCl, a counter electrode: Pt plate.

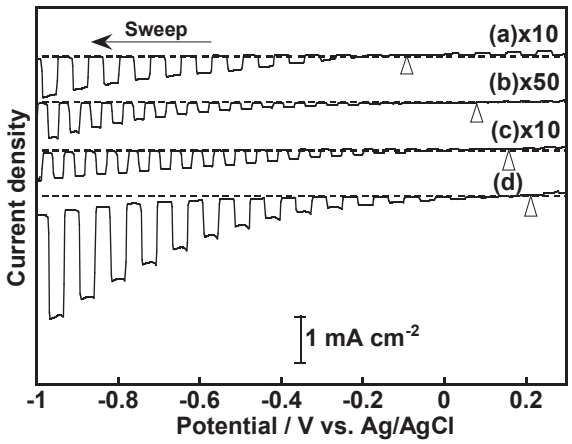

Figure 4-2. Current vs. potential curves for $Cu_{0.8}Ag_{0.2}GaS_2$ photoelectrode modified with ZnS by using different method. (a) pristine $Cu_{0.8}Ag_{0.2}GaS_2$, (b) P-ZnS(A)/$Cu_{0.8}Ag_{0.2}GaS_2$, (c) TF-ZnS(NA)/$Cu_{0.8}Ag_{0.2}GaS_2$, and TF-ZnS(A)/$Cu_{0.8}Ag_{0.2}GaS_2$ photoelectrodes. Modifying conditions: Particle-ZnS: a drop-cast method (773 K for 2 h in N_2), TF-ZnS: a chemical bath deposition (with or without annealing for 2 h in N_2 after the deposition). Open triangles indicate the on-set potential. Electrolyte: 0.1 mol L^{-1} of $KHCO_{3\ aq.}$ with dissolved CO_2 atmosphere, light source: a 300 W Xe-arc lamp with a cutoff filter (λ > 420 nm), sweep range: 0.3→−1 vs. Ag/AgCl, a counter electrode: Pt plate.

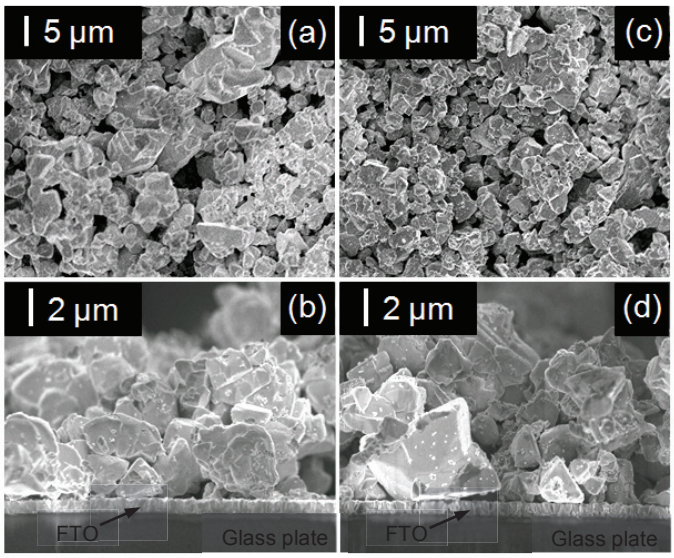

Figure 4-3. SEM images of top and side of (a and b) pristine-$Cu_{0.8}Ag_{0.2}GaS_2$ and (c and d) Thin-ZnS(A)/$Cu_{0.8}Ag_{0.2}GaS_2$ photocathodes.

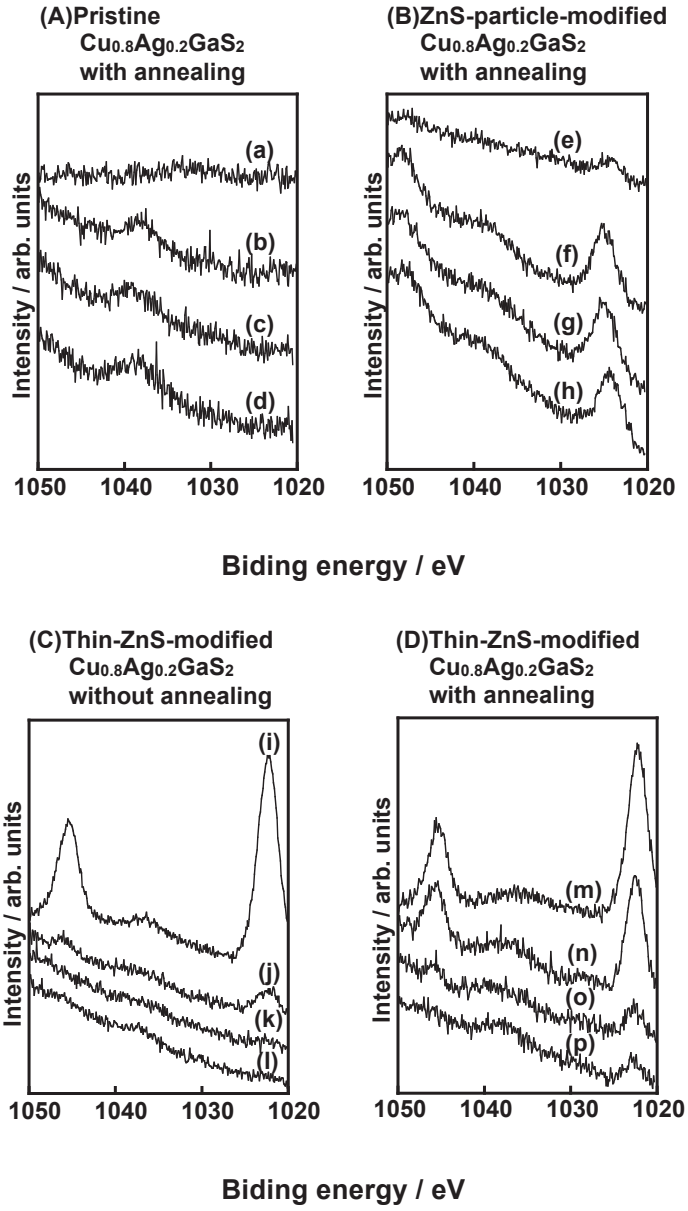

Figure 4-4. X-ray photoelectron spectra of (A) $Cu_{0.8}Ag_{0.2}GaS_2$, (B) P-ZnS(A)/$Cu_{0.8}Ag_{0.2}GaS_2$, (C) TF-ZnS(NA)/$Cu_{0.8}Ag_{0.2}GaS_2$ and (D) TF-ZnS(A)/$Cu_{0.8}Ag_{0.2}GaS_2$ photoelectrodes. Ar etching time: (a, e, i and m) 0 s, (b, f, j and n) 5 s, (c, g, k and o) 20 s, (d, h, l and p) 60 s.

$Cu_{0.8}Ag_{0.2}GaS_2$ photoelectrodes. All ZnS-modified $Cu_{0.8}Ag_{0.2}GaS_2$ photoelectrodes gave the Zn2p peak, while pristine $Cu_{0.8}Ag_{0.2}GaS_2$ photoelectrode did not give the Zn2p peak. Although the Zn2p peak before etching was smaller than that of after etching, P-ZnS(A)/$Cu_{0.8}Ag_{0.2}GaS_2$ photoelectrode gave the same intensities of the Zn2p peaks even after etching with the time at 5, 20, and 60 s. The Zn2p peaks of TF-ZnS(NA)/$Cu_{0.8}Ag_{0.2}GaS_2$ and TF-ZnS(A)/$Cu_{0.8}Ag_{0.2}GaS_2$ photoelectrodes were drastically decreased by etching, whereas the initial intensity of the peaks were much larger than the Zn2p peaks of P-ZnS(A)/$Cu_{0.8}Ag_{0.2}GaS_2$ photoelectrode. Especially, the Zn2p peak of TF-ZnS(NA)/$Cu_{0.8}Ag_{0.2}GaS_2$ photoelectrode disappeared by etching for 60 s of the time. In contrast, the Zn2p peak of TF-ZnS(A)/$Cu_{0.8}Ag_{0.2}GaS_2$ photoelectrode was observed even after etching for 60 s of the time.

The structures of Pristine and ZnS-modified $Cu_{0.8}Ag_{0.2}GaS_2$ photoelectrodes were proposed based on SEM and XPS measurements as shown in Figure 4-5. Pristine $Cu_{0.8}Ag_{0.2}GaS_2$ is accumulated on FTO substrate without any order (Figure 4-5(a)). The ZnS particles of P-ZnS(A)/$Cu_{0.8}Ag_{0.2}GaS_2$ accumulate on $Cu_{0.8}Ag_{0.2}GaS_2$ photoelectrode (Figure 4-5(b)). In contrast, ZnS thin film prepared by a chemical bath deposition without annealing coveres the surface of the $Cu_{0.8}Ag_{0.2}GaS_2$ photoelectrode judging from the results of XPS measurement (Figure 4-5(c)). The ZnS diffuses in the $Cu_{0.8}Ag_{0.2}GaS_2$ bulk with concentration gradient by annealing judging from the results of XPS measurement with Ar etching (Figure 4-5 (d)). Therefore, the TF-ZnS(A)/$Cu_{0.8}Ag_{0.2}GaS_2$ photoelectrode consists of three-layered structure with ZnS thin film at the surface, $(Cu_{0.8}Ag_{0.2}Ga)_{1-x}Zn_{2x}S_2$ solid-solution at the interlayer and $Cu_{0.8}Ag_{0.2}GaS_2$ in the bulk as sown in Figure 4-6(a). The structure gives p-n junction and continuous band gradient resulting in the formation of the band bending to the surface from the bulk as shown in Figure 4-6(b). The band gap of $(Cu_{0.8}Ag_{0.2}Ga)_{1-x}Zn_{2x}S_2$ solid-solution of a interlayer is probably almost the same as pristine $Cu_{0.8}Ag_{0.2}GaS_2$. The reason why the photocurrent was drastically enhanced by modification of ZnS thin film is that the band bending improved the charge separation of photogenerated carriers.

Figure 4-7 shows DRS and IPCE of a TF-ZnS(A)/$Cu_{0.8}Ag_{0.2}GaS_2$ electrode under N_2 atmosphere. The absorption edge of TF-ZnS(A)/$Cu_{0.8}Ag_{0.2}GaS_2$ photoelectrode was almost the

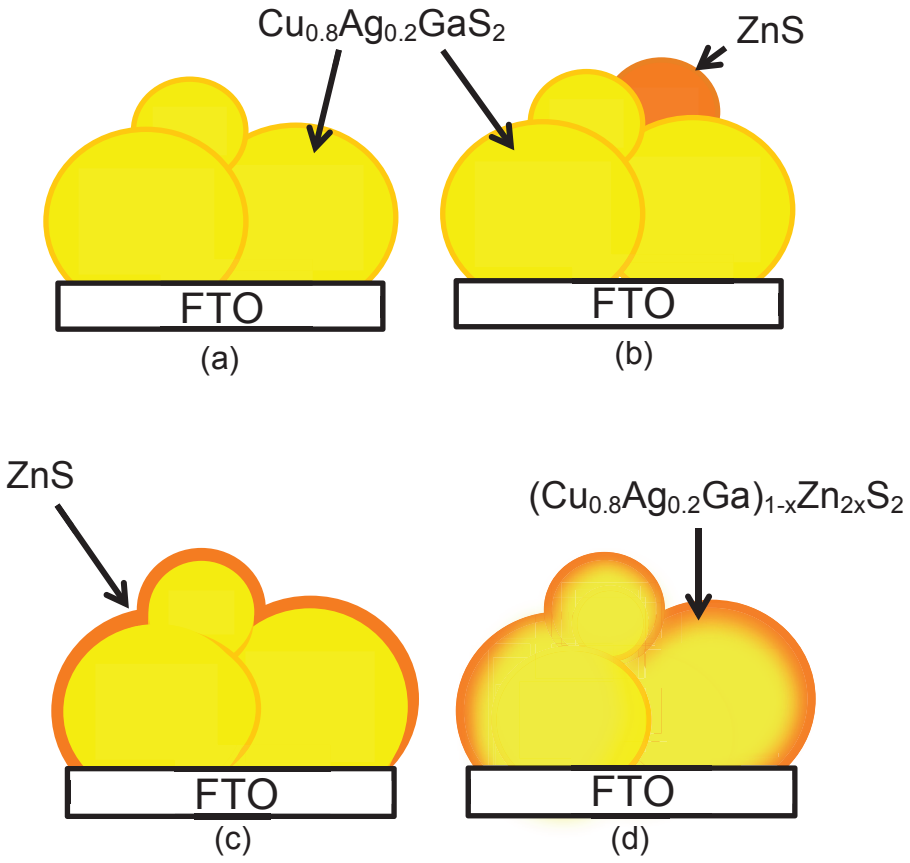

Figure 4-5. Proposed structures of (a) $Cu_{0.8}Ag_{0.2}GaS_2$, (b) P-ZnS(A)/$Cu_{0.8}Ag_{0.2}GaS_2$, (c) TF-ZnS(NA)/$Cu_{0.8}Ag_{0.2}GaS_2$ and (d) TF-ZnS(A)/$Cu_{0.8}Ag_{0.2}GaS_2$ photoelectrodes.

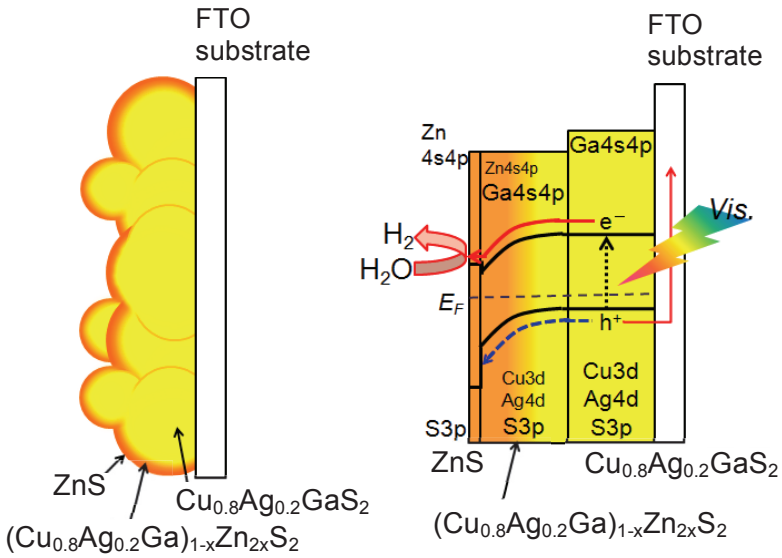

Figure 4-6. Proposed sedimentation and band structure of Thin-ZnS(A)/$Cu_{0.8}Ag_{0.2}GaS_2$ photoelectrodes.

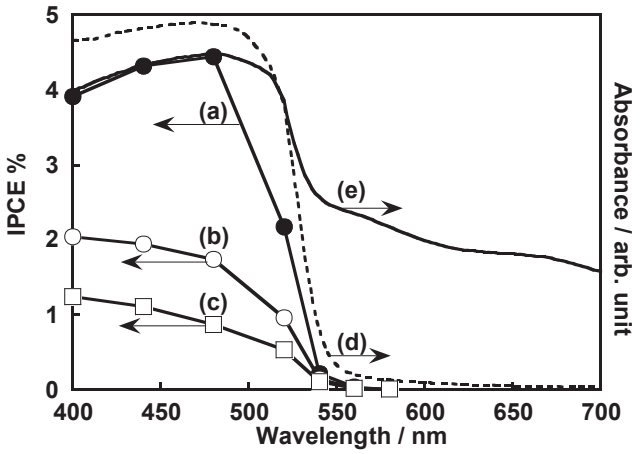

Figure 4-7. IPCEs for cathodic photocurrent of Thin-ZnS(A)/$Cu_{0.8}Ag_{0.2}GaS_2$ electrode at (a) −1, (b) −0.6 and (c) −0.3 V vs. Ag/AgCl and diffuse reflectance spectra of (d) $Cu_{0.8}Ag_{0.2}GaS_2$ powder and (e) Thin-ZnS(A)/$Cu_{0.8}Ag_{0.2}GaS_2$ electrode. Electrolyte: 0.1 mol L^{-1} of $K_2SO_{4\ aq.}$ with phosphate buffer (0.025 mol L^{-1} of $KH_2PO_{4\ aq.}$ and $Na_2HPO_{4\ aq.}$) under N_2 atmosphere, light source: a 300 W Xe-arc lamp with a cutoff filter ($\lambda > 420$ nm), counter electrode: Pt plate.

same as that of pristine $Cu_{0.8}Ag_{0.2}GaS_2$ powder, while the back ground of a diffuse reflectance spectrum arose by annealing TF-ZnS(NA)/$Cu_{0.8}Ag_{0.2}GaS_2$ photoelectrode. Onsets of the IPCE at different potentials agreed with a diffuse reflectance spectrum indicating that the cathodic photocurrent was observed by the band gap excitation. Thus, the modification of ZnS thin film on the surface of $Cu_{0.8}Ag_{0.2}GaS_2$ photoelectrode improved the charge separation of the carriers photogenerated by band gap excitation of $Cu_{0.8}Ag_{0.2}GaS_2$.

4-3-2. Improvement of ZnS-modified $Cu_{0.8}Ag_{0.2}GaS_2$ photocathode for CO_2 reduction by loading cocatalysts

Table 4-1 shows CO_2 reduction over pristine $Cu_{0.8}Ag_{0.2}GaS_2$ and TF-ZnS(A)/$Cu_{0.8}Ag_{0.2}GaS_2$ photoelectrodes. Pristine $Cu_{0.8}Ag_{0.2}GaS_2$ photoelectrode gave cathodic photocurrent and produced CO at −0.6 V vs. Ag/AgCl under visible light irradiation. The current and amount of CO evolved were improved by modifying ZnS thin film with annealing. The Faradaic efficiency for CO evolution calculated by equation (1) reached at 16%. The efficiency was about five times as high as that of the pristine $Cu_{0.8}Ag_{0.2}GaS_2$ photoelectrode.

Faradaic efficiency for CO evolution (FE_{CO})
= (the number of electrons consumed for CO formation / μmol) / (the number of electrons calculated from the quantity of electricity / μmol)×100 (1)

This result indicates that ZnS thin film on the surface $Cu_{0.8}Ag_{0.2}GaS_2$ photoelectrode functions as not only the layer with n-type character to form p-n junction for improvement of the charge separation but also an active site for CO_2 reduction to form CO. ZnS nanoparticle shows activity for CO_2 reduction even without any cocatalyst. Therefore, the reason why FE_{CO} of $Cu_{0.8}Ag_{0.2}GaS_2$ photoelectrode was enhanced by modifying ZnS thin film is that the surface of the ZnS has active site to reduce CO_2 to CO. Moreover, CO did not evolve under dark in CO_2 atmosphere and visible

Table 4-1 Effect of ZnS modification on photocathodic property of $Cu_{0.8}Ag_{0.2}GaS_2$ electrode under CO_2 and N_2 atmosphere.

Modification of ZnS	Gas (1 atm)	Electrolyte	Visible light irradiation	Cathodic current density / μA cm^{-2}	Amounts of products (3 h) / μmol		FE_{CO} %
					H_2	CO	
No	CO_2	$KHCO_3$	Yes	53~65	1.9	0.1	3
Yes	CO_2	$KHCO_3$	Yes	190~602	12.1	2.1	16
Yes	CO_2	$KHCO_3$	No	−	0	Trace	−
Yes	N_2	[a]K_2SO_4	Yes	268~604	24.5	Trace	−

Electrolyte: 0.1 mol L^{-1} of $K_2SO_{4\ aq.}$ with phosphate buffer (0.025 mol L^{-1} of $KH_2PO_{4\ aq.}$ and $Na_2HPO_{4\ aq.}$), light source: a 300 W Xe-arc lamp with a cutoff filter ($\lambda > 420$ nm), potential: −0.6 vs. Ag/AgCl, counter electrode: Pt plate.
FE_{CO}: Faradaic efficiency for CO evolution.

light irradiation in N_2 atmosphere, indicating that CO_2 reduction to form CO proceeded photoelectrochemically.

In CO_2 reduction over wide band gap photocatalysts, Ag and Cu cocatalysts behave as a good active site for CO_2 reduction. Therefore, it is interesting to load metal cocatalysyts onto the TF-ZnS(A)/$Cu_{0.8}Ag_{0.2}GaS_2$ photoelectrode. Effects of loading cocatalysts on the activity for CO_2 reduction using TF-ZnS(A)/$Cu_{0.8}Ag_{0.2}GaS_2$ photoelectrode were evaluated as shown in Table 4-2. The cathodic photocurrent was increased by loading various cocatalysts except Rh cocatalyst. Especially, when Ag cocatalyst was loaded, the cathodic photocurrent and amount of CO evolved increased compared with that of the TF-ZnS(A)/$Cu_{0.8}Ag_{0.2}GaS_2$ photoelectrodes loaded with other cocatalysts. The stability of cathodic photocurrent for CO_2 reduction using pristine $Cu_{0.8}Ag_{0.2}GaS_2$, TF-ZnS(A)/$Cu_{0.8}Ag_{0.2}GaS_2$ and TF-ZnS(A)/$Cu_{0.8}Ag_{0.2}GaS_2$ loaded with Ag cocatalyst were compared as shown in Figure 4-8. The cathodic photocurrent of $Cu_{0.8}Ag_{0.2}GaS_2$ photoelectrode was enhanced by modifying ZnS thin film, although the stability of the cathodic photocurrent was not satisfying. In contrast, the cathodic photocurrent and the partial current density for CO evolution were drastically not only improved but also stabilized by loading Ag. The partial current density for CO evolution calculated from Faradaic efficiency for CO evolution to the average photocurrent of pristine-$Cu_{0.8}Ag_{0.2}GaS_2$, TF-ZnS(A)/$Cu_{0.8}Ag_{0.2}GaS_2$ and Ag-loaded TF-ZnS(A)/$Cu_{0.8}Ag_{0.2}GaS_2$ (Ag/ZnS/$Cu_{0.8}Ag_{0.2}GaS_2$) photoelectrodes were about 2, 50 and 300 μA cm^{-2}, respectively. The mixed gases of H_2 and CO produced by the Ag/ZnS/$Cu_{0.8}Ag_{0.2}GaS_2$ photoelectrode was visually observed as shown in Figure 4-9.

In the CO_2 reduction, it is important to confirm that the products originate from not contamination but CO_2 gas by using $^{13}CO_2$. Only ^{13}CO was obtained by reduction of $^{13}CO_2$ over the Ag/ZnS/$Cu_{0.8}Ag_{0.2}GaS_2$ photoelectrode. This result indicated that the CO evolved from a CO_2 molecule by photoelectrocatalytic reaction.

Table 4-2 Effect of loading cocatalysts on CO_2 reduction using Thin-ZnS(A)/$Cu_{0.8}Ag_{0.2}GaS_2$ photocathode.

Cocatalyst	Cathodic current density / mA cm^{-2}	Amounts of products (3 h) / μmol		FE_{CO}
		H_2	CO	%
None	0.2~0.6	12	2.1	16
Cu	1.0~1.8	53	7.8	12
Ru	0.3~0.4	12	0.5	4
Rh	0.1~0.2	7.6	0.3	20
Ag	1.1~1.9	61	14	20
Pt	0.7~0.8	33	1	3
Au	0.3~0.6	20	1.5	7

Electrolyte: 0.1 mol L^{-1} of $KHCO_{3\ aq.}$ with dissolved CO_2 at 1 atm, light source: a 300 W Xe-arc lamp with a cutoff filter ($\lambda > 420$ nm), sweep range: −0.6 vs. Ag/AgCl, a counter electrode: Pt plate.

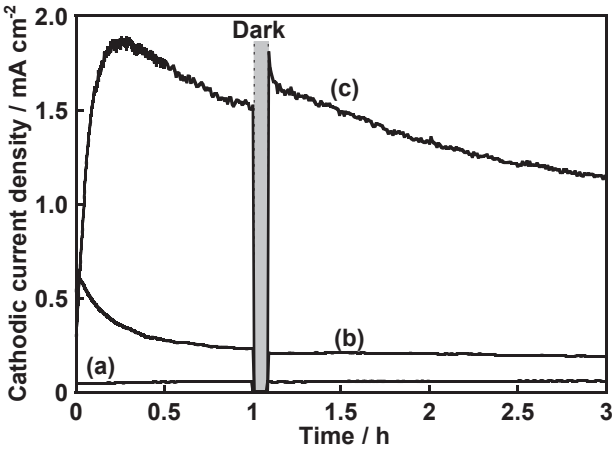

Figure 4-8. Stability of the photocurrent for CO_2 reduction of (a) pristine-$Cu_{0.8}Ag_{0.2}GaS_2$, (b) TF-ZnS(A)/$Cu_{0.8}Ag_{0.2}GaS_2$ and (c) Ag-loaded TF-ZnS(A)/$Cu_{0.8}Ag_{0.2}GaS_2$ photoelectrodes. Electrolyte: 0.1 mol L^{-1} of $KHCO_{3\ aq.}$ with dissolved CO_2 at 1 atm, light source: a 300 W Xe-arc lamp with a cutoff filter ($\lambda > 420$ nm), sweep range: −0.6 vs. Ag/AgCl, counter electrode: Pt plate.

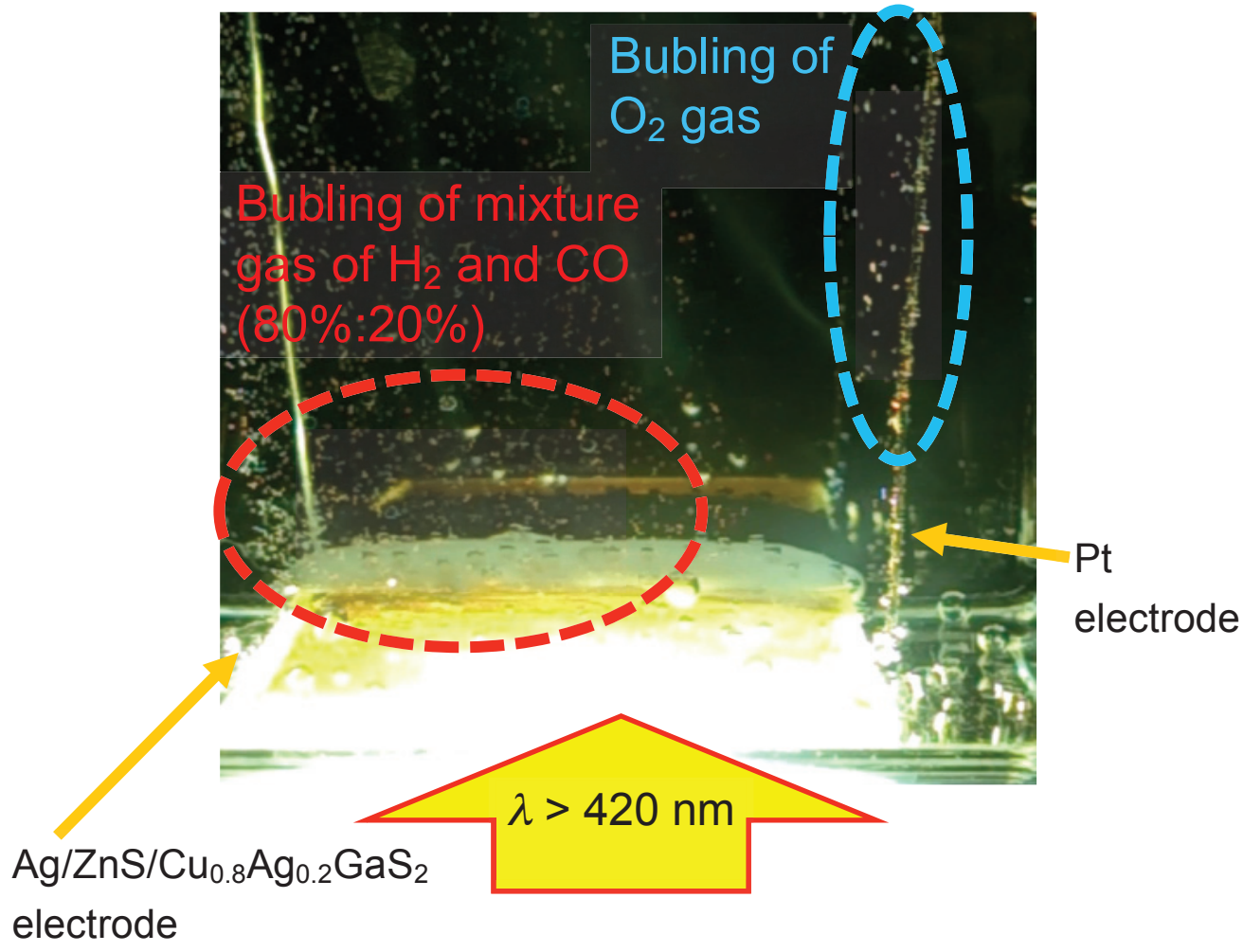

Figure 4-9. CO_2 reduction using Ag-loaded TF-ZnS(A)/$Cu_{0.8}Ag_{0.2}GaS_2$ photocathode (20 cm^2). Electrolyte: 0.1 mol L^{-1} of $KHCO_{3\ aq.}$ with dissolved CO_2 at 1 atm, light source: a 300 W Xe-arc lamp with a cutoff filter (λ > 420 nm), sweep range: –0.6 vs. Ag/AgCl, counter electrode: Pt wire

4-3-3. Construction of photoelectrochemical cell consisting of Ag/ZnS/$Cu_{0.8}Ag_{0.2}GaS_2$ photocathode and CoO/$BiVO_4$ photoanode for CO_2 reduction utilizing solar energy without an external bias

The photoelectrochemical cell consisting of Rh-doped $SrTiO_3$ and CoO/$BiVO_4$ photoelectrodes split water into H_2 and O_2 in stoichiometric amounts under pseudo-sunlight irradiation without any external bias. Therefore, CO_2 reduction without any external bias was evaluated by constructing the photoelectrochemical cell using Ag/Thin-ZnS(A)/$Cu_{0.8}Ag_{0.2}GaS_2$ and CoO/$BiVO_4$ photoelectrodes. The cell gave photocurrent and produced H_2 and CO as reduction products of H_2O and CO_2, and O_2 as an oxidation product of H_2O without any external bias under visible light irradiation as shown in Figure 4-10. Moreover, the cell is also active under pseudo-sunlight. This indicates that H_2 and CO evolve by consuming water as an electron donor. The solar energy conversion efficiency for CO evolution was 0.0005%. Thus, the solar energy conversion accompanied with CO_2 reduction to form CO using water as an electron donor was demonstrated by developing Ag/ZnS/$Cu_{0.8}Ag_{0.2}GaS_2$ of a new photoelectrode.

4-4. Conclusions

$Cu_{0.8}Ag_{0.2}GaS_2$ photoelectrode reduced CO_2 to CO under visible light irradiation. The cathodic photocurrent and the Faradaic efficiency for CO evolution increased by modification of ZnS thin film prepared by a chemical bath deposition. The cathodic photocurrent increased by loading metal cocatalysts. Especially, the stability of the cathodic photocurrent and the partial current density for CO evolution were drastically improved by loading Ag cocatalyst. The partial current density for CO evolution had achieved at about 300 μA cm^{-2}. The electrochemical cell consisting of Ag/ZnS/$Cu_{0.8}Ag_{0.2}GaS_2$ as a cathode and CoO/$BiVO_4$ as an anode gave photocurrent and produced CO as a reduction product of CO_2 under pseudo sun light irradiation without any external bias. The solar energy conversion efficiency accompanied with reducing CO_2 to form CO was 0.0005%.

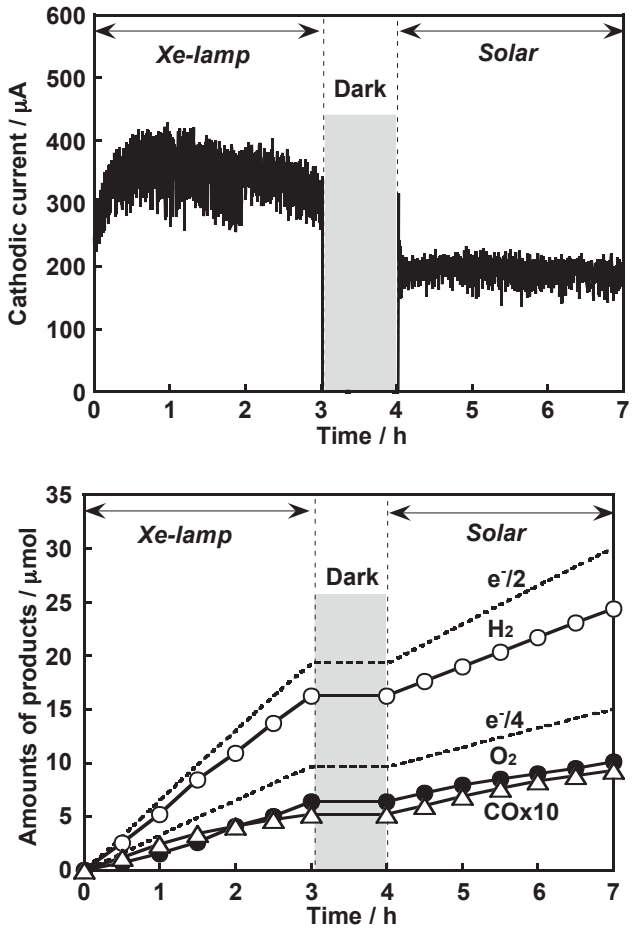

Figure 4-10. CO_2 reduction utilizing water as an electron donor using the photoelectrochemical cell constructing of Ag-loaded TF-ZnS(A)/$Cu_{0.8}Ag_{0.2}GaS_2$ photocathode and CoO/$BiVO_4$ photoanode under visible light irradiation and pseudo-sun light with any external bias. Electrolyte: 0.1 mol L^{-1} of $KHCO_{3\ aq.}$ with dissolved CO_2 at 1 atm, light source: a 300 W Xe-arc lamp with a cutoff filter (λ > 420 nm) and solar simulator, electrode area: Ag-loaded TF-ZnS(A)/$Cu_{0.8}Ag_{0.2}GaS_2$ photocathode; 20 cm^2 and CoO/$BiVO_4$ photoanode; 5 cm^2.

References

(1) Iizuka, K.; Wato, T.; Miseki, Y.; Saito, K.; Kudo, A. *J. Am. Chem. Soc.* **2011**, *133*, 20863.

(2) Teramura, K.; Wang, Z.; Hosokawa, S.; Sakata, Y.; Tanaka, T. *Chem. Eur. J.* **2014**, *20*, 9906.

(3) Kanemoto, M.; Ishihara, K.; Wada, Y.; Sakata, T.; Mori, H.; Yanagida, S. *Chem. Lett.* **1992**, 835.

(4) Ma, G.; Minegishi, T.; Yokoyama, D.; Kubota, J.; Domen, K. *Chem. Phys. Lett.* **2011**, *501*, 619.

(5) Tsutsui, Y. *the master's thesis at Tokyo University of Science* **2009**.

(6) Kaga, H. *the doctoral thesis at Tokyo University of Science* **2015**.

(7) W. J. Chen, *et al*. *Appl. Surf. Sci.*, **2013**, *264*, 213.

Chapter 5

Conclusions

In this thesis, a new photocatalyst was developed by focusing on metal oxide with tungsten bronze structure. The reaction mechanism for CO_2 reduction was discussed. Moreover, new visible-light-driven photocathode for CO_2 reduction was developed to consist of the photoelectrochemical cell for CO_2 reduction using water as an electron source of an artificial photosynthesis.

In the chapter 2, $KCaSrTa_5O_{15}$ of a new photocatalyst for water splitting and CO_2 reduction was developed and the mechanism for CO_2 reduction was discussed based on various characterizations. $KCaSrTa_5O_{15}$ with tungsten bronze structure prepared by a solid-state reaction showed activity for water splitting without cocatalysts. CO_2 reduction using the photocatalyst was examined. As the result of surveying various cocatalysts, Ag cocatalyst functioned as the active site for CO_2 reduction to form CO. In this reaction, H_2, CO, and O_2 evolved in a stoichiometric ratio. The turnover number calculated from the number of electrons consumed to form CO to the number of Ag atom in cocatalyst was larger than 1. Additionally, an isotope experiment using $^{13}CO_2$ revealed that the CO produced from a CO_2 molecule by photocatalytic reduction over $Ag/KCaSrTa_5O_{15}$. These results indicate that the CO_2 reduction over $Ag/KCaSrTa_5O_{15}$ proceeded photocatalytically using water as an electron donor.

The $KCaSrTa_5O_{15}$ photocatalyst was prepared as nanorod particles by a polymerized complex method being different from a solid-state reaction. Observation of a scanning electron microscope and a transmission electron microscope indicates that the nanorod particle was a single crystal particle grown along c-axis with tungsten bronze structure.

The Tb-doped nanorod single crystal particle gave green emission originated from the $^5D_4 \rightarrow {}^7F_6$ and $^5D_4 \rightarrow {}^7F_5$ transitions of Tb^{3+} by host excitation at room temperature. In contrast, the Tb-doped polycrystalline particles prepared by the solid-state reaction did not give the emission. This indicates that the single crystalline nanorod particle has a small amount of the recombination center such as the grain boundary and the defect compared with that of polycrystalline particles. The single crystalline nanorod photocatalyst showed relative high activity for water splitting by loading NiO-cocatalyst. The apparent quantum yield was 6.6% at 254 nm. The efficiency was about

three times as high as that of polycrystalline particles. It is clear from the probing the photoluminescence of Tb that the photogenerated carrier migrated smoothly in the single crystalline nanorod particle prepared by a polymerized complex method. The Ag-cocatalyst-loaded single crystalline nanorod photocatalyst showed activity for CO_2 reduction to form CO in a stoichiometric amount using water as an electron donor. The reaction was drastically improved by adding $NaHCO_3$ into the reactant solution. The selectivity for CO evolution calculated from obtained reduction products was about 90%. The reason why the selectivity was improved by adding $NaHCO_3$ may be that CO_2 molecules are smoothly supplied to the active site by releasing the CO_2 molecule from HCO_3^- in an aqueous medium. Additionally, the photocatalyst after CO_2 reduction gave the surface plasmonic absorption, indicating that Ag-cocatalysts were present at the state of metallic nanoparticles. In contrast, when NiO-cocatalysts were loaded, CO did not evolve even if $NaHCO_3$ was added into the reactant solution. Thus, it was concluded that the selectivity for CO evolution is improved by smooth supply of the CO_2 molecule to Ag-cocatalyst of an active site for CO_2 reduction to form CO. In conclusion, it was demonstrated that the preparation of the particle having the bulk property which photogenerated carrier migrates smoothly and the supply of the substrate on the suitable active site are important designing guide to achieve highly efficient photocatalytic reaction.

In the chapter 3, the effects of the strain of the crystal structure on the crystal growth process and photocatalytic activities were discussed by using $K_3Ta_3Si_2O_{13}$ and $Ba_3Ta_6Si_4O_{26}$ of the metal oxide materials with the same crystal structure. The band gaps of $K_3Ta_3Si_2O_{13}$ and $Ba_3Ta_6Si_4O_{26}$ with tungsten bronze-like structure prepared by a flux method were 4.2 and 4.3 eV, respectively. The strain of the crystal framework along the c-axis of $Ba_3Ta_6Si_4O_{26}$ photocatalyst is larger than that of $K_3Ta_3Si_2O_{13}$ photocatalyst, indicating that the band gap increases by the localization of the excitation energy. Thus, it was clarified that the strain of the crystal framework affected the band gap not only perovskite structure but also tungsten bronze-like structure. Moreover, the strain affects the crystal growth and photocatalytic activity for water splitting as mentioned bellow.

This effect on photocatalysts with tungsten bronze-like structure was similar to that on

photocatalysts such as $ATaO_3$ (A = Na and K) with perovskite structure. $K_3Ta_3Si_2O_{13}$ photocatalysts with small strain of the crystal structure along c-axis were obtained nanorod-shaped particles, while $Ba_3Ta_6Si_4O_{26}$ photocatalysts with the large strain were obtained block-shaped particles. The apparent quantum yield for water splitting over NiO-cocatalyst-loaded $K_3Ta_3Si_2O_{13}$ and $Ba_3Ta_6Si_4O_{26}$ photocatalysts were 2.4 and 0.2% at 254 nm, respectively. These results indicate that the large strain of the crystal framework along c-axis may suppress the crystal growing along c-axis and decrease the mobility of the photogenerated carrier in not only perovskite structure but also tungsten bronze-like structure. Thus, the relationship among the strain of the crystal framework with tungsten bronze-like structure, the crystal growth process, and the photocatalytic activity had been clarified.

In the chapter 4, the photocathode using a $Cu_{0.8}Ag_{0.2}GaS_2$ photocatalyst with a p-type semiconductor character was developed for CO_2 reduction utilizing water as an electron donor. Pristine $Cu_{0.8}Ag_{0.2}GaS_2$ photocathode showed activity for the CO_2 reduction to form CO. The cathodic photocurrent and Faradaic efficiency for CO evolution were improved by modification of ZnS thin film. The results indicated that the modification of ZnS thin film enhanced the charge separation by forming a p-n junction between the ZnS layer and $Cu_{0.8}Ag_{0.2}GaS_2$ and functioned as the active site for CO evolution. Moreover, the cathodic photocurrent and the partial current density for CO evolution were drastically improved by loading Ag-cocatalyst on the ZnS-modified $Cu_{0.8}Ag_{0.2}GaS_2$ photoelectrode. This result suggests that Ag-cocatalyst is suitable active site for CO_2 reduction in not only photocatalyst-powder system but also photocatalyst-electrode system. Moreover, the photoelectrochemical cell consisting of the photocathode and a $CoO/BiVO_4$ photoanode showed activity for CO_2 reduction using water as an electron donor without any external bias under pseudo-sunlight. Thus, the photoelectrochemical cell which can convert the solar energy by CO_2 reduction using water as an electron donor was successfully constructed by using visible-light driven $Ag/ZnS/Cu_{0.8}Ag_{0.2}GaS_2$ of a new photocathode for CO_2 reduction.

Figure 5-1 shows the typical strategy to develop highly efficient photocatalyst for water splitting and CO_2 reduction, and the contribution of this thesis to the strategy. It is conducted The

fundamental research to design highly efficient new photocatalyst materials and systems and store scientific knowledge. Additionally, development of new photocatalyst materials and systems based on the fundamental research give the new knowledge. As the result, highly efficient photocatalysts and photocathodes for water splitting and CO_2 reduction have been developed. In this thesis, especially, Ag/ZnS/$Cu_{0.8}Ag_{0.2}GaS_2$ photocathode developed in chapter 4 have achieved artificial photosynthesis for CO_2 reduction using solar energy without any external bias by consisting photoelectrochemical cell with a CoO/$BiVO_4$ photoanode, although the activity is not high at the present stage. This insights will probably give new information for multi field such as material science, crystal chemistry, and electrochemistry and so. In future, a new photocathode using metal sulfide photocatalysts with narrower band gap and p-type semiconductor character will be developed by comodification of semiconductor thin film with n-type and suitable cocatalysts such as the Ag/ZnS/$Cu_{0.8}Ag_{0.2}GaS_2$ photocathode. The new photocathode is also useful to consist of the highly efficient photoelectrochemical cell for CO_2 reduction.

Finally, the author hopes that the knowledge of this thesis is useful to achieve artificial photosynthesis for solar hydrogen production and CO_2 fixation.

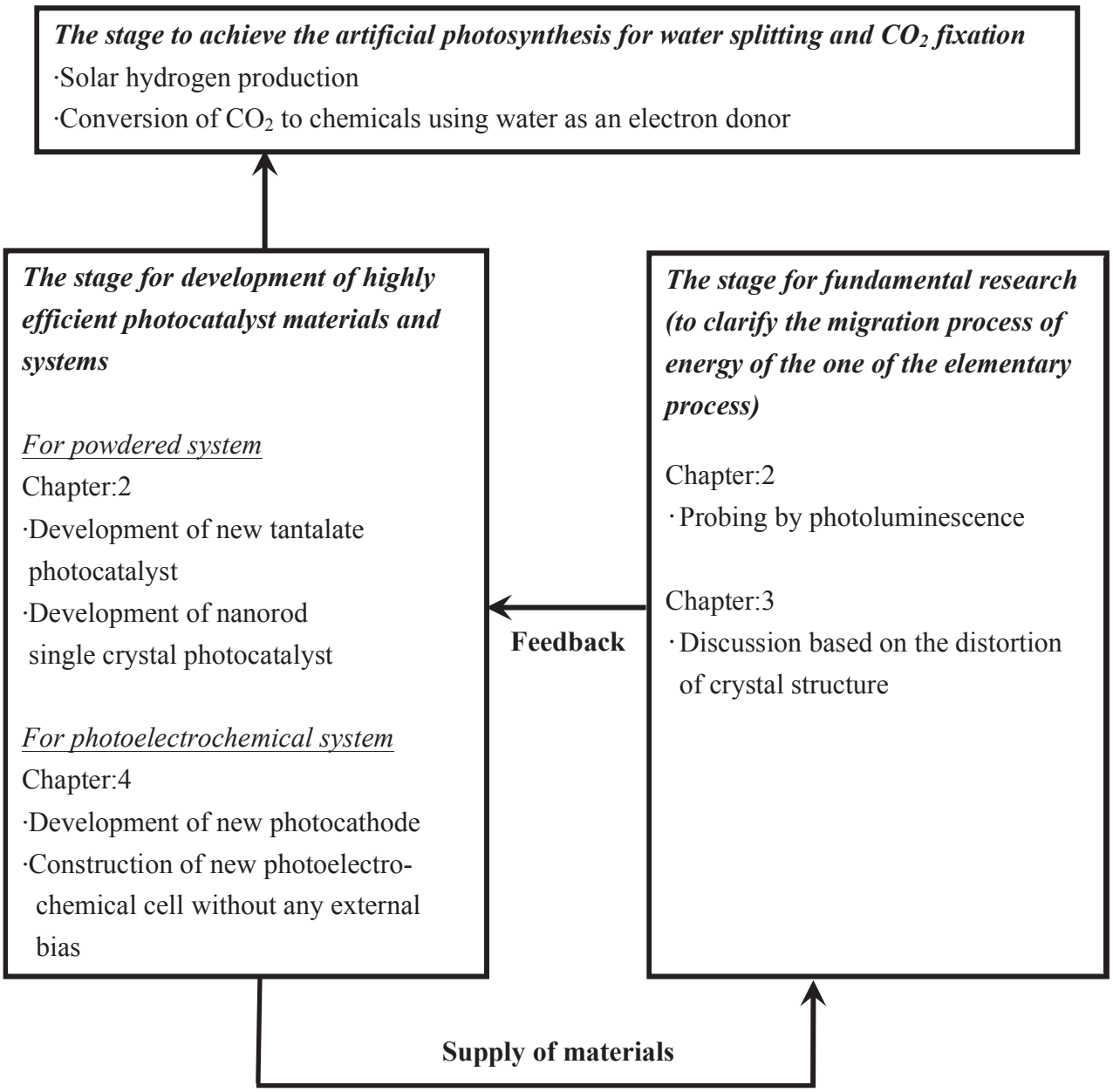

Figure 5-1. The typical strategy to develop highly efficient photocatalyst for water splitting and CO_2 reduction and the contribution of this thesis to the strategy.

List of publications

1. For the chapter 2; The $KCaSrTa_5O_{15}$ Photocatalyst with Tungsten Bronze Structure for Water Splitting and CO_2 Reduction

T. Takayama, K. Tanabe, K. Saito, A. Iwase, A. Kudo, *Phys. Chem. Chem. Phys.*, **2014**, *16*, 24417.

2. For the chapter 2; Photocatalytic Water Splitting and CO_2 Reduction over $KCaSrTa_5O_{15}$ Nanorod prepared by a Polymerized Complex Method

T. Takayama, A. Iwase, A. Kudo, *Bull. Chem. Soc. Jpn.*, *in communication*.

3. For the chapter 3; Photocatalytic Water Splitting over Rod-shaped $K_3Ta_3Si_2O_{13}$ and Block-shaped $Ba_3Ta_6Si_4O_{26}$ prepared by Flux Method

T. Takayama, A. Iwase, A. Kudo, *Chem. Lett.*, *in press*.

Others

1. Photocatalytic Reduction of Carbon Dioxide over Ag Cocatalyst-Loaded $ALa_4Ti_4O_{15}$ (A=Ca, Sr, and Ba) Using Water as a Reducing Reagent

K. Iizuka, **T. Wato**, Y. Miseki, K. Saito, A. Kudo, *J. Am. Chem. Soc.*, **2011**, *133*, 20863.

2. Enhanced Photocatalytic Water Splitting by $BaLa_4Ti_4O_{15}$ Loaded with ~1nm Gold Nanoclusters using Glutathione-Protected Au25 Clusters

Y. Negishi, M. Mizuno, M. Hirayama, M. Omatoi, **T. Takayama**, A. Iwase, A. Kudo, *Nanoscale* (communications), **2013**, *5*, 7188. Selected as "Outside Back Cover"

3. Effects of cocatalyst on carrier dynamics of a titanate photocatalyst with layered perovskite

structure

M. Yabuta, **T. Takayama**, K. Shirai, K. Watanabe, A. Kudo, T. Sugimoto,Y. Matsumoto, *J. Phys. Chem. C*, **2014**, *118*, 10972.

4. 微小金クラスター助触媒担持による水分解光触媒の高活性化

御纏真実子，平山道世，**髙山大鑑**，岩瀬顕秀，工藤昭彦，根岸雄一，2013，ナノ学会会報，第 12 巻，29-33.